SCUOLA INTERNAZIONALE SUPERIORE DI STUDI AVANZATI

PHD COURSE IN THEORY AND NUMERICAL SIMULATION
OF CONDENSED MATTER

SISSA
40!

---

ab initio Simulation of Heat Transport
in Silica Glass

A thesis submitted for the degree of *Doctor Philosophiæ*

Candidate
Loris ERCOLE

Supervisor
Prof. Stefano BARONI

OCTOBER 2018

To my parents.

Contents

1

Introduction

Heat flow is ubiquitous in nature, it governs a multitude of complex processes, from the evolution of stars and planets to the dynamical stability of biological systems, all the way down to the maintenance of optimal operating conditions in many (nano)technological applications. Heat flow determines the internal temperature distribution of out-of-equilibrium systems and the rate of cooling or heating of bodies. Therefore the study of thermal transport is fundamental to modeling a multitude of complex systems, and to engineer nanotechnologies, where thermal insulation or dissipation properties have to be properly designed. Yet, despite being one the oldest problems of statistical mechanics, a complete theoretical understanding of heat transport is still lacking.

Transfer of thermal energy occurs via three different mechanisms, that may prevail or coexist in different regimes [1]: *convection*, in which heat is transported by a flow of mass; *radiation*, in which heat is removed from the surface of the hot source by photons; and *conduction*, in which heat transfer is determined by the microscopic dynamics of atoms, or in the case of metals, of conduction electrons. In condensed phases and at the molecular scale, conduction is by far the most relevant heat transfer mechanism, and we shall focus on it. The first macroscopic theory of heat transport was formulated by Fourier [2], in 1822, who established a proportionality law between the heat current $\mathbf{J}$ and the temperature gradient in the system ∇T:

$$\mathbf{J} = -\kappa\,\nabla T\,. \tag{1.1}$$

The ratio between the heat flux and the temperature gradient defines the *thermal conductivity*, κ, which is an intrinsic property of the material.

Glass, a quintessential nanotech man-made material

Although being known and used for more than three thousand years, the last century experienced extraordinary advances in the definition, fabrication, characterisation, and application of glass [3]. Methods and theory analogous to those employed in the study of crystalline solids have been used to study the electronic, atomic, and micro-structural properties of glass, trying to describe the basic nature of the glassy state, that still represents one of the most difficult open problems in science [4]. An increased understanding and control of the structure of glass, with both fundamental and fabrication advances, has led to remarkable applications in a variety of fields such as civil engineering, transportation, electronics, photonics, communication, and

medicine, many of which are today accepted as the norm. Glass is more and more demanded as a high-tech material for consumer electronic devices, and it is going to play a critical role in solving several of the global energy and healthcare challenges of today.

An atomic-level description of the glassy state is extremely complex due to the lack of long-range order found in crystalline materials, and to the intrinsic non-equilibrium nature of this material. However, thanks to the recent theoretical and experimental advances, glass science is maturing from an empirical discipline to one built upon rigorous scientific principles. The glass transition and the processes involved in glass formation are still open questions. The chemistry of glasses can be extremely complex: glass compositions are infinitely tunable in chemistry, allowing one to design glasses with tailored mechanical, optical, electrical, magnetic, and thermal properties for specific purposes. However this task is far from easy. For example, it was recently discovered that two glasses of identical chemistry may exhibit considerably different short-range structural ordering, thus leading to large differences in the observed properties, a phenomenon called polyamorphism [5, 6].

In particular, the thermal conductivity is a fundamental property for many industrial and technological applications of glass, ranging from electronics to the insulation efficiency of windows for green architectures, to nuclear waste storage. Despite its importance, *"thermal conductivity of glass represents largely unexplored territories, ripe for new research efforts"* (J. Mauro, senior research manager – Glass Research, Corning Inc.) [4]. The understanding of thermal conductivity and its structural origin in glasses has been greatly overlooked in the literature and presents several non trivial challenges for atomistic simulations. The problem of generating faithful amorphous structures and the correct description of the vibrational properties are the key points that one needs to solve to estimate the thermal conductivity of glasses. Moreover, non-periodic systems still lack a theory able to describe the contributions to the thermal conductivity in a way similar to methods widely used for crystalline solids.

Vitreous silica

Vitreous silica (a-SiO_2, aka fused silica or fused quartz) and silicate glasses in general have been the subject of significant research efforts in the last decades, due to their many technological applications that range from thermal insulation to laser engineering, semiconductor fabrication, and optical communication. In particular, thanks to its excellent UV transparency, mechanical stability, and chemical durability, silica can be used in many optical applications, such as the diffractive elements and the protective windows of the optics assemblies of inertial confinement fusion facilities. In these facilities, extremely intense nanosecond laser pulses are used and can seriously challenge the durability the optical glasses. It is indeed well established that the small defects or impurities of the glass may cause local lattice heating and melting, resulting in damage craters that will rapidly degrade its optical performance [7–15]. Moreover, these local damages can be mitigated by using pulsed laser treatments that increase the damage sites to temperatures of $2000 - 5000\,\mathrm{K}$

in 10^{-9} down to 10^{-12} s and partially restore the desired optical properties [16]. The interpretation of these types of damage processes require the study of thermal properties and the prediction of the thermal conductivity of silica glass, especially in these extreme conditions that experiments cannot probe.

Furthermore, amorphous silica serves as the basis of multicomponent silica glasses, that are adopted for a wide range of special applications. To cite an example, borosilicate glasses (BSG) are broadly used to vitrify and immobilize high-level nuclear waste, forming a stable solid matrix that is then stored for very long time [17]. These glasses proved to be one of the most reliable materials to accomplish this task, indeed their intrinsic disorder reduces the effects of radiation damage and their chemical stability and resistance to water corrosion ensures a long and safe storage. A high thermal conductivity favours the efficiency of the fabrication and the stability of the final product, as it entails a faster dissipation of heat generated by radioactive decays. Predicting the thermal conductivity of silica also represents the first step towards the prediction of the thermal conductivity of more complicated glasses such as BSG, whose components are characterised by a complex chemistry that is more difficult to model.

Silica glass has been the subject of many classical MD studies in the last twenty years, that showed that classical force fields can reproduce reasonably well all the structural properties of a-SiO_2, but do not describe very well its vibrational spectrum, that instead requires first-principles simulations. Its thermal conductivity, that depends on both these properties, still lacks satisfactory and reliable calculations and thus calls for a rigorous study to finally settle the issue. Besides, silica also lacks a proper study determining dependence of κ on some simulation factors, such as the cooling protocol used to prepare the glass sample and that influences remarkably its structural properties, and the size of system.

Computing thermal conductivity

Notwithstanding its fundamental importance, *"thermal conductivity has proven to be one of the most difficult transport coefficients to calculate"* [18] and its simulation is still today a conceptual, no less than practical, challenge to our materials modeling capabilities. In order to compute κ, one needs a microscopic theory that describes the conduction of heat carriers, *i.e.* electrons and lattice vibrations (phonons). Hereafter we will focus only on lattice vibrations, the only carriers contributing to heat transport in *insulators* (the electrons following adiabatically in their ground state), to which we restrict our attention. The first microscopic theory of lattice thermal transport was formulated by Peierls, in 1929, and is based on the assumption that phonons obey the Boltzmann transport equation (BTE) [19]. About thirty years later, Green and Kubo (GK) independently expressed the thermal conductivity, as well as other transport coefficients, by liner response theory in terms of correlation functions of the heat currents [20–24]:

$$\kappa \propto \int_0^\infty \langle J(t) J(0) \rangle \, dt, \tag{1.2}$$

where the brackets indicate ensamble averages, thus allowing its computation from simple equilibrium molecular dynamics (MD) simulations.

In the meantime, a few decades ago, our abilities to understand and predict the properties of materials were boosted by the advent of density functional theory (DFT) [25–27], which allows computing interactions entirely from quantum mechanics, thus freeing us from the need to leverage prior experimental knowledge, in order to perform MD simulations.

Recent developments enabled the implementation of the BTE from first principles, thus making it the state of the art technique to compute κ of bulk crystalline materials (*e.g.* Si, Ge, diamond [28, 29]) and nanostructures (*e.g.* graphene and 2D materials [30]). *Ab initio* BTE also provides insights into the mechanisms of heat transport, by breaking down the contributions to κ into single carrier properties. Nonetheless, the applicability of the BTE approach is limited to periodic materials at low temperatures, where the harmonic approximation of normal modes applies or anharmonic effects are very limited, and it cannot be straightforwardly applied to disordered systems, such as glasses and liquids, were phonons are not even defined, and for which MD is a natural choice.

On the other hand, MD is set to overcome these limitations: it allows one to study non-periodic and highly anharmonic systems in a straightforward way and to compute their thermal conductivity accounting for full anharmonicity. The only inputs required are the atomic structure and an appropriate interatomic potential, which can be constructed empirically, *e.g.* by fitting previous experimental or *ab initio* results using force fields or modern neural networks (classical MD), or directly by first-principles DFT calculations (*ab initio* MD, AIMD). Once one has these ingredients, κ can be computed from equilibrium MD (EMD) or non-equilibrium MD (NEMD) simulations. The latter directly exploits the Fourier law, Eq. (1.1), and applies straightforwardly to finite systems and interfaces, but suffers from severe practical difficulties, such as finite-size and non-linear effects, that have to be carefully accounted for. Instead, we focus on EMD simulations, from which the thermal conductivity can be computed directly via the GK equation, Eq. (1.2), that only requires an expression for the *heat current*. For classical empirical potentials, such expression can be readily obtained as a sum of atomic contributions, containing the atomic coordinates, velocities, and forces. On the other hand, a corresponding definition in the framework of DFT was not considered possible until very recently, when it was formulated successfully for the first time [31]. Indeed, despite its rigour and simplicity, the GK theory has long been deemed incompatible with DFT, because the total energy cannot be decomposed into individual localized atomic contributions, thus making the heat current ill-defined.

This conceptual prejudice hindered the development of the GK theory in AIMD simulations for many years. It was only a few years ago that the spurious nature of this belief was recognized through the discovery of a *gauge invariance principle* for transport coefficients [A, 31]. This principle ensures the value of thermal conductivity ultimately estimated through the GK equation does not depend on the microscopic details that define the energy density, from which the heat current is derived, hence κ is well-defined, as any measurable quantity should be. However,

the problem of univocally defining the atomic energies exists also in classical MD simulations and was recognized in the past, although applications of the GK equation resorted on what was considered the most straightforward definition, without formally justifying this choice.

On the other hand, despite these important discoveries, experience from classical MD simulations indicates that the practical implementation of the GK theory usually requires very long trajectories to estimate κ, thus making expensive quantum simulations unfeasible. Several expedients have been used in the last twenty years to determine the convergence of the integral in Eq. (1.2) from trajectories of finite-length, yet it is very surprising that none of these is able to estimate the statistical error of κ in an efficient and reliable way. Most of these methods are designed and tested on specific classes of systems, such as crystalline solids (for which, besides, the BTE is the preferable method), but do not work for liquids, disordered or strongly anharmonic systems, or they require extremely long MD simulations. We addressed this problem using an innovative data-analysis method based on the *cepstral analysis* of stationary time series [B], that provides a rigorous estimation of κ with good statistical accuracy from optimally short MD trajectories, for different classes of materials.

These two achievements finally demonstrate the feasibility of *ab initio* GK simulations of thermal transport and pave the way to their application to previously intractable materials, such as fluids, crystals under extreme conditions, and glasses.

Purpose of this Thesis

In this thesis we aim to calculate for the first time the thermal conductivity of silica glass at different temperatures, by applying the *ab initio* Green-Kubo theory of thermal transport. We first show how it is possible to overcome the conceptual and methodological problems mentioned above, that involve the bottom-up definition of a heat current and the estimation of the thermal conductivity from optimally short MD trajectories. For this scope, we present the gauge invariance principle for thermal transport coefficients and an innovative data-analysis protocol. We then introduce the problem of simulating an amorphous system with MD, and by means of classical MD simulations we study the effects of sample preparation on the value of thermal conductivity of a-SiO_2. We use these results as a starting point to run a few first-principles simulations aimed to compute the thermal conductivity of silica at different temperatures using DFT.

This thesis is organized as follows. Chapter 2 introduces the Green-Kubo theory of heat transport. Starting from a light review of the theory of hydrodynamic variables and linear response theory, we derive the GK equation for one-component and multi-component systems, and we obtain an expression for the energy current for classical force fields. In Chapter 3 we address the definition of atomic energies and energy densities in interacting systems. We show that there is no unique way to define the heat current, nevertheless the resulting thermal conductivity is well-defined. We prove this statement by numerical simulations and by theory, introducing the principle of gauge invariance of thermal transport coefficients. In Chapter 4, after

briefly reviewing some of the most recent first-principles simulation techniques of thermal transport, we show how one can derive and compute an *ab initio* expression for the energy current in the framework of density functional theory. Chapter 5 is entirely devoted to the practical evaluation of the thermal conductivity from the GK equation. We briefly review all the analysis methods found in the literature, and comment upon their weak points. We thus introduce a new technique to evaluate transport coefficients, based on the so-called *cepstral analysis* of time series, and we benchmark it with classical MD simulations for different classes of materials. In Chapter 6 we study the thermal conductivity of a-SiO$_2$ using the *ab initio* GK theory. We discuss the aspects involved in the atomistic simulation of glass and we simulate silica with classical MD using a popular force field. In particular, we study the dependence of κ on the size of the system and the quenching rate used in the virtual vitrification process. We then select an optimal system size and simulate one sample with AIMD. We compute its thermal conductivity at four different temperatures, and we finally compare the simulation results with experiments. Chapter 7 finally contains our conclusions.

Some parts of Chapter 2, 3, and 5 were adapted from the following papers that I have (co-)authored:

[**A**] L. Ercole, A. Marcolongo, P. Umari, and S. Baroni, "Gauge invariance of thermal transport coefficients", J. Low Temp. Phys. **185**, 79 (2016) `10.1007/s10909-016-1617-6`.

[**B**] L. Ercole, A. Marcolongo, and S. Baroni, "Accurate thermal conductivities from optimally short molecular dynamics simulations", Sci. Rep. **7**, 15835 (2017) `10.1038/s41598-017-15843-2`.

[**C**] S. Baroni, R. Bertossa, L. Ercole, F. Grasselli, and A. Marcolongo, "Heat transport in insulators from ab initio green-kubo theory", in *Handbook of materials modeling: applications: current and emerging materials*, edited by W. Andreoni, and S. Yip, (Springer International Publishing, Cham, 2018), pp. 1–36, `10.1007/978-3-319-50257-1_12-1`.

[**D**] R. Bertossa, L. Ercole, and S. Baroni, "Transport coefficients in multi-component fluids from equilibrium molecular dynamics", arXiv:1808.03341, 2018.

2

Green-Kubo theory of heat transport

CONTENTS

Our microscopic understanding of heat and mass transport in extended systems is rooted in the Green-Kubo (GK) theory of linear response [21, 22], as applied to the Navier-Stokes equations for the densities of the conserved extensive variables [32, 33], which include energy, momentum, and the particle numbers for each molecular species.

This work was initiated by Onsager in the thirties [34, 35] and carried on by Green and Kubo in the fifties with the theory of linear response [20–23]. The theory is built on the concept of adiabatic decoupling of the slow long-wavelength components of the densities of conserved extensive quantities (which include energy, momentum, and particle number) [32], the so-called *hydrodynamic variables*, from the other atomically fast degrees of freedom. Their work resulted in the celebrated *Green-Kubo equations*, a consequence of the fluctuation-dissipation theorem, that establish a relation between a (non-equilibrium) transport coefficient κ and the spontaneous fluctuations of the relevant currents J at equilibrium. Transport coefficients are in fact proportional to their autocorrelation times:

$$\kappa \propto \int_0^\infty \langle J(t)J(0)\rangle \, dt, \tag{2.1}$$

where the brackets indicate ensemble averages over trajectories, and are accessible to equilibrium MD simulations.

In this chapter we briefly walk through the theory that allows the derivation of the Green-Kubo equations for transport coefficients, starting from the definition of the hydrodynamic variables of a system, in Section 2.1, and the use of linear response theory to connect equilibrium properties to non-equilibrium ones, presented in Section 2.2. In Section 2.3, we specialize to heat transport in solids and one component fluids, and the general case of multi-component fluids, and we derive the expression of the energy flux for systems described by classical force fields.

2.1   Hydrodynamic variables

The macroscopic processes occurring in condensed matter are often described in terms of *extensive variables*. By definition, the value that such a variable assumes for a system is the sum of the values it has for each of its subsystems. This property allows one to express an extensive variable, A, as the integral of a suitably defined density, $a(\mathbf{r})$, as:

$$A[\Omega] = \int_\Omega a(\mathbf{r})d\mathbf{r}, \tag{2.2}$$

where Ω is the system volume. Here and in the following boldfaces indicate 3D vectors and Greek subscripts label Cartesian components: $\mathbf{u} = \{u_\alpha\} = \{u_1, u_2, u_3\}$. When an extensive quantity is locally conserved, a current density, $\boldsymbol{j}(\mathbf{r}, t)$, can be associated to its density in such a way that the two of them satisfy the continuity equation:

$$\frac{\partial a(\mathbf{r}, t)}{\partial t} = -\nabla \cdot \boldsymbol{j}(\mathbf{r}, t), \tag{2.3}$$

where $\nabla \cdot \boldsymbol{j}$ indicates partial differentiation and the middle dot a scalar product (a divergence in this case). In the following the densities and current densities of conserved quantities will be called *conserved densities* and *conserved currents* for short. The space Fourier transform of Eq. (2.3) reads:

$$\dot{\tilde{a}}(\mathbf{q}, t) = -i\mathbf{q} \cdot \tilde{\boldsymbol{j}}(\mathbf{q}, t), \tag{2.4}$$

where the overdot indicates a time derivative and the tilde a Fourier transform, so that the longer the wavelength, the slower is the dynamics of a conserved density. We conclude that for long enough wavelengths, conserved densities are adiabatically decoupled from all the other (zillions of) fast atomic degrees of freedom. Note that in this chapter we are using the concept of *adiabatic decoupling* in two distinct senses, depending on the context: to indicate the decoupling of electronic from nuclear degrees of freedom, and that of hydrodynamic variables from fast atomic ones.

The long-wavelength Fourier components of conserved densities are called *hydrodynamic variables*. In macroscopically homogeneous systems, different wavelengths are decoupled from each other, while, as we have seen, the long wavelengths are adiabatically decoupled from all the other degrees of freedom. Let us suppose there are Q conserved extensive variables. In the case of a mono-atomic fluid, for instance, $Q = 5$, corresponding to mass (or particle number), energy, and the three components of the momentum. In order to simplify the notation, we set the value of the conserved quantities equal to zero, $A^i = 0$, so that their densities, $a^i(\mathbf{r})$, directly refer to the departure from equilibrium, and we indicate by $\boldsymbol{j}^i(\mathbf{r}, t)$ the corresponding currents. At equilibrium, all the conserved densities and currents vanish. Off equilibrium, it will be assumed that the wavelength and the time scale of the disturbances are so long that thermal equilibrium still holds *locally*. That is to say, a local temperature, pressure, and chemical potential can be defined, such that, when combined with the densities of extensive variable, they satisfy a local equation of state.

For small enough deviations from equilibrium, the time derivatives of conserved densities are linear combinations of the densities themselves. In the frequency/wavevector domains this condition can be expressed as

$$-i\omega\tilde{a}^i(\mathbf{q},\omega) = \sum_j \tilde{\Lambda}^{ij}(\mathbf{q},\omega)\,\tilde{a}^j(\mathbf{q},\omega), \qquad (2.5)$$

where the tilde indicates now a space-time Fourier transform: $\tilde{a}(\mathbf{q},\omega) = \int e^{-i(\mathbf{q}\cdot\mathbf{r}-\omega t)}a(\mathbf{r},t)d\mathbf{r}dt$. By combining Eq. (2.5) with the time Fourier transform of Eq. (2.4), we obtain the so-called constitutive equations for the (longitudinal components of the) conserved currents:

$$\tilde{\boldsymbol{j}}^i(\mathbf{q},\omega) = i\frac{\mathbf{q}}{q^2}\sum_j \tilde{\Lambda}^{ij}(\mathbf{q},\omega)\tilde{a}^j(\mathbf{q},\omega). \qquad (2.6)$$

In isotropic media, the $\tilde{\Lambda}$'s are spherically symmetric functions of $\mathbf{q}$, whereas their value at $\mathbf{q} = 0$ vanishes, because a non-vanishing value would imply a non-physical long-range dependence of the currents on density fluctuations, in contrast with our assumption of local thermodynamic equilibrium. The long-wavelength low-frequency limit of the coupling constants can thus be assumed to be $\tilde{\Lambda}^{ij}(\mathbf{q},\omega) \sim q^2\lambda^{ij}$, so that the macroscopic ($\mathbf{q} = 0$) stationary ($\omega = 0$) components of the currents, $\mathbf{J}^i = \frac{1}{\Omega}\int \boldsymbol{j}^i(\mathbf{r})d\mathbf{r}$, are related to the corresponding components of the density gradients, $\mathbf{D}^i = \frac{1}{\Omega}\int \nabla a^i(\mathbf{r})d\mathbf{r}$, through the equations:

$$\mathbf{J}^i = \sum_j \lambda^{ij}\mathbf{D}^j. \qquad (2.7)$$

In the following, the macroscopic component of a current will be indicated as a *flux*.

Let $x^i = \frac{\partial S}{\partial A^i}$ be the intensive variable conjugate to A^i, where S is the system's entropy, and $\chi^{ij} = \frac{1}{\Omega}\frac{\partial A^i}{\partial x^j}$ the corresponding susceptibility. For instance, when A^i is the energy of the system, the corresponding conjugate variable is the inverse temperature, $x^i = 1/T$, while, when A^i represents the number of particles of a given species, one has $x^i = -\mu^i/T$, μ^i being the corresponding chemical potential. The hypothesis of local thermodynamic equilibrium allows defining local values of the intensive variables, and we define *thermodynamic forces* as their average gradients: $\mathbf{F}^i = \frac{1}{\Omega}\int \nabla x^i(\mathbf{r})d\mathbf{r}$. The average density gradients are related to the thermodynamic forces through the susceptibility defined above, as:

$$\mathbf{D}^i = \sum_j \chi^{ij}\mathbf{F}^j. \qquad (2.8)$$

By inserting this relation into Eq. (2.7), one gets:

$$\mathbf{J}^i = \sum_j L^{ij}\mathbf{F}^j, \qquad (2.9)$$

where $L^{ij} = \sum_k \lambda^{ik}\chi^{kj}$. Eq. (2.9) expresses the linear relation between fluxes, the $\mathbf{J}$'s, and thermodynamic affinities, the $\mathbf{F}$'s, for which Onsager derived his celebrated reciprocity relations ($L^{ji} = L^{ij}$) from microscopic reversibility [34–36]. Note that, according to our definition, both the $\mathbf{J}$'s and the $\mathbf{F}$'s in Eq. (2.9) do not depend on the size of the system.

2.2   Linear-response theory

In order to evaluate the L^{ij} phenomenological coefficients appearing in Eq. (2.9), we consider a classical system of N interacting atoms described by the Hamiltonian

$$H^\circ(\Gamma) = \sum_n \frac{1}{2M_n}(\mathbf{P}_n)^2 + V(\mathbf{R}_1, \mathbf{R}_2, \cdots \mathbf{R}_N), \qquad (2.10)$$

where M_n, $\mathbf{R}_n$, and $\mathbf{P}_n$ are the masses, coordinates, and momenta of the n-th particle, $\Gamma = \{\mathbf{R}_n, \mathbf{P}_n\}$ indicates the phase-space coordinates of the entire system, and V is a generic many-body potential. Let us now suppose that the system is subject to an external perturbation that can be described as a linear combination of the conserved densities, $\{a^i(\mathbf{r}; \Gamma)\}$, as:

$$V'(\Gamma, t) = \sum_i \int v^i(\mathbf{r}, t) a^i(\mathbf{r}; \Gamma) d\mathbf{r}, \qquad (2.11)$$

where $a(\mathbf{r}; \Gamma)$ is a phase-space function whose ensemble average is the conserved density,

$$a(\mathbf{r}) = \langle a(\mathbf{r}; \Gamma) \rangle$$
$$= \int a(\mathbf{r}; \Gamma) \mathcal{P}^\circ(\Gamma) d\Gamma, \qquad (2.12)$$

$\mathcal{P}^\circ(\Gamma) \propto e^{-\frac{H^\circ(\Gamma)}{k_B T}}$ is the equilibrium distribution, k_B the Boltzmann constant, and $\{v^i(\mathbf{r}, t)\}$ are time-dependent fields that couple to the conserved densities and vanish at $t = -\infty$, when the system is assumed to be in thermal equilibrium at some temperature T. Of course, conserved currents are also expected values of some phase-space functions, $\boldsymbol{j}(\mathbf{r}) = \langle \boldsymbol{j}(\mathbf{r}; \Gamma) \rangle$. The phase-space functions whose expected values are conserved densities/currents will be referred to as *phase-space samples* of the currents/densities. In the following, when the phase-space dependence of a conserved density/current is explicitly indicated, we will mean a phase-space sample; when it is not a phase-space average will be implied. When a phase-space sample is evaluated along a dynamical trajectory, Γ_t, the sample function will depend on time and on the initial conditions of the trajectory. Averaging with respect to the initial conditions will result in a time-dependent expected value for the conserved densities (or currents):

$$a(\mathbf{r}, t) = \langle a(\mathbf{r}; \Gamma'_t) \rangle_0$$
$$= \int a(\mathbf{r}; \Gamma'_t) \mathcal{P}^\circ(\Gamma_0) d\Gamma_0. \qquad (2.13)$$

In Eq. (2.13) the notation Γ'_t denotes somewhat pedantically that the time evolution in phase space is driven by the perturbed Hamiltonian, $H^\circ + V'$. If it were driven by H°, evidently the value of a would be time-independent. In the following, the notation Γ_t will indicate an unperturbed time evolution. As an example, the phase-space sample of the particle density can be assumed to be $n(\mathbf{r}; \Gamma) = \sum_n \delta(\mathbf{r} - \mathbf{R}_n)$,

the corresponding current is $\boldsymbol{j}(\mathbf{r}, \Gamma) = \sum_n \delta(\mathbf{r} - \mathbf{R}_n)\mathbf{P}_n/M_n$, and a local external potential is described by: $V'(\Gamma, t) = \sum_n v(\mathbf{R}_n, t) = \int v'(\mathbf{r}, t)n(\mathbf{r}; \Gamma)d\mathbf{r}$. Note that sample functions are not necessarily univocally defined. Different functions whose phase-space averages coincide in the long-wavelength limit sample the same hydro-dynamical variable. More on this in Chapter 3.

According to Ref. [21–23], the linear response of the i-th conserved current to the perturbation is:

$$j_\alpha^i(\mathbf{r}, t) = \frac{1}{k_B T} \sum_j \int_{-\infty}^t dt' \int d\mathbf{r}' \left\langle j_\alpha^i(\mathbf{r}, \Gamma_t)\dot{a}^j(\mathbf{r}', \Gamma_{t'}) \right\rangle_0 v^j(\mathbf{r}', t') \tag{2.14}$$

$$= \frac{-1}{k_B T} \sum_{j,\beta} \int_{-\infty}^t dt' \int d\mathbf{r}' \left\langle j_\alpha^i(\mathbf{r}, \Gamma_t)\partial_\beta' j_\beta^j(\mathbf{r}', \Gamma_{t'}) \right\rangle_0 v^j(\mathbf{r}', t') \tag{2.15}$$

$$= \frac{1}{k_B T} \sum_{j,\beta} \int_{-\infty}^t dt' \int d\mathbf{r}' \left\langle j_\alpha^i(\mathbf{r}, \Gamma_t)j_\beta^j(\mathbf{r}', \Gamma_{t'}) \right\rangle_0 \partial_\beta' v^j(\mathbf{r}', t'). \tag{2.16}$$

The second line follows from the first through the continuity equation, Eq. (2.3), while the third line follows after integrating by parts with respect to $\mathbf{r}'$. The notation $\partial_\beta' = \frac{\partial}{\partial r_\beta'}$ has been used.

By integrating Eq. (2.16) all over the space, and assuming space-time homo-geneity as well as isotropy, one recovers Eq. (2.9) with:

$$J_\alpha^i(\Gamma) = \frac{1}{\Omega} \int j_\alpha^i(\mathbf{r}, \Gamma)d\mathbf{r}, \tag{2.17}$$

$$F_\alpha^i(\Gamma) = \frac{1}{\Omega T} \int \partial_\alpha v^i(\mathbf{r}, \Gamma)d\mathbf{r}, \tag{2.18}$$

$$L_{\alpha\beta}^{ij} = \frac{\Omega}{k_B} \int_0^\infty \left\langle J_\alpha^i(\Gamma_t)J_\beta^j(\Gamma_0) \right\rangle_0 dt. \tag{2.19}$$

This completes the derivation of the Green-Kubo formula for transport coeffi-cients, Eq. (2.1), from classical linear-response theory. Onsager's reciprocity rela-tions, $L^{ij} = L^{ji}$ [34, 35], follow from Eq. (2.19) leveraging time-translational invari-ance, $\langle J_\alpha^i(\Gamma_t)J_\beta^j(\Gamma_0)\rangle = \langle J_\alpha^i(\Gamma_0)J_\beta^j(\Gamma_{-t})\rangle$, and micro-reversibility, $\langle J_\alpha^i(\Gamma_t)J_\beta^j(\Gamma_0)\rangle = \langle J_\alpha^i(\Gamma_{-t})J_\beta^j(\Gamma_0)\rangle$.

2.2.1 Einstein-Helfand expression for transport coefficients and the Wiener-Khintchine theorem

The celebrated Einstein's relation between the mean-square displacement of a dif-fusing particle and its velocity auto-correlation function is easily generalized to an arbitrary stochastic process and has in fact been utilized by Helfand [37] to provide an "Einstein-like" expression for transport coefficients.

Let X_t be a stationary stochastic process. One has:

$$\frac{1}{\mathcal{T}} \left\langle \left| \int_0^{\mathcal{T}} X_t dt \right|^2 \right\rangle = 2 \int_0^{\mathcal{T}} \langle X_t X_0 \rangle dt - \frac{2}{\mathcal{T}} \int_0^{\mathcal{T}} \langle X_t X_0 \rangle t \, dt. \tag{2.20}$$

In the large-$\mathcal{T}$ limit, the second term on the right-hand side of Eq. (2.20) can be neglected.

When the stochastic process is the velocity of a Brownian particle, Eq. (2.20) allows one to establish a relation between the diffusion constant of the particle, temperature, and the auto-correlation time of the velocity. When X_t is the heat flux of a macroscopic body, Eq. (2.20) allows one to estimate the thermal conductivity, as given by Eq. (2.1), from the asymptotic behavior of the "energy displacement" $\boldsymbol{\mathcal{D}}(\tau) = \int_0^\tau \mathbf{J}(\Gamma_t)dt$. From Eq. (2.19) we have that

$$
\begin{aligned}
L_{\alpha\beta}^{ij} &= \lim_{\mathcal{T}\to\infty} \frac{\Omega}{k_B} \int_0^{\mathcal{T}} \left\langle J_\alpha^i(\Gamma_t) J_\beta^j(\Gamma_0) \right\rangle_0 \left(1 - \frac{t}{\mathcal{T}}\right) dt \\
&= \lim_{\mathcal{T}\to\infty} \frac{\Omega}{2k_B\mathcal{T}} \left\langle \int_0^{\mathcal{T}} J_\alpha^i(\Gamma_t) \int_0^{\mathcal{T}} J_\beta^j(\Gamma_t)dt \right\rangle_0 .
\end{aligned}
\tag{2.21}
$$

Power Spectrum

Eq. (2.20) can be easily generalized to the finite-frequency regime, to get:

$$
\begin{aligned}
S_{\mathcal{T}}(\omega) &= \frac{1}{\mathcal{T}} \left\langle \left| \int_0^{\mathcal{T}} X_t e^{i\omega t} dt \right|^2 \right\rangle \\
&= 2\mathfrak{Re} \int_0^{\mathcal{T}} \langle X_t X_0 \rangle\, e^{i\omega t} dt + \mathcal{O}(\mathcal{T}^{-1}).
\end{aligned}
\tag{2.22}
$$

This equation expresses the Wiener-Khintchine theorem [38, 39], which states that the expectation of the squared modulus of the Fourier transform of a stationary process is the Fourier transform of its time correlation function, which is usually referred to as the process *power spectral density*,

$$
S(\omega) = \int_{-\infty}^{\infty} \langle X_t X_0 \rangle\, e^{i\omega t} dt,
\tag{2.23}
$$

aka the *power spectrum*. In the following the suffix $\mathcal{T}$ will be neglected for simplicity and its value assumed to be sufficiently large as to be considered infinite. More generally, when several conserved currents interact with each other, one can define the *cross-spectrum* of the conserved fluxes as the Fourier transform of the cross time-correlation functions:

$$
\begin{aligned}
S^{kl}(\omega) &= \int_{-\infty}^{\infty} \langle X_t^k X_0^l \rangle\, e^{i\omega t} dt \\
&= \frac{1}{\mathcal{T}} \mathfrak{Re} \left\langle \int_0^{\mathcal{T}} X_t^k e^{-i\omega t} dt \times \int_0^{\mathcal{T}} X_t^l e^{i\omega t} dt \right\rangle + \mathcal{O}(\mathcal{T}^{-1}).
\end{aligned}
\tag{2.24}
$$

Eqs. (2.20) and (2.22) indicate that the transport coefficients we are after essentially are the zero-frequency value of the (cross-) power spectrum of the corresponding current(s), a fact that will be instrumental in our approach to data analysis, as explained in Chapter 5. Therefore, Eq. (2.19) can be cast into the form:

$$
L^{kl} = \frac{\Omega}{2k_B} S^{kl}(\omega = 0),
\tag{2.25}
$$

where the Cartesian indices have been omitted for clarity.

2.3 Heat transport

The above treatment allows one to compute the linear response of a system at thermal equilibrium to a generic mechanical perturbation. Heat transport is determined by temperature gradients that cannot be described by any mechanical perturbation. The concept of temperature distribution implies that the system is locally at thermal equilibrium over lengths and times large with respect to atomic distances and relaxation times. Temperature affects the physical properties of a system through the Boltzmann distribution function. When the temperature is not constant, $T(\mathbf{r}) = T + \Delta T(\mathbf{r})$ ($|\Delta T| \ll T$), the effects of this inhomogeneity can be formally described by the distribution function:

$$\mathcal{P}(\Gamma) \propto \exp\left[-\int \frac{e(\mathbf{r};\Gamma)}{k_B T(\mathbf{r})} d\mathbf{r}\right] \tag{2.26}$$

$$= \exp\left[-\frac{H^\circ(\Gamma) + V'(\Gamma)}{k_B T}\right], \tag{2.27}$$

where $e(\mathbf{r};\Gamma)$ is an energy (Hamiltonian) density, such that $\int e(\mathbf{r};\Gamma)d\mathbf{r} = H^\circ(\Gamma)$. Eq. (2.11) becomes:

$$V'(\Gamma) = -\frac{1}{T}\int \Delta T(\mathbf{r})e(\mathbf{r};\Gamma)d\mathbf{r} + \mathcal{O}(\Delta T^2). \tag{2.28}$$

Eq. (2.28) shows that the effects of temperature inhomogeneities can be mimicked by a mechanical perturbation coupled to the temperature distribution. From Eqs. (2.9) and (2.17-2.19) we conclude that in a system where the only non-trivial conserved quantity is the energy, the heat (energy) flow is coupled to temperature gradients through the constitutive equation:

$$\mathbf{J}^E = -\kappa \nabla T, \tag{2.29}$$

where the thermal conductivity $\kappa_{\alpha\beta} = L^{EE}_{\alpha\beta}/T^2$ (see Eq. (2.9)) can be expressed by a Green-Kubo relation in terms of the fluctuations of the energy flux as:

$$\boxed{\kappa_{\alpha\beta} = \frac{\Omega}{k_B T^2}\int_0^\infty \left\langle J^E_\alpha(\Gamma_t)J^E_\beta(\Gamma_0)\right\rangle_0 dt} \tag{2.30}$$

and

$$\mathbf{J}^E(\Gamma) = \frac{1}{\Omega}\int \boldsymbol{j}^E(\mathbf{r};\Gamma)d\mathbf{r}. \tag{2.31}$$

In order to obtain an explicit expression for the energy flux from a microscopic expression for the energy density, we multiply the continuity equation, Eq. (2.3), by $\mathbf{r}$ and integrate by parts, to obtain:

$$\mathbf{J}^E(\Gamma) = \frac{1}{\Omega}\int \dot{e}(\mathbf{r};\Gamma_t)\,\mathbf{r}\,d\mathbf{r} \tag{2.32}$$

$$= \frac{1}{\Omega}\int \left[\sum_n \left(\frac{\partial e(\mathbf{r};\Gamma_t)}{\partial \mathbf{R}_n}\cdot \mathbf{V}_n + \frac{\partial e(\mathbf{r};\Gamma_t)}{\partial \mathbf{P}_n}\cdot \mathbf{F}_n\right)\right]\mathbf{r}\,d\mathbf{r}, \tag{2.33}$$

where $\mathbf{F}_n$ is the force acting on the n-th atom, and $\mathbf{V}_n = \frac{\mathbf{P}_n}{M_n}$ its velocity.

The manipulations leading from the continuity equation, Eq. (2.3), to Eq. (2.33) deserve some further comments, as they imply neglecting a boundary term, $\mathbf{J}_{\partial \Omega} = \frac{1}{\Omega} \int_{\partial \Omega} (\boldsymbol{j}(\mathbf{r}) \cdot \hat{\mathbf{n}}) \, \mathbf{r} \, d\mathbf{r}$ (where $\partial \Omega$ is the boundary of the integration volume and $\hat{\mathbf{n}}$ the normal to it), which in general does not vanish in the thermodynamic limit and is ill-defined in periodic boundary conditions (PBC), as it depends on the definition and choice of the unit cell. The correct way of addressing this problem is to work with the Taylor expansion of the space Fourier transform of the continuity equation, Eq. (2.4), and to perform the thermodynamic limit at finite wavelength. The leading non-vanishing term in the Taylor expansion yields Eq. (2.32) without any boundary term in the way.

2.3.1   Energy flux from classical force fields

When atoms interact through a classical force field, $V(\mathbf{R}_1, \mathbf{R}_2, \cdots \mathbf{R}_N)$, an energy density can be defined in terms of local atomic energies as:

$$e(\mathbf{r}, \Gamma) = \sum_n \delta(\mathbf{r} - \mathbf{R}_n) e_n(\Gamma), \tag{2.34}$$

$$e_n(\Gamma) = \frac{(\mathbf{P}_n)^2}{2M_n} + v_n(\{\mathbf{R}\}), \tag{2.35}$$

where the v_n's represent a partition of the total potential energy into local contributions, *i.e.* $\sum_n v_n = V$, with a short-range dependence on the coordinates of the other atoms. In the presence of long-range forces, this condition is effectively guaranteed by local charge neutrality, which we will assume throughout. By inserting Eq. (2.34) into Eq. (2.33), the energy flux can be cast into the form:

$$\mathbf{J}^E(\Gamma) = \frac{1}{\Omega} \left[\sum_n \mathbf{V}_n e_n + \sum_n \mathbf{R}_n \left(\mathbf{F}_n \cdot \mathbf{V}_n + \sum_m \mathbf{V}_m \cdot \frac{\partial v_n}{\partial \mathbf{R}_m} \right) \right] \tag{2.36}$$

Two-body potentials

When the interaction among atoms can be expressed in terms of two-body potentials, one has: $v_m = \frac{1}{2} \sum_n v(\mathbf{R}_n - \mathbf{R}_m)$ and $\mathbf{F}_{nm} = -\frac{1}{2} \nabla_{\mathbf{R}_n} v(\mathbf{R}_n - \mathbf{R}_m)$, where $\mathbf{F}_{nm} = -\frac{\partial v_m}{\partial \mathbf{R}_n}$ is the contribution of the m-th atom to the force acting on the n-th atom, $\sum_m \mathbf{F}_{nm} = \mathbf{F}_n$, and $\mathbf{F}_{nm} = -\mathbf{F}_{mn}$. Here we implicitly assumed that the interaction energy is equally partitioned between atoms m and n. In Chapter 3 we shall see this is not the only possible choice, with far-reaching consequences on the theory of heat transport. The energy flux becomes:

$$\mathbf{J}^E(\Gamma) = \frac{1}{\Omega} \left[\sum_n \mathbf{V}_n e_n + \sum_{n,m} (\mathbf{R}_n - \mathbf{R}_m) \mathbf{F}_{nm} \cdot \mathbf{V}_n \right]. \tag{2.37}$$

Notice that this expression is also well-defined in PBC.

The first term on the right-hand side of Eq. (2.36),

$$\mathbf{J}_c^E = \frac{1}{\Omega} \sum_n \mathbf{V}_n e_n, \tag{2.38}$$
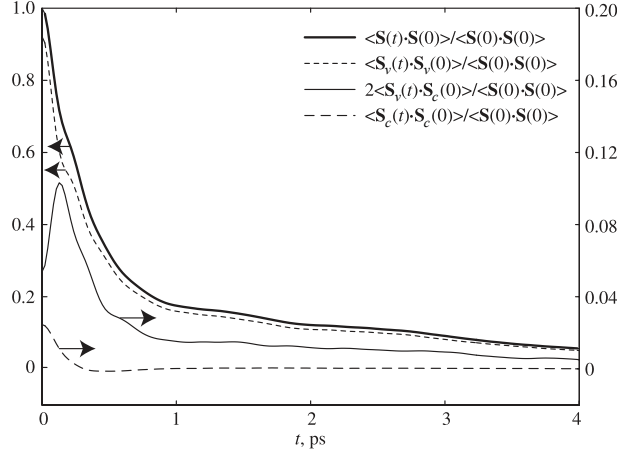
Figure 2.1: Breakdown of the energy flux autocorrelation function $\langle \mathbf{J}^E(t) \cdot \mathbf{J}^E(t) \rangle$ of LJ fcc solid argon at $50\,\mathrm{K}$ into the three terms of Eq. (2.40). Note that the total ACF and the virial component correspond to the left vertical axis, while the cross and convection curves correspond to the right axis. Reproduced from Ref. [40].

is often called *convective* (or *kinetic*) and the second term,

$$\mathbf{J}_v^E = \frac{1}{\Omega} \left[\sum_{n,m} (\mathbf{R}_n - \mathbf{R}_m) \mathbf{F}_{nm} \cdot \mathbf{V}_n \right], \tag{2.39}$$

is often called *virial* (or *potential*). Fan et al. [41] and Carbogno et al. [42], for example, adopt this nomenclature and state that the convective term $\mathbf{J}_c^E$ "*gives no contributions to the conductivity tensor in solids, as mass transport is negligible*". We feel that the wording "convective" is somewhat misleading in this context, as the contribution of the convective flux $\mathbf{J}_c^E$ to the heat conductivity may not vanish even in the absence of convection, especially in softer solid materials. Using Eqs. (2.38) and (2.39), the energy flux autocorrelation function can be split into 3 terms:

$$\langle \mathbf{J}^E(t) \cdot \mathbf{J}^E(0) \rangle = \langle \mathbf{J}_c^E(t) \cdot \mathbf{J}_c^E(0) \rangle + 2 \langle \mathbf{J}_c^E(t) \cdot \mathbf{J}_v^E(0) \rangle + \langle \mathbf{J}_v^E(t) \cdot \mathbf{J}_v^E(0) \rangle. \tag{2.40}$$

Their contributions to thermal conductivity were computed by McGaughey and Kaviany [40] for a LJ fcc argon crystal at $50\,\mathrm{K}$ (the breakdown of $\langle \mathbf{J}^E(t) \cdot \mathbf{J}^E(0) \rangle$ into the three terms of Eq. (2.40) is shown in Fig. 2.1). They found that while the convection contribution $\langle \mathbf{J}_c^E(t) \cdot \mathbf{J}_c^E(0) \rangle$ was indeed small ($\sim 1\%$), the contribution of the cross term $2\langle \mathbf{J}_c^E(t) \cdot \mathbf{J}_v^E(0) \rangle$ is not insignificant ($\sim 10\%$). The relative contributions of the convective and cross terms are expected to increase as the temperature goes up and anharmonic effects inhibit phononic conduction. While the convective term may not be as important for materials with higher thermal conductivity, in general, its contribution and that of the cross term should be checked before assuming they are negligible. Some further comments on this issue are reported in Appendix A.

In the literature the nomenclature is often confusing, and the relative contributions of each term not very well established. For example, Vogelsang et al. [43]

divide the energy flux in two terms [44]: a "*kinetic*" part, defined as

$$\mathbf{J}_k^{E\prime} = \frac{1}{\Omega} \frac{(\mathbf{P}_n)^2}{2M_n} \mathbf{V}_n, \tag{2.41}$$

and a "*potential*" part, defined as

$$\mathbf{J}_p^{E\prime} = \frac{1}{\Omega} \left[\sum_n v_n(\{\mathbf{R}\})\mathbf{V}_n + \sum_{n,m}(\mathbf{R}_n - \mathbf{R}_m)\mathbf{F}_{nm} \cdot \mathbf{V}_n \right]. \tag{2.42}$$

They find that $\mathbf{J}_k^{E\prime}$ is negligible in solids, where atomic diffusion does not occur. Kinaci et al. [45], instead, use the Einstein formulation and define a "*kinetic*" term

$$\mathbf{J}_k^{E\prime\prime} = \frac{1}{\Omega} \left[\frac{(\mathbf{P}_n)^2}{2M_n} \mathbf{V}_n + \sum_{n,m}(\mathbf{R}_n - \mathbf{R}_m)\mathbf{F}_{nm} \cdot \mathbf{V}_n \right], \tag{2.43}$$

and a "*potential*" term

$$\mathbf{J}_p^{E\prime\prime} = \frac{1}{\Omega} \sum_n v_n(\{\mathbf{R}\})\mathbf{V}_n, \tag{2.44}$$

and conclude that in perfect solid systems, where diffusion is highly improbable, $\mathbf{J}_p^{E\prime\prime}$ contribution to thermal conductivity is negligible.

Finally, an alternative definition of the heat flux can be used when dealing with solids [46]:

$$\mathbf{J}^E(\Gamma) = \frac{1}{\Omega} \sum_{n,m}(\mathbf{R}_n^0 - \mathbf{R}_m^0)\mathbf{F}_{nm} \cdot \mathbf{V}_n, \tag{2.45}$$

where $\mathbf{R}_n^0$ denotes the average atomic position of atom n. One should not confuse this expression with neglecting the convection part of the heat current. For a solid, Eq. (2.45) will give the same thermal conductivity as Eq. (2.37). In Appendix A we present a simple demonstration of this statement, by exploiting the gauge invariance principle that will be introduced in Ch. 3.

Many-body potentials

In the case of a many-body potential interaction, if the atomic potential energy can be written as a function of the distance vectors $\mathbf{R}_{nm} = \mathbf{R}_n - \mathbf{R}_m$, as $v_n = v_n(\mathbf{R}_{1n}, \mathbf{R}_{2n}, \cdots, \mathbf{R}_{Nn})$, the force acting on atom n can be written as [41, 47]:

$$\begin{aligned}
\mathbf{F}_n &= -\sum_m \frac{\partial v_m}{\partial \mathbf{R}_n} = \sum_m \sum_{p \neq n} \frac{\partial v_m}{\partial \mathbf{R}_{pn}} \\
&= \sum_m \sum_{p \neq n} \left(\frac{\partial v_m}{\partial \mathbf{R}_{mn}}\delta_{pm} + \frac{\partial v_m}{\partial \mathbf{R}_{pn}}\delta_{mn} \right) \\
&= -\sum_{m \neq n} \left(\frac{\partial v_n}{\partial \mathbf{R}_{nm}} - \frac{\partial v_m}{\partial \mathbf{R}_{mn}} \right).
\end{aligned} \tag{2.46}$$

For example, for the Tersoff [48] and Swillinger-Weber [49] potentials, Fan et al. [41] obtain the following definition for the virial energy flux:

$$\mathbf{J}_v^E = \sum_n \sum_{n \neq m} \mathbf{R}_{nm} \left(\frac{\partial v_m}{\partial \mathbf{R}_{mn}} \cdot \mathbf{V}_n \right), \tag{2.47}$$

equivalent to the one obtained by Hardy [50], and they show that other two-body like formulations widely reported in the literature may give wrong results, especially in low-dimensional systems.

2.3.2 Multi-component fluids

In a multi-component fluid there is one conserved quantity (the particle number) per atomic species, plus the total energy and the three Cartesian components of the total momentum. The momentum densities are mass currents: the mass flux is therefore the total momentum, which vanishes in the center of mass reference frame. The transverse components of the momentum densities are decoupled from the other conserved densities [51], while the longitudinal one can be assumed to coincide with the total momentum in the long-wavelength limit. Momentum conservation thus constrains the number of fluxes interacting with the energy flux in Eq. (2.9) to $Q - 1$, Q being the number of atomic species, so that the resulting dimension of the matrix of Onsager coefficients, L, is $Q \times Q$. The heat flux is defined as the non-convective component of the energy flux, *i.e.* the value of the latter in the absence of mass transport, that is to say when all the particle fluxes vanish.[1] By imposing this condition in Eq. (2.9), with $\mathbf{J}^1 \equiv \mathbf{J}^E$, and $\mathbf{J}^q$ ($q = 2, \ldots Q$) being independent particle fluxes, the thermal conductivity, defined by the Fourier's law as the ratio of the heat flux over the temperature gradient, is given by:

$$\kappa = \frac{1}{T^2 \left(L^{-1} \right)^{11}}. \tag{2.48}$$

This expression can be proved to be invariant under *any* non-singular linear transformation of the independent particle fluxes.

Two-component fluids

For instance, in the case of a two-component liquid, energy and particle fluxes are coupled as in:

$$\begin{aligned}
\mathbf{J}^E &= L^{EE} \nabla \left(\frac{1}{T} \right) + L^{EQ} \nabla \left(\frac{\mu}{T} \right), \\
\mathbf{J}^Q &= L^{EQ} \nabla \left(\frac{1}{T} \right) + L^{QQ} \nabla \left(\frac{\mu}{T} \right),
\end{aligned} \tag{2.49}$$

where $\mathbf{J}^Q$ is the particle flux of one of the two species (say, the second), and μ the corresponding chemical potential [52]. By imposing that the particle current

---

[1]It is unfortunate, but inevitable due to common usage, that this definition of non-convective flux clashes with the one given in Sec. 2.3.1, Eqs. (2.37-2.39).

vanishes, the resulting thermal conductivity is:

$$\kappa = \frac{1}{T^2} \left(L^{EE} - \frac{(L^{EQ})^2}{L^{QQ}} \right).$$

(2.50)

3

Gauge invariance of heat transport coefficients

It has long been thought that the inherent indeterminacy of any quantum mechanical expression for the energy density would hinder the evaluation of thermal transport coefficients from equilibrium *ab initio* molecular dynamics (AIMD), using the Green-Kubo formalism. In classical molecular dynamics this goal is achieved by decomposing the total energy of an extended system into *localised* atomic contributions and by deriving from this decomposition an explicit, and allegedly unique, expression for the energy flux [53].

In density-functional theory (DFT), as well as in any other quantum mechanical approach, this decomposition is not possible, and it has therefore long been thought that *"the Green-Kubo relation does not serve our purposes* [of computing the thermal conductivity] *because in first-principles calculations it is impossible to uniquely decompose the total energy into individual contributions from each atom"* [54].

In this chapter, we confute this prejudice thanks to the discovery of a *gauge invariance* principle, that ensures that the Green-Kubo formula is well-defined, even though the microscopic quantities whence it is derived are not [A, 31]. Energy densities and fluxes are indeed ill-defined, in classical no less than in quantum mechanics, however the transport coefficients derived from them do not depend on their microscopic definition, as long as the last complies with energy *extensivity* and *conservation*. In Section 3.1, we show the nature of this indeterminacy and we demonstrate it in the case of classical MD simulations, providing a numerical example. In Section 3.2, we introduce the concept of gauge invariance of thermal transport coefficients and prove it both theoretically and numerically. In Section 3.3, we treat the specific case of molecular fluids and give a perspective on how the gauge invariance property may be exploited to define equivalent formulations for the heat currents. These ideas may reveal to be very handy in optimising the statistical properties of the heat currents: a task especially useful in view of the *ab initio* calculation of thermal conductivity, and that we will exploit later on. Finally, Section 3.4 concludes this chapter by giving some future perspectives.
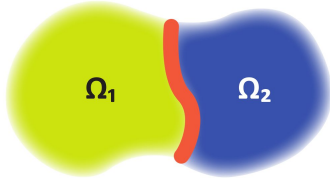
$$E(\Omega_1 \cup \Omega_2) = E(\Omega_1) + E(\Omega_2) + W_{12}$$
$$\stackrel{?}{=} \mathcal{E}(\Omega_1) + \mathcal{E}(\Omega_2)$$

Figure 3.1: The energy of an isolated system is the sum of the energies of its subsystems (as defined when they are isolated as well) plus the interaction among them, W_{12}, whose magnitude scales as the area of the interface, depicted in red. When defining the energies of individual subsystems, $\mathcal{E}$, W_{12} has to be arbitrarily partitioned among them.

3.1   Microscopic ill-definedness

It is often implicitly assumed that the well-definedness of thermal transport coefficients would stem from the uniqueness of the decomposition of the system's total energy into localised, atomic, contributions. This assumption is manifestly incorrect, as any decomposition leading to the same value for the total energy as Eq. (2.35) should be considered as legitimate. The difficulty of partitioning a system's energy into subsystems' contributions is illustrated in Fig. 3.1, which depicts a system made of two interacting subsystems. When defining the energy of each of the two subsystems, an arbitrary decision has to be made as to how the interaction energy is partitioned. In the case depicted in Fig. 3.1, for instance, the energy of each of the two subsystems can be defined as $\mathcal{E}(\Omega_i) = E(\Omega_i) + \frac{1}{2}(1 \pm \lambda)W_{12}$, where $E(\Omega_i)$ are the energies of the two isolated subsystems, W_{12} their interaction energy, and λ an arbitrary constant. In the thermodynamic limit, when all the subsystems' energies are much larger than the interaction between any pairs of them, the value of the λ constant is irrelevant. When it comes to defining energy densities (*i.e.* energies of infinitesimal portions of a system) or atomic energies, instead, the magnitude of the interaction between different subsystems is comparable to their energies, which become therefore intrinsically ill-defined.

Let us consider a mono-atomic fluid interacting through pair potentials, $v(|\mathbf{R}_n - \mathbf{R}_m|)$, and define the atomic energies as [A, 55]:

$$e_{\gamma,n}(\Gamma) = \frac{1}{2M_n}(\mathbf{P}_n)^2 + \frac{1}{2}\sum_{m \neq n} v(|\mathbf{R}_n - \mathbf{R}_m|)(1 + \gamma_{nm}), \qquad (3.1)$$

where $\gamma_{nm} = -\gamma_{mn}$ is *any* antisymmetric matrix. As the inter-atomic potential appearing in Eq. (3.1) is symmetric with respect to the atomic indices, it is clear that the sum of all the atomic energies does not depend on γ, thus making any choice of γ equally permissible. This trivial observation has deep consequences on the theory of thermal fluctuations and transport, because the value of the macroscopic energy flux, instead, depends explicitly on γ, thus making one fear that the resulting transport coefficients would depend on γ as well. Using the same manipulations that lead from Eqs. (2.34) and (2.35) to Eq. (2.36), for any choice of the γ matrix in

Eq. (3.1), a corresponding expression for the macroscopic energy flux can be found, reading [A, 55]:

$$\mathbf{J}_\gamma^E = \mathbf{J}^E + \frac{1}{2\Omega} \sum_{n,m \neq n} \gamma_{nm} \Big(v_{nm} \mathbf{V}_n + \big(\mathbf{V}_n \cdot \nabla_{\mathbf{R}_n} v_{nm} \big)(\mathbf{R}_n - \mathbf{R}_m) \Big), \qquad (3.2)$$

where $v_{nm} = v(|\mathbf{R}_n - \mathbf{R}_m|)$.

### 3.1.1 An example from classical MD

In order to illustrate this state of affairs, we have performed classical MD simulations for a Lennard-Jones monoatomic fluid described by the inter-atomic potential $v(R) = 4\varepsilon \left[\left(\frac{\sigma}{R} \right)^{12} - \left(\frac{\sigma}{R} \right)^6 \right]$ at temperature $T = 1.86 \frac{\epsilon}{k_B}$ and density $\rho = 0.925\sigma^{-3}$, using cubic simulation cells containing 256 atoms in the iso-choric microcanonical ensemble, with the LAMMPS package [56]. We computed different definitions of the energy flux of Eq. (3.2), by choosing γ matrices constructed in two different ways, according to the (arbitrary) prescriptions:

$$\gamma_{IJ} = \begin{cases} \frac{1}{2}(A_{IJ} - A_{JI}) & \begin{array}{l} \text{where the matrix elements of } A \text{ are drawn} \\ \text{from a uniform deviate in the } [0, \lambda] \text{ interval.} \end{array} \quad (1) \\ \\ 0, +\lambda, -\lambda & \text{according to whether } I = J, I > J, \text{ or } I < J. \quad (2) \end{cases} \quad (3.3)$$

In Fig. 3.2(a) we display the resulting macroscopic energy-flux autocorrelation functions, $\langle \mathbf{J}_\gamma^E(t) \cdot \mathbf{J}_\gamma^E(0) \rangle$, that dramatically depend on the definition of the γ matrix in Eqs. (3.1) and (3.2). Notwithstanding, the integrals of all these time correlation functions tend to the same limit at large integration times, as shown in Fig. 3.2(b).

The ill-definition of the atomic energies and of the heat current was already noticed by some authors. Schelling et al. [57] computed the thermal conductivity of Stillinger-Weber [49] silicon and noticed that it was fairly insensitive to the particular definition used, and concluded that the fact that there is no rigorous and unique definition is not a serious impediment to using the GK method. Ten years later, Howell [58] studied the same system more extensively, and found that the energy decomposition in the three-body interaction term gives a negligible contribution to the computed thermal conductivity, even though he did not recognise the ill-definition of the two-body atomic energy term.

How is it that different definitions of the energy flux would lead to the same value for the thermal conductivity? The fundamental origin of this conundrum involves two intrinsic properties of the total energy: *extensivity* and *conservation*, that lead us to the discovery of a gauge invariance principle for thermal transport coefficients.
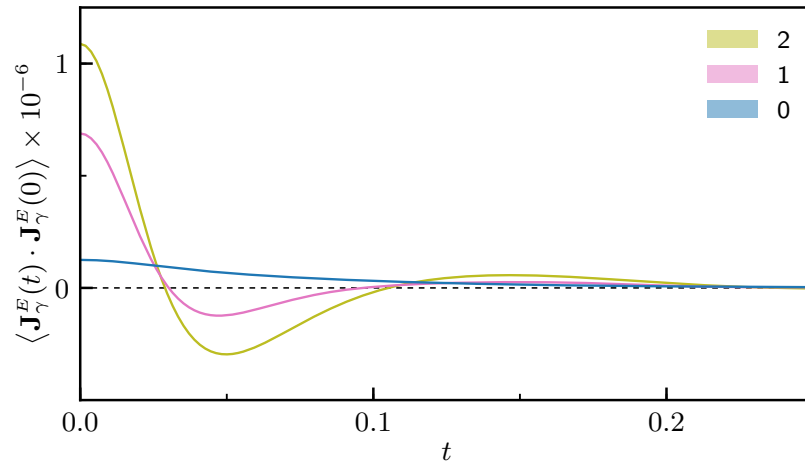
(a)
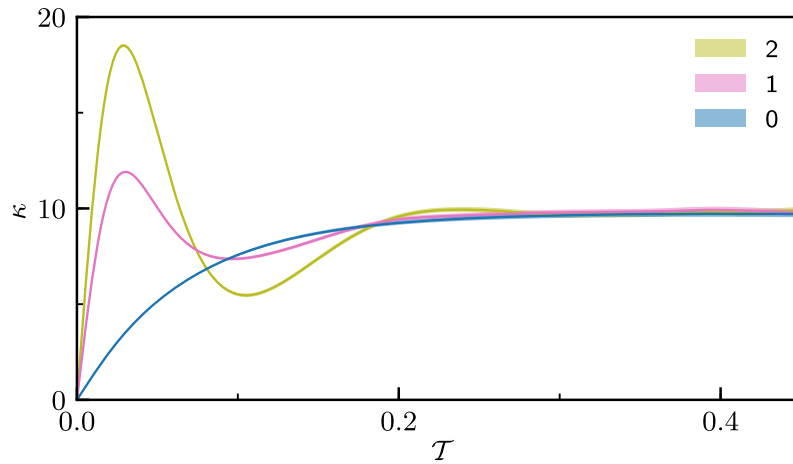
(b)

Figure 3.2: (a) Time correlation functions of the modified macroscopic energy flux of a Lennard-Jones fluid, at the conditions described in the text, as defined in Eq. (3.2), for different definitions of the γ matrix (see text). The "0" line refers to the standard definition ($\gamma = 0$), whereas the labels "1" and "2" correspond to the two (arbitrary) definitions of γ given in Eq. (3.3). (b) Integral of the time correlation functions displayed in Fig. 3.2(a), multiplied by the prefactor appearing in the GK relation, Eq. (2.30), as a function of the upper limit of integration. The parameters used are $\lambda_1 = 10$ and $\lambda_2 = 2.5$. The barely visible shaded area surrounding each line is an indication of the error bars, as estimated by standard block analysis. Units are Lennard-Jones units ($M = \sigma = \varepsilon = 1$). Reproduced from Ref. [A].

3.2 Gauge invariance

In order to get insight into this remarkable invariance property, let us inspect the difference between the generalized flux in Eq. (3.2) and the standard expression of Eq. (2.36):

$$\Delta \mathbf{J}_\gamma^E = \mathbf{J}_\gamma^E - \mathbf{J}^E = \frac{\mathrm{d}}{\mathrm{dt}} \frac{1}{4\Omega} \sum_{n,m\neq n} \gamma_{nm}\, v(|\mathbf{R}_n - \mathbf{R}_m|)(\mathbf{R}_n - \mathbf{R}_m). \qquad (3.4)$$

We see that the two different expressions for the macroscopic energy flux differ by a total time derivative of a bounded phase-space vector function. In the following, we show that this is a consequence of energy conservation and extensivity and a sufficient condition for the corresponding thermal conductivities to coincide.

The very possibility of defining an energy current density, from which the energy fluxes of Eq. (2.36) and (3.2) ultimately depend, stems from energy extensivity, *i.e.* the energy of a macroscopic sample of matter of volume Ω can be written as the integral of an energy density, $e(\mathbf{r})$:

$$E[\Omega] = \int_\Omega e(\mathbf{r})d\mathbf{r}. \qquad (3.5)$$

Along the same considerations illustrated in Fig. 3.1, the energy density appearing in Eq. (3.5) is not uniquely defined: any two densities $e'(\mathbf{r}, t)$ and $e(\mathbf{r}, t)$, whose integrals over a macroscopic volume differ by a quantity that scales as the volume boundary, should be considered as equivalent. This equivalence can be expressed by the condition that two equivalent densities differ by the divergence of a (bounded) vector field:

$$e'(\mathbf{r}, t) = e(\mathbf{r}, t) - \nabla \cdot \boldsymbol{p}(\mathbf{r}, t). \qquad (3.6)$$

In a sense, two equivalent energy densities can be thought of as different *gauges* of the same scalar field.

Energy is also conserved: because of this, for any given gauge of the energy density, $e(\mathbf{r}, t)$, an energy current density can be defined, $\boldsymbol{j}(\mathbf{r}, t)$, so as to satisfy the continuity equation, Eq. (2.3):

$$\dot{e}(\mathbf{r}, t) = -\nabla \cdot \mathbf{j}_e(\mathbf{r}, t). \qquad (3.7)$$

By combining Eqs. (3.6) and (3.7) we see that energy current densities and macroscopic fluxes transform under a gauge transformation as:

$$\boldsymbol{j}'(\mathbf{r}, t) = \boldsymbol{j}(\mathbf{r}, t) + \dot{\boldsymbol{p}}(\mathbf{r}, t), \qquad (3.8)$$

$$\mathbf{J}'(t) = \mathbf{J}(t) + \dot{\mathbf{P}}(t), \qquad (3.9)$$

where $\mathbf{P}(t) = \frac{1}{\Omega} \int \boldsymbol{p}(\mathbf{r}, t)d\mathbf{r}$. We conclude that the macroscopic energy fluxes in two different energy gauges differ by the total time derivative of a bounded phase-space vector function.

We now show that the energy fluxes of the same system in two different energy gauges, e and e', differing by a bounded total time derivative, as in Eq. (3.9), result in the same heat conductivity, as given by the Green-Kubo formula, Eq. (2.30). More generally, the Onsager coefficients coupling two fluxes, $\mathbf{J}^1$ and $\left(\mathbf{J}^1\right)'$, do not depend on the gauge of either one of them. In fact, let $\left(\mathbf{J}^1\right)' = \mathbf{J}^1 + \dot{\mathbf{P}}$; one has:

$$
\begin{aligned}
\left(L^{11}\right)' &= \frac{\Omega}{2k_B} \int_{-\infty}^{+\infty} \left\langle \left(\mathbf{J}^1(t) + \dot{\mathbf{P}}(t)\right) \cdot \left(\mathbf{J}^1(0) + \dot{\mathbf{P}}(0)\right) \right\rangle dt \\
&= L^{11} + \frac{\Omega}{2k_B} \left[\left\langle \mathbf{P}(t) \cdot \dot{\mathbf{P}}(0) \right\rangle \Big|_{-\infty}^{+\infty} + 2\left\langle \mathbf{P}(t) \cdot \mathbf{J}^1(0) \right\rangle \Big|_{-\infty}^{+\infty} \right],
\end{aligned}
\tag{3.10}
$$

where we used the property that classical auto-correlation functions are even in time. The expectation of the time-lagged products in Eq. (3.10) factorises into the products of two independent expectations at large time lag. As the equilibrium expectations of both a total time derivative and a current vanish, we conclude that $\left(L^{11}\right)' = L^{11}$. Heat conductivities computed in different energy gauges coincide, as they must on physical grounds. A slight generalisation of this argument, also using microscopic reversibility as in Ref. [34, 35], allows us to conclude that $\left(L^{12}\right)' = L^{12}$ and that, in general, $\kappa' = \kappa$.

We summarise the gauge invariance principle with a theorem.

Theorem 1 (Gauge invariance). *Two energy fluxes that differ by a total time derivative of a bounded function result in the same thermal conductivity (Onsager coefficient).*

3.2.1 Alternative proof

An alternative proof of the gauge invariance principle of the Onsager coefficients can be obtained using the Lemma described by Marcolongo et al. [31].

Lemma 1 (Marcolongo et al.). *Let $\mathbf{J}^A$ and $\mathbf{J}^B$ be two macroscopic fluxes defined for the same system, and $\mathbf{J}^C = \mathbf{J}^A + \mathbf{J}^B$ be their sum. The corresponding Onsager coefficients[1], L^A, L^B, and L^C satisfy the relation:*

$$
\left| L^C - L^A - L^B \right| \leq 2\sqrt{L^A L^B}
\tag{3.11}
$$

Proof. The Einstein-Helfand relation (Eq. (2.21)) corresponding to a flux $\mathbf{J}^X$ states that

$$
L^X = \lim_{\mathcal{T} \to \infty} \frac{\left\langle |\boldsymbol{\mathcal{D}}^X(\mathcal{T})|^2 \right\rangle}{\mathcal{T}},
\tag{3.12}
$$

where $\boldsymbol{\mathcal{D}}^X(\mathcal{T}) = \int_0^{\mathcal{T}} \mathbf{J}^X(t) dt$ is the displacement associated with the flux $\mathbf{J}^X$. It follows that:

$$
L^C = L^A + L^B + \lim_{\mathcal{T} \to \infty} \frac{2\left\langle \boldsymbol{\mathcal{D}}^A(\mathcal{T}) \cdot \boldsymbol{\mathcal{D}}^B(\mathcal{T}) \right\rangle}{\mathcal{T}}.
\tag{3.13}
$$

---

[1]For the sake of simplicity, with L^X we indicate the $(1, 1)$ component of the Onsager matrix, built using J^X.

Canonical averages of products of phase-space functions can be seen as scalar products [59, 60]:[2] therefore, thanks to the Cauchy-Schwartz inequality, we have that $\lim_{\mathcal{T}\to\infty} \frac{2\langle \boldsymbol{\mathcal{D}}^A(\mathcal{T})\cdot\boldsymbol{\mathcal{D}}^B(\mathcal{T})\rangle}{\mathcal{T}} \leq 2\sqrt{L^A L^B}$, that proves the theorem. $\qquad\square$

Proof (alternative). Alternatively, we can express the Onsager coefficients as the zero-frequency value of the corresponding power spectrum (or cross spectrum), as in Eq. (2.25), *i.e.* $L^X \propto S^{XX}(\omega = 0)$. We obtain:

$$
\begin{aligned}
S^{CC}(\omega = 0) &= \int_{-\infty}^{\infty} \langle J^C(t) J^C(0)\rangle dt \\
&= \int_{-\infty}^{\infty} \left(\langle J^A(t) J^A(0)\rangle + \langle J^B(t) J^B(0)\rangle + 2\langle J^A(t) J^B(0)\rangle \right) dt \\
&= S^{AA}(\omega = 0) + S^{BB}(\omega = 0) + 2S^{AB}(\omega = 0),
\end{aligned}
\tag{3.15}
$$

where we used the fact the $\langle J^A(t) J^B(0)\rangle = \langle J^B(t) J^A(0)\rangle$, and from Eqs. (2.24) we have:

$$
S^{AB}(\omega = 0) = \left\langle \frac{\int_0^{\mathcal{T}} J^A(t)dt}{\sqrt{\mathcal{T}}} \frac{\int_0^{\mathcal{T}} J^B(t)dt}{\sqrt{\mathcal{T}}} \right\rangle + \mathcal{O}(\mathcal{T}^{-1}).
\tag{3.16}
$$

Thanks to the Schwartz inequality (Eq. (3.14)), we must have that

$$
0 \leq \left| S^{AB}(\omega = 0) \right| \leq \sqrt{\left\langle \frac{1}{\mathcal{T}} \left(\int_0^{\mathcal{T}} J^A(t)dt \right)^2 \right\rangle} \sqrt{\left\langle \frac{1}{\mathcal{T}} \left(\int_0^{\mathcal{T}} J^B(t)dt \right)^2 \right\rangle}
$$
$$
= \sqrt{S^{AA}(\omega = 0) S^{BB}(\omega = 0)},
\tag{3.17}
$$

for any $\mathcal{T} > 0$. By letting $\mathcal{T} \to \infty$, Eq. (3.11) follows from Eq. (3.15) and (3.17). $\quad\square$

Thanks this theorem, if we define $\mathbf{J}'(t)$ as in Eq. (3.9), we shall have that $\left| \kappa' - \kappa - \kappa_{\dot{\mathbf{P}}} \right| \leq 2\sqrt{\kappa \kappa_{\dot{\mathbf{P}}}}$. Since $\dot{\mathbf{P}}$ is a bounded function and using the Einstein-Helfand relation (Eq. 2.21), we have that $\kappa_{\dot{\mathbf{P}}} = \lim_{\mathcal{T}\to\infty} \frac{\langle |\dot{\mathbf{P}}| \rangle}{\mathcal{T}} = 0$, hence $\kappa = \kappa'$.

An simple example of application of the gauge invariance theorem is presented in Appendix A, where we show a way to prove the equivalence of two definitions of the energy currents in solids, Eq. (2.36) and (2.45).

---

[2]A simple idea is the following. Let us consider two random variables, X and Y, and $Z = (X + aY)^2$, where $a \in \mathbb{R}$ is a constant. By definition Z is not negative, and $0 \leq \langle Z\rangle = \langle X^2\rangle + a^2\langle Y^2\rangle + 2a\langle XY\rangle$. If we take $a = -\frac{\langle XY\rangle}{\langle Y^2\rangle}$, we obtain the Schwartz inequality

$$
|\langle XY\rangle| \leq \sqrt{\langle X^2\rangle}\sqrt{\langle Y^2\rangle}.
\tag{3.14}
$$

3.3   Molecular fluids

In a one-component molecular fluid such as liquid water or, say, ethanol, there are in general Q fluxes interacting with each other through Onsagers' Eq. (2.9), where Q is the number of atomic species in a molecule. The requirement that atoms are bound in molecules of fixed composition, however, sets a number of constraints that substantially simplify the treatment of heat transport, making the molecular case similar to the one-component one.

Let us consider a molecule of chemical formula $A_{N_A} B_{N_B} \cdots$, where $A, B, \cdots$ indicate atomic species, and $N_A, N_B, \cdots$ the corresponding atomic stoichiometric indices. For each atomic species we define the normalised number flux as:

$$\mathbf{J}^X = \frac{1}{N_X} \sum_{n \in X} \mathbf{V}_n. \tag{3.18}$$

If we indicate by M_X the atomic mass of species X, momentum conservation requires that $\sum_X M_X N_X \mathbf{J}^X = 0$ in the center-of-mass reference frame. The flux $\mathbf{J}^{XY} = \mathbf{J}^X - \mathbf{J}^Y$ is the total time derivative of a bounded vector, because its integral is the sum over all the molecules of the difference between the average atomic positions of either species within a same molecule, which is obviously bounded if molecules do not dissociate. As any number flux $\mathbf{J}^X$ can be expressed as a linear combination of the total momentum and of several $\mathbf{J}^{XY}$ fluxes, each of them is the total time derivative of a bounded vector. Therefore, by the gauge invariance theorem, the Onsager coefficient coupling any of these atomic fluxes with any other or with the energy flux vanishes. We conclude that energy is the only relevant conserved quantity relevant for heat transport in a molecular fluid, and that the energy-flux autocorrelation function directly yields the thermal conductivity, as in Eq. (2.1).

3.4   Outlook

The discovery of the gauge invariance principle provides the theoretical foundation for the formulation of a microscopic theory of adiabatic heat transport in the framework of density functional theory (DFT). The first such formulation is presented in Chapter 4.

Furthermore, this principle opens the way to designing the definition of the local energy (both in terms of atomic energies or energy densities), so as to optimise the convergence of the thermal conductivity estimator. Lemma 1, Eq. (3.11), ensures that if a flux $\mathbf{J}^B$ does not contribute to the conductivity (*i.e.* it has a vanishing GK integral, $L^B = 0$), it is possible to the define a new flux $\mathbf{J}^C = \mathbf{J}^A + \mathbf{J}^B$ that will yield the same conductivity of $\mathbf{J}^A$. Even though $L^C = L^A$, the statistical properties of two such equivalent currents need not be the same, in that the fluctuations of their correlation functions will be different, and the resulting GK integral, Eq. (2.30)

will depend differently on the upper limit of integration, as it was the case in the example shown in Fig. 3.2. We shall see that in the particular case of DFT thermal transport, for some peculiar systems, the natural definition of energy density and flux may make the estimate of the thermal conductivity very difficult, due to the large statistical fluctuations of the correlation functions. In this cases, the gauge invariance principle can come to the rescue.

Besides, the general concept of gauge invariance of heat conductivity will likely apply to other transport properties as well, such as ionic conduction, viscosity, and many others [61], and/or simulation methodologies, such as those based on a neural-network representation of interatomic potentials, which hold the promise of a strong and long-lasting impact on molecular simulations.

4

Density-functional theory of adiabatic heat transport

CONTENTS

The advent of density-functional theory (DFT) [25–27] has marked the start of a new era for the quantum modeling of materials. DFT enables the computation of interatomic forces entirely from first principles using the chemical composition and the fundamental laws of nature as the sole ingredients, without any need to leverage experimental knowledge of these interactions. Its combination with classical molecular dynamics, both in the Born-Oppenheimer or Car-Parrinello flavours [62, 63], had a groundbreaking impact in a wide number of physical problems.

Nevertheless, for the reasons discussed in the previous chapters, DFT has long been thought to be incompatible with the GK theory of thermal transport, and *ab initio* simulations of heat transport have only been performed using the Boltzmann transport equation, when possible, or non-equilibrium MD approaches. The gauge invariance principle introduced in Chapter 3 finally gives us a rigorous way of deriving an expression for the energy flux directly from DFT, without introducing any *ad hoc* ingredients.

In this chapter, we start by summarising the most recent *ab initio* methods for the computation of thermal conductivity, in Section 4.1. In Section 4.2 we briefly review the first-principles GK theory of thermal transport developed by Marcolongo et al. [31], that will be applied later to the simulation of silica glass. Finally, in Section 4.3 we conclude with some development prospects.

4.1   First-principles simulation methods

In insulators heat transport is determined by the dissipative dynamics of atoms, the electrons following adiabatically in their ground state, a regime often referred to as atomic or *adiabatic heat conduction*. Different approaches are available to model heat conduction in these systems (for a recent review see Ref. [64]): the main ones are the *Boltzmann's transport equation* (BTE) and *molecular dynamics* (MD), both in its non-equilibrium and equilibrium flavors.

The *Boltzmann's transport equation* (BTE) [19, 65] is the method of choice for crystals well below melting, where long-lived phonons are clearly identified as the heat carriers. In this case density-functional perturbation theory [66–68] enables one to compute accurate phonon frequencies [69] and lifetimes, [70, 71] and thus implement the BTE entirely from first principles [28]. The flexibility and accuracy of *ab initio* BTE are such that this approach is being successfully used to screen new materials for custom-designed properties, such as high thermal conductivity for passive cooling [72, 73] or low thermal conductivity for thermoelectric energy conversion [74, 75]. Recent self-consistent and variational approaches to solve the BTE beyond the relaxation-time approximation [76] are also providing fresh and deep insight into the collective character of heat transport [76–79]. Yet, the applicability of *ab initio* BTE is restricted to periodic systems consisting of a small number of atoms per unit cell, and is severely limited by its own inherent approximations: as the temperature increases, anharmonic effects become so important as to eventually make it break down well below melting [80], while the BTE simply does not apply to glasses and liquids, where phonons are not even defined [81] .

Molecular dynamics (MD) [81, 82] is set to overcome these limitations. In non-equilibrium MD (NEMD) [18, 83], temperature gradients or heat fluxes are explicitly imposed on the virtual sample, and the thermal conductivity is estimated from the resulting value of the conjugate variable (flux or gradient). In the so-called *approach to equilibrium* (AEMD) methodology of Lampin et al. [84] the system is first prepared in an out-of-equilibrium state, characterized by an inhomogeneous temperature distribution, and the thermal conductivity is evaluated from the time it takes for the system to equilibrate. NEMD and AEMD lend themselves to a straightforward quantum-mechanical implementation [54, 85] using *ab initio* molecular dynamics (AIMD). For example, Stackhouse et al. [54] computed the thermal conductivity of periclase MgO using a method devised by Müller-Plathe [83], *i.e.* by imposing a temperature gradient to the system, and evaluating the ratio between the heat flux and the resulting temperature gradient. Bouzid et al. [85] combined AEMD with AIMD to simulate thermal transport in a $GeTe_4$ glass, while Puligheddu et al. [86] further generalized and applied it to crystalline and nano-structured MgO. However, these methods may be both affected by non-linear effects, due to the strength of the temperature gradient to be imposed [57, 87] and by finite-size/finite-time effects that require long simulation times and difficult extrapolations to approach the thermodynamic limit [87–91].

The combination of equilibrium molecular dynamics (EMD), based on the

Green-Kubo theory, with DFT, has been successfully accomplished very recently by Marcolongo et al. [31], thanks to the gauge-invariance principle introduced in Chapter 3, that gives a rigorous way of deriving an expression for the energy flux directly from DFT, without introducing any *ad hoc* ingredients. We describe this approach in Section 4.2 and we will use it in the last part of this work.

More recently, several authors attempted to combine the GK approach to heat transport with first-principles techniques based on electronic-structure theory, by adopting some *ad hoc* definitions for the energy flux. Kang and Wang [92], for instance, derived an expression for the energy flux from a (rather arbitrary) quantum-mechanical definition of the atomic energies and used a modified MD integration algorithm to cope with the difficulties ensuing from the implementation of their expression in PBC. Carbogno et al. [42] gave a different expression for the energy flux, that neglects the convective term, Eq. (2.38), and is based on a normal-mode decomposition of the atomic coordinates and forces, which, while reducing the effects of thermal fluctuations, can only be applied to crystalline solids. English and Tse [93], instead, used the classical Einstein relation for the energy displacement, $\mathcal{D}(\tau) = \sum_n \mathbf{R}_n \int_0^\tau \mathbf{F}_n \cdot \mathbf{V}_n \, dt$, computed from a BO-AIMD trajectory, where the forces are computed via the Hellmann-Feynman theorem. They applied this methodology to the computation of thermal conductivity of periclase MgO [94] and other solids. Their approach also neglects the convective term and is only applicable to solids.

4.2   DFT energy flux

The gauge invariance principle presented in Chapter 3 provides a rigorous way to derive an expression for the adiabatic energy flux from DFT. In order to derive such an expression, we start with the standard DFT expression of the total energy in terms of the Kohn-Sham (KS) eigenvalues ε_v, eigenfunctions $\phi_v(\mathbf{r})$, and density $n(\mathbf{r}) = \sum_v |\phi_v(\mathbf{r})|^2$ [27]:[1]

$$E_{DFT} = \frac{1}{2} \sum_n M_n V_n^2 + \frac{\mathsf{e}^2}{2} \sum_{n,m \neq n} \frac{Z_n Z_m}{|\mathbf{R}_n - \mathbf{R}_m|}$$
$$+ \sum_v \varepsilon_v - \frac{\mathsf{e}^2}{2} \int \frac{n(\mathbf{r})n(\mathbf{r}')}{|\mathbf{r} - \mathbf{r}'|} d\mathbf{r} d\mathbf{r}' + \int \left(\epsilon_{xc}[n](\mathbf{r}) - \mu_{xc}[n](\mathbf{r}) \right) n(\mathbf{r}) d\mathbf{r}, \quad (4.1)$$

where $\{\mathbf{R}\}$ and $\{\mathbf{r}\}$ indicate ionic and electronic positions, respectively, e is the electron charge, $\epsilon_{xc}[n](\mathbf{r})$ is a local exchange-correlation (XC) energy per particle defined by the relation $\int \epsilon_{xc}[n](\mathbf{r})n(\mathbf{r})d\mathbf{r} = E_{xc}[n]$, the latter being the total XC energy of the system, and $\mu_{xc}(\mathbf{r}) = \frac{\delta E_{xc}}{\delta n(\mathbf{r})}$ is the XC potential. The DFT total

---

[1]For simplicity, here and in the following we imply the dependence on time t of atomic positions, velocities and KS orbitals.

energy can be readily written as the integral of a DFT energy density (not uniquely defined) [61]:

$$E_{DFT} = \int e_{DFT}(\mathbf{r}) d\mathbf{r},$$

$$e_{DFT}(\mathbf{r}) = e_{el}(\mathbf{r}) + e_z(\mathbf{r}), \tag{4.2}$$

where:

$$e_{el}(\mathbf{r}) = \Re \mathfrak{e} \sum_v \phi_v^*(\mathbf{r})\big(H_{KS}\phi_n(\mathbf{r})\big)$$

$$- \frac{1}{2} n(\mathbf{r}) v_H(\mathbf{r}) + (\epsilon_{XC}(\mathbf{r}) - \mu_{XC}(\mathbf{r})) \, n(\mathbf{r}), \tag{4.3}$$

$$e_z(\mathbf{r}) = \sum_n \delta(\mathbf{r} - \mathbf{R}_n)\left(\frac{1}{2}M_n V_n^2 + w_n\right), \tag{4.4}$$

$$w_n = \frac{\mathrm{e}^2}{2}\sum_{m\neq n}\frac{Z_n Z_m}{|\mathbf{R}_n - \mathbf{R}_m|}, \tag{4.5}$$

H_{KS} is the instantaneous self-consistent Kohn-Sham Hamiltonian, and $v_H = \mathrm{e}^2 \int d\mathbf{r}' \frac{n(\mathbf{r}')}{|\mathbf{r}-\mathbf{r}'|}$ is the Hartree potential.

An explicit expression for the DFT energy flux is obtained by computing the first moment of the time derivative of the energy density, Eqs. (4.2-4.5), as indicated in Eq. (2.32),

$$\mathbf{J}^E = \frac{1}{\Omega}\int \dot{e}_{DFT}(\mathbf{r})\,\mathbf{r}\,d\mathbf{r}, \tag{4.6}$$

and considering the Born-Oppenheimer (BO) equations of motion for the nuclei:

$$M_n \dot{\mathbf{V}}_n = -\frac{\partial E_{DFT}}{\partial \mathbf{R}_n}. \tag{4.7}$$

This results in a number of terms, some of which are either infinite or ill-defined in PBC. Casting the result in a regular, boundary-insensitive, expression requires a careful breakup and refactoring of the various harmful terms [31, 55]. The final

result reads:

$$\mathbf{J}_{DFT}^{E} = \mathbf{J}^{H} + \mathbf{J}^{z} + \mathbf{J}^{0} + \mathbf{J}^{KS} + \mathbf{J}^{XC}, \tag{4.8}$$

$$\mathbf{J}^{H} = \frac{1}{4\pi\Omega e^{2}} \int \nabla v_{H}(\mathbf{r})\dot{v}_{H}(\mathbf{r})d\mathbf{r}, \tag{4.9}$$

$$\mathbf{J}^{z} = \frac{1}{\Omega}\sum_{n}\left[\mathbf{V}_{n}\left(\frac{1}{2}M_{n}V_{n}^{2} + w_{n}\right) + \sum_{m\neq n}(\mathbf{R}_{n} - \mathbf{R}_{m})\left(\mathbf{V}_{m}\cdot\frac{\partial w_{n}}{\partial\mathbf{R}_{m}}\right)\right], \tag{4.10}$$

$$\mathbf{J}^{0} = \frac{1}{\Omega}\sum_{n}\sum_{v}\left\langle\phi_{v}\left|(\mathbf{r} - \mathbf{R}_{n})\left(\mathbf{V}_{n}\cdot\frac{\partial\hat{v}_{0}}{\partial\mathbf{R}_{n}}\right)\right|\phi_{v}\right\rangle, \tag{4.11}$$

$$\mathbf{J}^{KS} = \frac{1}{\Omega}\sum_{v}\left(\langle\phi_{v}|\mathbf{r}H_{KS}|\dot{\phi}_{v}\rangle + \varepsilon_{v}\langle\phi_{v}|\mathbf{r}|\dot{\phi}_{v}\rangle\right) = \frac{1}{\Omega}\mathfrak{Re}\sum_{v}\left\langle\bar{\phi}_{v}^{c}\left|H_{KS} + \varepsilon_{v}\right|\dot{\phi}_{v}^{c}\right\rangle, \tag{4.12}$$

$$J_{\alpha}^{XC} = \begin{cases} 0 & \text{(LDA)} \\ -\frac{1}{\Omega}\int n(\mathbf{r})\dot{n}(\mathbf{r})\frac{\partial\epsilon^{GGA}(\mathbf{r})}{\partial(\partial_{\alpha}n)}d\mathbf{r} & \text{(GGA)}, \end{cases} \tag{4.13}$$

where $\hat{v}_{0}$ is the bare, possibly non-local, (pseudo-) potential acting on the electrons and

$$|\bar{\phi}_{v}^{c}\rangle = \hat{P}_{c}\,\mathbf{r}\,|\phi_{v}\rangle, \tag{4.14}$$

$$|\dot{\phi}_{v}^{c}\rangle = \hat{P}_{c}|\dot{\phi}_{v}\rangle = \dot{\hat{P}}_{v}|\phi_{v}\rangle, \tag{4.15}$$

are the projections over the empty-state manifold of the action of the position operator over the v-th occupied orbital, Eq. (4.14), and of its adiabatic time derivative [95], Eq. (4.15); $\hat{P}_{v}$ and $\hat{P}_{c} = 1 - \hat{P}_{v}$ being the projector operators over the occupied- and empty-states manifolds, respectively. Both these functions are well defined in PBC and can be computed, explicitly or implicitly, using standard density-functional perturbation theory [68].

4.2.1 Electronic current

The current $\mathbf{J}^{KS}$, Eq.(4.12), is not manifestly invariant with respect to the arbitrary choice of the zero of the one-electron energy levels: a shift of this zero by a quantity $\Delta\epsilon$ results in a shift of the energy flux by $\Delta\mathbf{J}^{el}$, where $\mathbf{J}^{el}$ is the adiabatic electronic current [96]:

$$\mathbf{J}^{el} = \frac{2}{\Omega}\mathfrak{Re}\sum_{v}\langle\bar{\phi}_{v}^{c}|\dot{\phi}_{v}^{c}\rangle, \tag{4.16}$$

that can be derived from the continuity equation for the electronic density:

$$\nabla\cdot\boldsymbol{j}^{el}(\boldsymbol{r},t) = -\dot{n}^{el}(\boldsymbol{r},t). \tag{4.17}$$

The electronic current is the difference between the total charge current (defined as the atom's Born charge times its velocity and summed over the atoms) and its ionic component (here defined considering the nucleus plus the valence electrons). In

the specific case of one-component systems and molecular systems that are electric insulators, the total charge current and the electronic flux $\mathbf{J}^{el}$ are non-diffusive, as well as the ionic one, *i.e.* they do not contribute to thermal conductivity, lifting the apparent indeterminacy of Eq. (4.12). In multi-component systems this is not the case. Starting from Eq. (2.48), it can be proved that a shift in the zero-energy level adds a possibly diffusive contribution to the energy current, which however does not affect the thermal conductivity.

4.2.2   Numerical computation

The computation of the DFT energy flux, Eq. (4.8), at time t requires the atomic positions $\{\mathbf{R}\}$ and velocities $\{\mathbf{V}\}$, along with the Kohn-Sham eigenvalues ε_v, eigenfunctions $\phi_v(\mathbf{r})$, the ground-state electron density distributions $n(\mathbf{r}) = \sum_v |\phi_v(\mathbf{r})|^2$, and their time-derivatives.

   The method is implemented within the QUANTUM ESPRESSO code suite [95, 97] in a specialized post-processing code maintained by us. In order to compute the energy flux $\mathbf{J}^E$, the following steps are needed:

1. One should extract a sufficient number of time steps from a AIMD trajectory (the sampling frequency should be high enough to avoid aliasing problems: a deeper discussion on this is reported in Sec. 6.3).

2. For each of these time steps, two self-consistent Kohn-Sham self-consistent field calculations are performed with the PWSCF code: one at time t and one at time $t + \Delta t$. The atomic coordinates at time $t + \Delta t$ can be extrapolated from those at time t, simply as $\mathbf{R}(t + \Delta t) = \mathbf{R}(t) + \mathbf{V}(t)\Delta t$. The value of the finite difference Δt is very important, and is much smaller than the time step used to evolve the dynamics with MD. A convergence check should be performed beforehand.

3. The resulting densities are used to compute the time derivative of the electron density at time t, $\dot{n}(t)$, with finite differences: $\dot{n}(t) = (n(t + \Delta t) - n(t))/\Delta t$.

The cost of one energy flux calculation is about equal to the cost of two self-consistent PW calculations plus one linear response calculation. For example, in the current implementation, each time step costs almost 4 times the cost of a self-consistent calculation.

4.3   Outlook

As it was already mentioned in Sec. 3.4, the gauge invariance of transport coefficients not only provides a solid foundation to the quantum theory of adiabatic heat transport, by also allows tuning this definition so as to achieve optimal statistical properties to reduce its computational cost. This freedom can in principle be

exploited to design new expressions for the heat flux from first principles. One possibility may be devising a formulation based on a local representation of the electronic structure [98, 99], *e.g.* maximally localized Wannier functions, that would avoid the use of density-functional perturbation theory for the computation of $\mathbf{J}^{KS}$, by removing the ill-definition problems in PBC. In the case of solids, where correlation times are generally longer, a more efficient expression may be obtained from a normal-mode expansion [46] and interpolation, to cope with noise and finite-size effects, in a similar way to what proposed by Carbogno et al. [42].

Furthermore, the expression of the energy flux, that is now implemented for LDA and GGA energy functionals, can be extended to more advanced functionals [100, 101], where dispersion forces are accounted for. This effects are important in the structural and transport properties of many soft materials, and may give important contributions to the thermal conductivity as well.

Finally, the *ab initio* computation of thermal conductivity of multi-component fluids has never been attempted and would be particularly beneficial to study systems in extreme conditions.

5

Estimation of heat transport coefficients

CONTENTS

The evaluation of transport coefficients in extended systems, such as thermal conductivity or shear viscosity, is known to require impractically long simulations. The Green-Kubo equation, Eq. (2.30), expresses the thermal conductivity as the integral of the autocorrelation function of the heat flux, *i.e.* an autocorrelation time.

Many methods have been formulated to estimate its value from finite-length MD simulations: direct time-integration methods, fitting with exponential functions, and spectral methods; however, few of them provide a rigorous criterion to estimate the accuracy resulting from a given MD trajectory. Different classes of systems require different approaches to error analysis, but it is widely believed that they always require so long simulation times as to be unaffordable with accurate but expensive AIMD techniques [42].

The recent advances in the quantum simulations of thermal transport reinvigorated the interest in this subject and made it urgent to devise a data-analysis technique to make these calculations affordable, thus paving the way to the *ab initio* simulation of heat transport. In order to solve this problem, we considered it in

the light of the statistical theory of stationary time series, and we devised a data-analysis protocol leading to an asymptotically unbiased and consistent estimate of transport coefficients (*i.e.* the bias and the statistical error can be made both arbitrarily small in the limit of long simulation times) and requiring shorter simulations than used so far [B]. This protocol, based on the *cepstral analysis* of time series, avoids any *ad-hoc* fitting procedure and naturally provides an accurate estimate of the statistical error, thus lending itself to an easy implementation and automated use. While motivated by heat transport applications, our approach naturally applies to *any* other transport properties that can be expressed, in a GK framework, in terms of time integrals of suitable autocorrelation functions, such as, *e.g.*, ionic conductivities, viscosities, and tracer diffusivity, to name but a few.

In Section 5.1 of this chapter we review some of the techniques found in the literature to estimate the Green-Kubo integral and we illustrate some of their criticalities, along with some physical interpretations that have been proposed. In Section 5.2, we reformulate the problem in the light of the statistical theory of time series and show how to obtain an estimator of the thermal conductivity from cepstral analysis in solids and one-component fluids. We validate this method with extensive benchmarks on the calculation of the thermal conductivity of different classes of materials. In Section 5.3 we show how to extend the theory to the case of multi-component fluids. In Section 5.4 we introduce a couple of techniques useful to optimise the statistical properties of the heat currents by making use of the gauge invariance principle, a procedure that we found particularly useful when dealing with *ab initio* heat currents. Section 5.5 closes this chapter with an outlook of possible future prospects.

5.1 Estimation and interpretation of the Green-Kubo integral

In the following we shall focus on one-component systems, or molecular systems, where the heat flux corresponds to the energy flux. In order to estimate the thermal conductivity from EMD with the GK approach, one starts by computing the energy current $\mathbf{J}$ from a MD trajectory in the microcanonical ensemble,[1] via the classical expression, Eq. (2.36) (Eq. (2.37) for 2-body force fields), or the quantum (DFT) one, Eq. (4.8).

Thanks to ergodicity, an ensemble average is equivalent to a time average [82], that is an average over different starting times of a single trajectory. The heat current autocorrelation function (HCACF), $\langle J(t)J(0)\rangle$, can thus be estimated as a

---

[1]The issue of estimating dynamical properties in the canonical ensemble with thermostats is still matter of debate and is not completely settled. Some preliminary tests on simple systems showed that thermal conductivity is not affected by a well-designed global thermostat. However, we believe that this issue should be a matter of further dedicated studies, that fall outside the scope of this work. Therefore we decide to employ the common practice of computing dynamical properties in the microcanonical ensemble.

running average of time-lagged current products:

$$\langle J^i(t)J^j(0)\rangle \sim \frac{1}{\mathcal{T}-t}\int_0^{\mathcal{T}-t} J^i(\tau+t)J^j(\tau)\,d\tau, \qquad (5.1)$$

where $\mathcal{T}$ is the length of the MD trajectory, and J^i indicates any Cartesian component of $\mathbf{J}_i$. However, the calculation of dynamical properties, such as thermal conductivity, requires a minimum trajectory to compute time-correlation functions. On the computational point of view, it was shown that ensemble averaging, *i.e.* averaging over different initial configurations, exhibits similar overall cost with respect to simple time averaging, but it may significantly accelerate the calculation by exploiting parallel machines [102]. This point can be particularly relevant when dealing with expensive AIMD simulations.

5.1.1 Example: four paradigmatic systems

To illustrate some concepts in this Section, we provide a few examples. We have run classical MD simulations [56] of four paradigmatic systems representative of different classes of materials, using the LAMMPS package and the following setup:

- **liquid Ar**: Lennard-Jones potential as described in Ref. [103], at a temperature $T \approx 220\,\mathrm{K}$ and density $\rho = 1.55\,\mathrm{g/cm^3}$, in a cubic supercell containing 864 atoms, with a time step $\Delta t = 4\,\mathrm{fs}$.

- **liquid H_2O**: Flexible model as in Ref. [104] at a temperature $T \approx 300\,\mathrm{K}$ and density $\rho = 1.0\,\mathrm{g/cm^3}$, in a cubic supercell containing 180 molecules, with a time step $\Delta t = 0.5\,\mathrm{fs}$.

- **crystalline fcc MgO**: Buckingham-plus-Coulomb potential as in Ref. [105] at a temperature $T \approx 1000\,\mathrm{K}$ and density $\rho = 3.61\,\mathrm{g/cm^3}$, in a $4 \times 4 \times 4$ simple cubic conventional supercell with 512 atoms, and a time step $\Delta t = 0.3\,\mathrm{fs}$

- **amorphous SiO_2**: BKS potential [106] as implemented by Mantisi et al. [107] (see Sec. 6.2.1) at a temperature $T \approx 1000\,\mathrm{K}$ and density $\rho = 2.29\,\mathrm{g/cm^3}$, in a supercell containing 216 atoms with a time step $\Delta t = 1\,\mathrm{fs}$. The glass model was obtained from a quench from the melt ($T \approx 6500\,\mathrm{K}$) at a constant quenching rate of $5.5 \times 10^{12}\,\mathrm{K/s}$.

Each system was equilibrated in the NVT ensemble at the target temperature for several hundred picoseconds; data were then collected in the NVE ensemble and analysed. We will also use these systems to benchmark the cepstral analysis method presented in Sec. 5.2.

The HCACFs computed for these materials are shown in Fig. 5.1(a). Liquid argon's HCACF is characterised by a simple exponential decay, characteristic of a simple diffusing liquid. The HCACFs of the other systems, instead, are characterised by an initial drop, followed by a much longer tail, with fast superimposed oscillations caused by the fast intramolecular vibrations (they can thought to be linked to the optical phonon modes of the system). MgO, being a crystalline solid, exhibits the
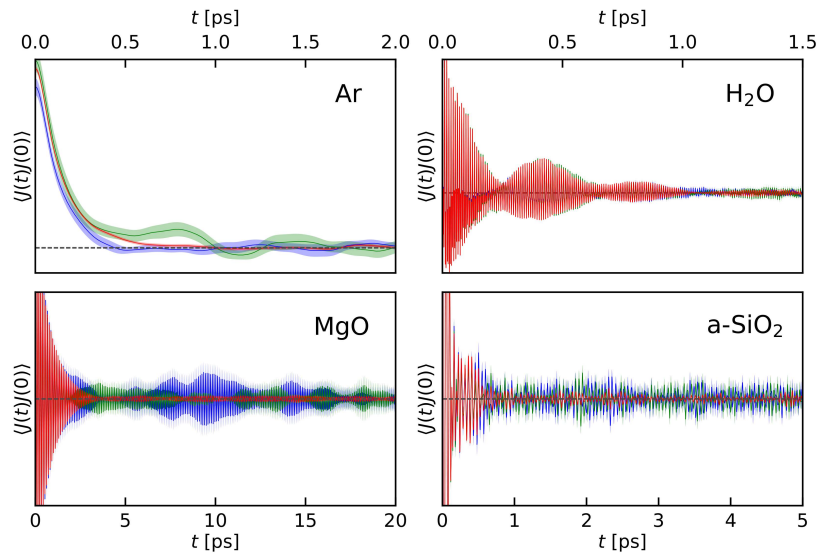
(a)
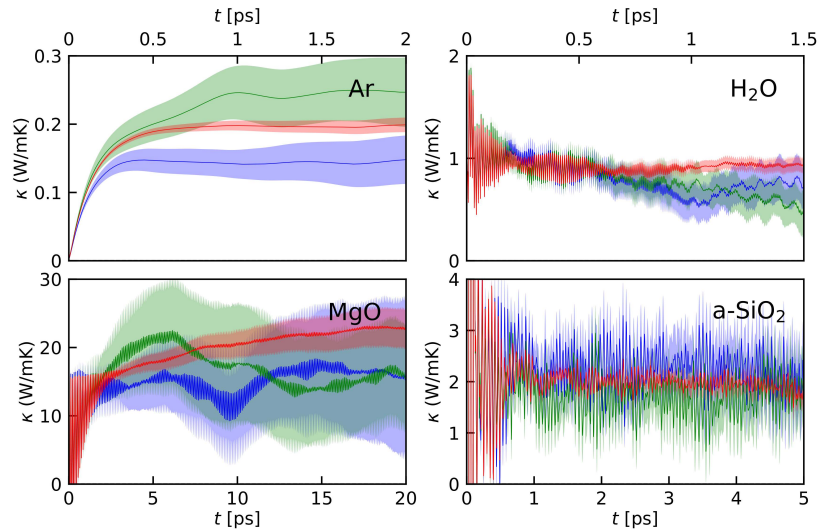
(b)

Figure 5.1: (a) Time correlation function of the energy current, Eq. (5.1), and (b) the thermal conductivity as a function of the upper limit of integration, Eqs. (5.2-5.3), computed from MD trajectories for Ar, H_2O, MgO, and a-SiO_2, The blue and green lines are computed from two different 100 ps trajectories; the red line is computed from a 1 ns trajectory. The shaded area surrounding each line indicates the error bars, as estimated from standard block analysis.

longest correlations, due to the long lifetimes of its propagating phonons. Water and silica, instead, have similar HCACFs, that decay quite fast but feature high-frequency oscillations that persist at long time-lags.

When a HCACF is computed from a trajectory of finite length $\mathcal{T}$, the statis-

tical error increases with the time-lag t, as larger time-lags have less statistics. In Fig. 5.1(a) three examples of HCACFs are plotted: two of them are computed from a 100 ps trajectory and present more oscillations and a larger statistical error with respect to the the third HCACF, that is computed from a 1 ns trajectory and shows a smoother decay.

5.1.2 Direct integration

The evaluation of the GK integral, Eq. (2.1), or more generally of an Onsager coefficient L^{ij}, Eq. (2.19), can simply be performed by direct integration of Eq. (5.1) as a function of the upper limit of integration:

$$L^{ij}(\texttt{T}) = \frac{\Omega}{k_B} \int_0^\texttt{T} \langle J^i(t) J^j(0) \rangle \, dt,$$ (5.2)

with $\texttt{T} < \mathcal{T}$. One then recovers, via Eq. (2.48), an estimate for the thermal conductivity dependent on $\texttt{T}$:

$$\kappa(\texttt{T}) = \frac{1}{T^2} \frac{1}{(L^{-1}(\texttt{T}))^{11}}.$$ (5.3)

This function is usually very noisy: in fact, at times greater than the correlation time between J^i and J^j, the correlation function $\langle J^i(t) J^j(0) \rangle$ approaches zero, hence $L^{ij}(\texttt{T})$ starts integrating pure noise and behaves like the distance travelled by a random walk, whose variance grows linearly with the upper integration limit, as can be appreciated in Fig. 5.1(b). The evaluation of transport coefficients thus requires averaging over multiple trajectories (possibly multiple segments of a same long trajectory) and estimating the resulting uncertainty as a function of both the length of each trajectory and the upper limit of integration, usually with standard *block analysis* [82]. This is a cumbersome task that often leads to a poor estimate of the statistical and systematic errors on the computed conductivity. All the more so when the signal is inherently oscillatory, due to the existence of high-frequency features, possibly due to intramolecular oscillations that meddle with the noise and can make the convergence of the GK not obvious.

The accuracy of the transport coefficient κ estimated by a direct integration of Eq. (5.2) is subject to three possible sources of errors:

- *averaging error*: the finite simulation length $\mathcal{T}$ over which the HCACF is computed, Eq. (5.1).

- *truncation error*: the upper limit of integration $\texttt{T}$ used in the estimation of L^{ij}, Eq. (5.2), that should be much larger than the characteristic decay time of the correlation, but much smaller thatn the simulation length $\mathcal{T}$.

- *discretization/aliasing error*: the finite sampling interval of the heat current, ϵ, that should be large enough to avoid aliasing effects. The Nyqvist-Shannon sampling theorem [108] states that the sampling period should be smaller than $\frac{1}{2 f_{\max}}$, where $f_{\max}$ is the maximum frequency of the heat flux signal $J(t)$.
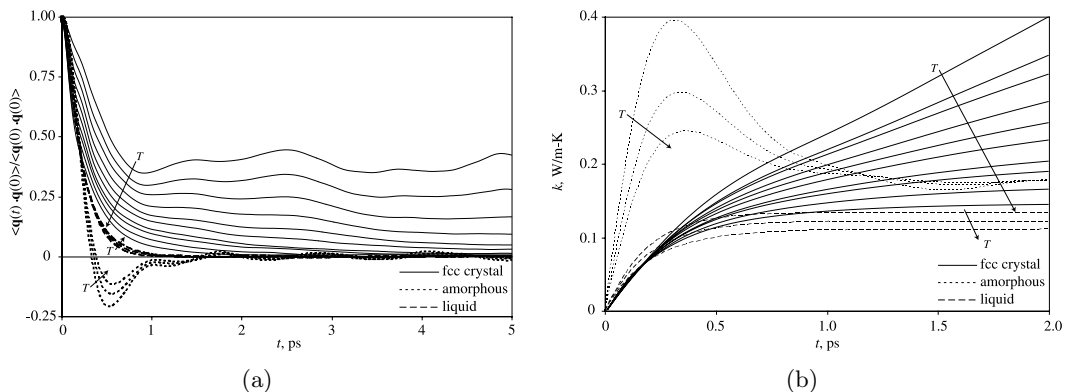
Figure 5.2: (a) Heat current autocorrelation function, Eq. (5.1), and (b) thermal conductivity as a function of the upper integration limit, Eqs. (5.2-5.3), for three phases of LJ argon. Reproduced from Ref. [109].

McGaughey and Kaviany [40, 109] studied the thermal conductivity of LJ argon in different phases: fcc crystal, liquid, and amorphous. In Fig. 5.2 we report the comparisons of the HCACFs of these three phases and their direct GK integrals, Eq. (5.3). At finite time the HCACFs of solid Ar show the two-stage decay [46], and their extension decreases as the temperature increases, as one would expect due to the decrease of phonons relaxation times. Their integral converges to the corresponding value of thermal conductivity, however the practical determination of κ may be quite subjective. Actually, in the majority of the GK studies reported in the literature, the criteria used to choose an upper limit of integration is not specified, so we guess that they are often based on simple assumption of convergence "by sight". A few exceptions are listed in the following. For example, the "first dip" (FD) method, proposed by Li et al. [110], specifies the upper limit of integration by setting the upper limit of integration to be the first time at which the calculated HCACF goes negative. FD may give acceptable results in solid and liquid argon, but it is not suitable to the amorphous phase and in systems with multi-atom unit cell, where the HCACF oscillates wildly around zero before slowly fading out.

In the case of unit cells with multiple atoms, where intramolecular vibrations manifest as fast oscillations in the HCACF, again, the EF method is not suited to determine κ. A rather arbitrary compromise was used by McGaughey and Kaviany [111]: the GK integral function, Eq. (5.2), is filtered with a running average [112] and the value at which it looks to converge is chosen. If the convergence is not clear one chooses to stop the integration at the point at which the oscillations of $L^{ij}(\mathtt{T})$ reach a minimum (neck).

Other methods to to perform error analysis have been devised, based on either heuristic or rigorous arguments [58, 113–116]. All require an estimate of an optimal value for the upper limit of integration, which determines a bias in the estimate, and which is in general difficult to obtain. Moreover most of them are specifically conceived and tested on simple crystalline solids, such as silicon, and are not suited

to study disordered and complex systems. For example, Jones and Mandadapu [114] proposed a heuristic on-the-fly algorithm to detect the convergence of the block average of κ, but that needs an empirical estimate of the maximum correlation time first, and thus it is not optimal. A similar empirical criterion has also been proposed by Wang et al. [115]. Oliveira and Greaney [116], instead, proposed a method that analyses the components of the noise of the GK integral and fits them with integral functions, in order to obtain an estimate of the uncertainty on κ of graphite.

5.1.3 Exponential fit and thermal conductivity decomposition

Another technique proposed by some authors is the exponential fit (EF) method, in which a single or multi-exponential function is fitted to the HCACF beyond a certain point (determined on a case-by-case basis) [110, 117, 118]. An example is the function [117]:

$$\langle J(t)J(0)\rangle = A_{\mathrm{ac,sh}}\mathrm{e}^{-t/\tau_{\mathrm{ac,sh}}} + A_{\mathrm{ac,lg}}\mathrm{e}^{-t/\tau_{\mathrm{ac,lg}}}, \qquad (5.4)$$

where the subscripts "ac, sh" and "lg" refer to acoustic, short-, and long range. From here the thermal conductivity is then estimated as:

$$\kappa = \frac{\Omega}{k_B T^2}(A_{\mathrm{ac,sh}}\tau_{\mathrm{ac,sh}} + A_{\mathrm{ac,lg}}\tau_{\mathrm{ac,lg}}) = \kappa_{\mathrm{ac,sh}} + \kappa_{\mathrm{ac,lg}}. \qquad (5.5)$$

McGaughey and Kaviany [109] interpreted the two-stage behaviour of solid argon's HCACF and the resulting decomposition of the thermal conductivity in the context of the mean phonon relaxation time: $\kappa_{\mathrm{ac,sh}}$ corresponds to the phonons with lowest relaxation times,[2] whereas $\kappa_{\mathrm{ac,lg}}$ corresponds to phonons with longer relaxation times, that make the longer decay time of the HCACF. This model works fairly well *e.g.* for solid argon [109], diamond and carbon nanotubes [117, 121], as well as in liquid argon, where a single-exponential decay is found, but does not work well to fit the long tails of the HCACF of silicon [57].

The HCACF of amorphous argon, though, shows a different behaviour with respect to the solid an liquid phases. It is very similar to the velocity autocorrelation function and can be interpreted considering the different local environments the atoms experience. In a crystal each atom is immersed in the same local environment and the same is true in a liquid, if we average over time. Conversely, in an amorphous solid each atom has a different local environment: close to its equilibrium position, it experiences the free trajectory of a liquid atom at short time scales; but at slightly larger times it feels the interactions of the other atoms, that change its trajectory, and make the correlation negative. The first timescale of the HCACF decomposition, $\tau_{\mathrm{ac,sh}}$, is related to the time it takes for the energy to move between nearest-neighbour atoms, and corresponds to the higher frequencies of the acoustic branches. The $\kappa_{\mathrm{ac,sh}}$ is the only one important in the liquid and amorphous phase, it

---

[2]*i.e.* phonons with a mean free path equal to one half of its wavelength, the shortest possible. This is also called the CP limit, a thermal conductivity model developed for amorphous materials [119, 120].

is a function of the coordination of the atoms and scarcely depends on temperature, whereas $\kappa_{\mathrm{ac,lg}}$ strongly depends on temperature.

When fast oscillations of the HCACF are present, such as in multi-atom unit cells, McGaughey and Kaviany [111] attempted to fit the filtered HCACF with Eq. (5.5) plus a sum of oscillating terms, that they associated to the "optical" modes of the system. Nevertheless, this fitting procedure is very difficult and it was found to be unsuitable for amorphous materials like silica glass, that therefore require either a direct integration or an alternative approach.

5.1.4 Spectral methods

As was shown in Sec. 2.2.1, the Wiener-Khintchine theorem enables one to express the heat conductivity in terms of the zero-frequency value of the power spectrum of the energy-flux (see Eqs. (2.22-2.25)):

$$\kappa = \frac{\Omega}{2k_B T^2} S(\omega = 0). \tag{5.6}$$

Estimating this limit can be very difficult if the statistical properties of the power spectrum are not taken properly into account, as we will argument in Sec. 5.2.

Some attempts were made by fitting the low-frequency region of the spectrum with one Lorentzian function. This is the Fourier transform of an exponential correlation function, hence, not surprisingly, this expression is in good agreement with time integration results when the HCACF is well modeled by one exponential, but does not work when a long tail is present in the HCACF and whenever the exponential fit is inappropriate [57]. The same applies if we consider the sum of two Lorentzians, *i.e.* the sum of two exponential functions in the time domain [122].

Lee et al. [123] and Volz and Chen [124] applied these fits in amorphous and crystalline silicon, respectively, speculating that finite-size effects would affect the low-frequency region. The finite size of the simulation cell sets a lower limit to the phonon wavelength that is allowed: only phonons with a wavelength shorter than the cell size are permitted to exist in the simulation domain and can contribute to the thermal conductivity. Furthermore, the small cell size may introduce artificial autocorrelations that do not exist in real systems, an effect that could be especially strong for phonons with long mean-free paths.

We believe that it is not easy to determine *a priori* at what level the power spectrum is affected by finite-size effects. Besides, let us notice that the size-dependence problem in the estimation of κ is also present in other methods, such as the direct integration of the GK equation. In general, one should be careful to verify that the chosen simulation cell is big enough for the thermal conductivity to converge. This will also imply that the low-frequency region of the power spectrum is correctly reproduced and does not exhibit unphysical features. We shall go back on this issue in Sec. 6.1.2 and 6.2.2.

5.1.5 Final remarks

Many methods have been formulated to estimate the thermal conductivity from the GK equation, but none of them is fully satisfactory. Some of them are optimized to the specific case of crystalline solids or simple liquids, and may be a good choice, however they do not really help much when dealing with amorphous solids. Different classes of systems require different approaches to error analysis: in some cases these methods fail to provide rigorous criteria to estimate the accuracy resulting from a given MD trajectory, but in general all of them always require very long simulation times, thus making *ab initio* simulations unaffordable. In next section we are going to present a novel data-analysis method that will be able to tackle both these problems and to provide us with an efficient and accurate estimator of κ. This will finally enable us to undertake the study of thermal conductivity of glasses with equilibrium AIMD simulations.

In Sec. 5.1.3 we saw that one may try to interpret the decay of HCACF in terms of different relaxation times to get insights into the different contributions to the thermal conductivity, though this is not obvious and clear in general. The GK equation is a very general result describing the collective dissipative response of any system to a fluctuation, and it has no intrinsic connection to particular transport mechanisms [58]. The frequencies of the power spectrum of the HCACF have been interpreted to be related to the phonon-phonon interactions [109]. Conversely, in the BTE approach the thermal conductivity is computed by integrating over the frequencies of individual phonons. The difference between these two frequencies is equivalent to that between the mean free path and the corresponding phonon wavelength.

However, in the light of the gauge invariance principle presented in Ch. 3, at this stage it is not very clear how much the HCACF or the power spectrum of the heat current can be interpreted in physical terms. It is evident that different definitions of the microscopic energy density (or atomic energies) will define different energy currents with very different power spectra, the only invariant quantity being their zero-frequency value, *i.e.* the thermal conductivity. Whether and how a particular definition can be linked to physical quantities is not yet completely understood. Therefore, extreme caution should be used when making physical interpretations out of a HCACF.

In conclusion, although the GK method yields a direct estimate of the thermal conductivity, it provides only very indirect information about the mechanisms of heat transport. We believe that different approaches, such as phonon-level methods, *e.g.* methods based on a normal-modes analysis [125], may be able to bring better insights into the individual contributions to thermal conductivity, especially in complex or disordered systems.

5.2   Cepstral analysis

In practice, MD gives access to a discrete sample of the flux process (a *time series*), $J_n = J(n\epsilon)$, $0 \le n \le N - 1$, where ϵ is the sampling period of the flux and N the length of the time series, that we assume to be even.

5.2.1   Periodogram

Let us define the discrete Fourier transform of the flux time series as:

$$\tilde{J}_k = \sum_{n=0}^{N-1} \mathrm{e}^{2\pi i \frac{kn}{N}} J_n, \tag{5.7}$$

for $0 \le k \le N - 1$.[3] The *sample spectrum* $\hat{S}_k$, aka *periodogram* in the statistics literature, is defined as

$$\hat{S}_k = \frac{\epsilon}{N} \left| \tilde{J}_k \right|^2, \tag{5.8}$$

and, for large N, it is an unbiased estimator of the power spectrum of the process, as defined in Eq. (2.22), evaluated at $\omega_k = 2\pi \frac{k}{N\epsilon}$, namely: $\langle \hat{S}_k \rangle = S(\omega_k)$. The reality of the $\hat{J}$'s implies that $\tilde{J}_k = \tilde{J}_{N-k}^*$ and $\hat{S}_k = \hat{S}_{N-k}$, so that periodograms are usually reported for $0 \le k \le \frac{N}{2}$ and their Fourier transforms evaluated as discrete cosine transforms.

The space autocorrelations of conserved currents are usually short-ranged. Therefore, in the thermodynamic limit the corresponding fluxes can be seen as sums of (almost) independent identically distributed stochastic variables, so that, according to the central-limit theorem, their equilibrium distribution is Gaussian. A slight generalisation of this argument leads us to conclude that any conserved-flux process, like the heat flux, is Gaussian as well. The flux time series is in fact a multivariate stochastic variable that, in the thermodynamic limit, results from the sum of (almost) independent variables, thus tending to a multivariate normal deviate. This implies that at equilibrium the real and imaginary parts of the $\tilde{J}_k$'s defined in Eqs. (5.7) are zero-mean normal deviates that, in the large-N limit, are uncorrelated among themselves and have variances proportional to the power spectrum evaluated at ω_k. For $k = 0$ or $k = \frac{N}{2}$, $\tilde{J}_k$ is real and $\sim \mathcal{N}\left(0, \frac{N}{\epsilon} S(\omega_k)\right)$; for $k \notin \left\{0, \frac{N}{2}\right\}$, $\mathfrak{Re}\tilde{J}_k$ and $\mathfrak{Im}\tilde{J}_k$ are independent and both $\sim \mathcal{N}\left(0, \frac{N}{2\epsilon} S(\omega_k)\right)$, where $\mathcal{N}(\mu, \sigma^2)$ indicates a normal deviate with mean μ and variance σ^2. We conclude that in the large-N limit the sample spectrum of the heat-flux time series reads:

$$\hat{S}_k = S(\omega_k)\, \xi_k \,, \tag{5.9}$$

where the ξ's are independent random variables distributed as a χ_1^2 variate for

---

[3]Here, the convention for the sign in the exponential of the time-to-frequency Fourier transform is opposite to what adopted in Ref. [B] and in most of the signal analysis literature, in order to comply with the convention for the space-time Fourier transforms usually adopted in the Physics literature and in Eqs. (2.4) and (2.5).

$k = 0$ or $k = \frac{N}{2}$ and as one half a χ_2^2 variate, otherwise. Here and in the following χ_ν^2 indicates the chi-square distribution with ν degrees of freedom. For the sake of simplicity, we make as though all the ξ's were identically distributed as $\xi_k \sim \frac{1}{2}\chi_2^2$ for all values of k, thus making an error of order $\mathcal{O}(1/N)$, which vanishes in the long-time limit that is being assumed throughout this section.

Multiple samples

In many cases of practical interest, multiple time series are available to estimate the power spectrum of a same process, $\{{}^p J_n\}$, $p = 1, \cdots \ell$. For instance, in equilibrium MD a same trajectory delivers one independent time series per Cartesian component of the heat flux, all of which are obviously equivalent in isotropic systems. In these cases it is expedient to define a mean sample spectrum by averaging over the ℓ different realisations,

$$
{}^\ell \hat{S}_k = \frac{\epsilon}{\ell N} \sum_{p=1}^{\ell} \left| {}^p \tilde{J}_k \right|^2
$$

$$
= S(\omega_k) {}^\ell \xi_k ,
$$

(5.10)

where the ${}^\ell \xi$'s are $\chi_{2\ell}^2$ variates, divided by the number of degrees of freedom:

$$
{}^\ell \xi_k \sim \frac{1}{2\ell} \chi_{2\ell}^2,
$$

(5.11)

for $k \notin \{0, \frac{N}{2}\}$.

Eqs. (5.9) and (5.10) show that ${}^\ell \hat{S}_0$ is an unbiased estimator of the zero-frequency value of the power spectrum, $\langle {}^\ell \hat{S}_0 \rangle = S(0)$, and through Eq. (5.6), of the transport coefficients we are after. However, this estimator is not consistent, *i.e.* its variance does not vanish in the large-N limit. This is so because a longer time series increases the number of discrete frequencies at which the power spectrum is sampled, rather than its accuracy at any one of them.

Fig. 5.3 displays the periodograms of the heat fluxes of the four systems presented in Sec. 5.1.1 (liquid Ar, liquid H_2O, crystalline MgO, and amorphous SiO_2), obtained from a 100 ps (500 ps for MgO) classical MD trajectory in the NVE ensemble and averaged over the three Cartesian components, showing the extremely noisy behaviour of the periodogram as an estimator of the spectrum. A consistent estimate of the value of the power spectrum at any frequency can be obtained by segmenting a time series into several blocks of equal length and then averaging over the sample spectra computed for each of them. When the length of the trajectory grows large, so does the number of blocks, thus making the variance of the average arbitrarily small. In practice, the determination of the optimal block size is a unwieldy process that leads to an inefficient determination of the length of the trajectory needed to achieve a given overall accuracy. Equivalently, a moving average [112] of the periodogram would consistently reduce the statistical noise, as happens in Fig. 5.3, but its *multiplicative* nature in Eq. (5.9) makes it difficult to disentangle the noise from the signal and may introduce a bias. Here we adopt a different approach enabling us to obtain a consistent estimate of the zero-frequency value of
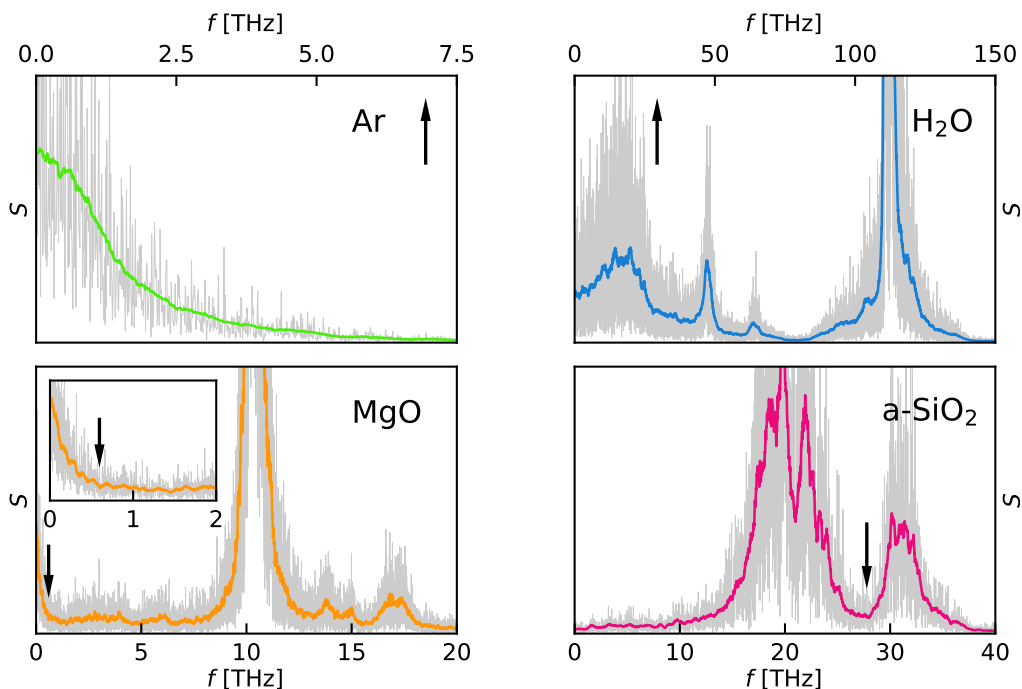
Figure 5.3: Sample power spectra of the heat flux computed from one MD trajectory for Ar, H_2O, a-SiO_2 (100 ps), and MgO (500 ps), obtained directly from Eq. (5.10), with $\ell = 3$ (gray line, see text). The x-axis is frequencies $f = \omega/2\pi$. The solid lines in color correspond to a moving average performed over a narrow frequency window of width 1 THz, usefult to reveal the main features of the spectrum. The vertical arrows indicate the cutoff frequencies, f^*, used for the subsequent cepstral analysis (see Sec. 5.2.5). The inset in the MgO panel is a magnification of the low-frequency region of the spectrum. Reproduced from Ref. [B].

the power spectrum from the statistical analysis of a *single* trajectory sample (*i.e.* no block analysis is needed) and such that the estimate of the trajectory length necessary to achieve a given accuracy is optimal.

5.2.2   Log-periodogram

Spectral density estimation from finite empirical time series is the subject of a vast literature in the statistical sciences, embracing both parametric and non-parametric methods [126]. In the following we propose a semi-parametric method to estimate the power spectrum of a stochastic process, based on a Fourier representation of the logarithm of its power spectrum (the "log-spectrum"). The advantage of dealing with the log-spectrum, instead of with the power spectrum itself, is twofold. First and foremost, the noise affecting the former is *additive*, instead of multiplicative, thus making it simple and expedient to apply linear filters: limiting the number of components of the Fourier representation of the log-spectrum acts as a low-pass filter that systematically reduces the power of the noise and yields a consistent estimator
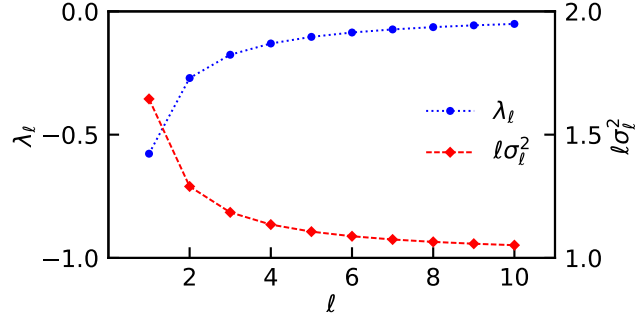
Figure 5.4: Expectation and variance of the $^\ell\lambda$ variables, as defined in Eqs. (5.12-5.14), as functions of the number of samples, ℓ, over which the periodograms are averaged.

of the log-spectrum at any given frequency. Second, as a bonus, the logarithm is usually smoother than its argument. Therefore, the Fourier representation of the logarithm of the power spectrum is more parsimonious than that of the spectrum itself.

Let $^\ell\hat{L}_k = \log(^\ell\hat{S}_k)$ be the "*log-periodogram*" of our time series. By taking the logarithm of Eq. (5.9), we can express $^\ell\hat{L}_k$ as:

$$
\begin{aligned}
^\ell\hat{L}_k &= \log(^\ell\hat{S}_k) \\
&= \log\left(S(\omega_k)\right) + \log(^\ell\xi_k) \\
&= \log\left(S(\omega_k)\right) + {}^\ell\Lambda + {}^\ell\lambda_k,
\end{aligned}
\tag{5.12}
$$

where

$$
^\ell\Lambda = \left\langle \log(^\ell\xi) \right\rangle = \int_0^\infty \log\left(\frac{\xi}{2\ell}\right) P_{\chi^2_{2\ell}}(\xi)\,d\xi = \psi(\ell) - \log(\ell)
\tag{5.13}
$$

is the expected value of the logarithm of the $^\ell\hat{\xi}$ stochastic variables defined in Eq. (5.11), $P_{\chi^2_{2\ell}}$ is the probability density of a $\chi^2_{2\ell}$ variate, $^\ell\lambda_k = \log\left(^\ell\xi_k\right) - {}^\ell\Lambda$ are zero-mean identically distributed independent stochastic variables, and $\psi(z)$ and is the digamma function [127]. The variance of the $^\ell\lambda$ variables is:

$$
\sigma_\ell^2 = \int_0^\infty \log\left(\frac{\xi}{2\ell}\right)^2 P_{\chi^2_{2\ell}}(\xi)\,d\xi - \lambda_\ell^2 = \psi'(\ell),
\tag{5.14}
$$

where $\psi'(z)$ is the tri-gamma function [127].

5.2.3 *Ceps*trum and *lif*tering

Eq. (5.12) explicitly shows that the sample log-spectrum of a time series is equal to the logarithm of the power spectrum one wishes to evaluate (modulo a constant), *plus* a (non-Gaussian) white noise. Whenever the number of (inverse) Fourier components of the logarithm of the power spectrum is much smaller than the length of the time series, applying a low-pass filter to Eq. (5.12) would result in a reduction
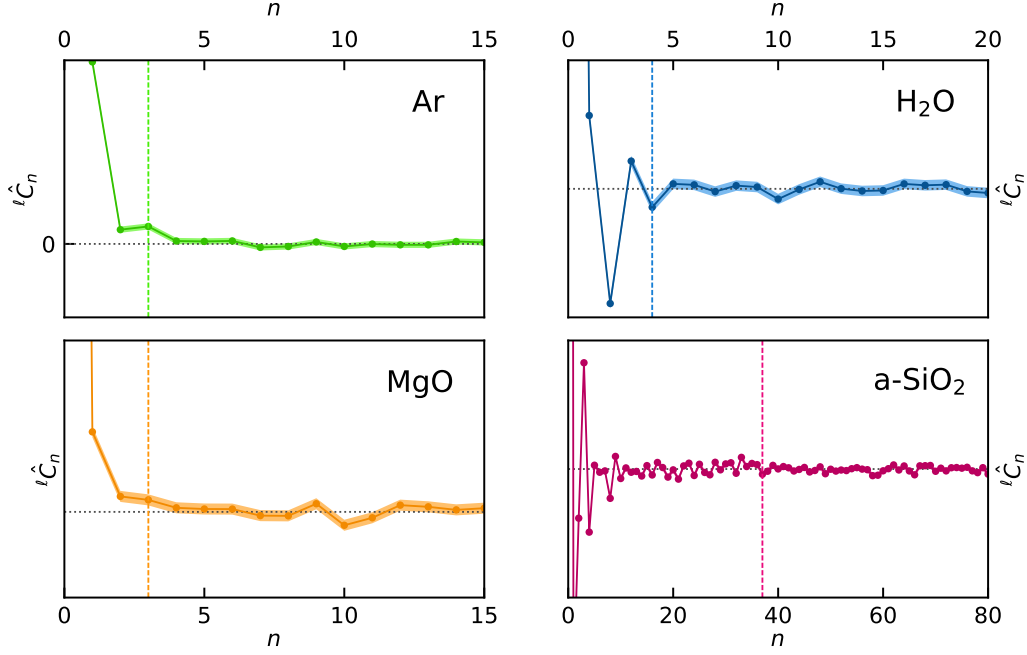
Figure 5.5: Cepstral coefficients of the heat flux computed from one MD trajectory for Ar, H_2O, a-SiO_2 (100 ps), and MgO (500 ps), analysing the low-frequency region of the periodogram (see Fig. 5.3) and defined in Eq. (5.15). The vertical dashed line indicates $(P^* - 1)$, *i.e.* the maximum coefficient summed in Eq. (5.18), chosen by the Akaike's information criterion, Eq. (5.27).

of the power of the noise, without affecting the signal. In order to exploit this idea, we define the "*cepstrum*" of the time series as the inverse Fourier transform of its sample log-spectrum [128]:

$$\ell\hat{C}_n = \frac{1}{N} \sum_{k=0}^{N-1} \ell\hat{L}_k \mathrm{e}^{-2\pi i \frac{kn}{N}}, \tag{5.15}$$

and its coefficients as the *cepstral coefficients* (or "*que*frencies"). A generalised central-limit theorem for Fourier transforms of stationary time series ensures that, in the large-N limit, these coefficients are a set of independent (almost) identically distributed zero-mean normal deviates [129, 130]. It follows that:

$$\ell\hat{C}_n = \lambda_\ell \delta_{n0} + C_n + \ell\mu_n, \tag{5.16}$$

$$C_n = \frac{1}{N} \sum_{k=0}^{N-1} \log\big(S(\omega_k)\big) \mathrm{e}^{-2\pi i \frac{kn}{N}}, \tag{5.17}$$

where $\ell\mu_n$ are independent zero-mean *normal* deviates with variances $\langle\ell\mu_n^2\rangle = \frac{1}{N}\sigma_\ell^2$ for $n \notin \{0, \frac{N}{2}\}$ and $\langle\ell\mu_n^2\rangle = \frac{2}{N}\sigma_\ell^2$ otherwise. This result can be easily checked explicitly by using the definition of the discrete Fourier transform; the non-trivial extra

information provided by the central-limit theorem is the asymptotic independence and normality of the $^\ell\mu$'s. Similarly to the sample power spectrum, the cepstral coefficients are real, periodic, and even: $\hat{C}_n = \hat{C}_{N-n}$.

In some sense, the cepstrum can be interpreted as a sort of correlation function in a pseudo-time domain. However, it differs from the original HCACF for the fact its coefficients are statistically independent and normally distributed, whereas the HCACF values at close time-lags are correlated. The word "*ceps*trum", obtained by reversing the first four letters of "spectrum", was coined to distinguish it from the power spectrum of a signal, and its coefficients essentially give information about the rate of change in the different spectrum bands. This concept has found many applications in voice recognition, pitch detection, characterisation of seismic and radar echoes, and more.

A thermal conductivity estimator

If the log-spectrum, $\log(S(f_k))$, is smooth enough, the number of non-negligible C_n coefficients in Eq. (5.17) is much smaller than N. For example, Fig. 5.5 displays the cepstral coefficients of the low-frequency region of the spectrum of the four systems (marked in Fig. 5.3), showing that only the first few coefficients are substantially different from zero. Therefore, let us indicate by P^* the smallest integer such that $C_n \approx 0$ for $P^* \leq n \leq N - P^*$. By limiting the Fourier transform of the sample cepstrum, Eq. (5.15), to P^* coefficients, we obtain an efficient estimator of the zero-frequency component of the log-spectrum as:

$$
\begin{aligned}
{}^\ell\hat{L}_0^* &= {}^\ell\hat{C}_0 + 2 \sum_{n=1}^{P^*-1} {}^\ell\hat{C}_n \\
&= {}^\ell\Lambda + \log(S_0) + {}^\ell\mu_0 + 2 \sum_{n=1}^{P^*-1} {}^\ell\mu_n \, .
\end{aligned}
\tag{5.18}
$$

Inspection of Eq. (5.18) shows that ${}^\ell\hat{L}_0^*$ is a normal estimator whose expectation and variance are:

$$
\langle {}^\ell\hat{L}_0^* \rangle = \log(S_0) + {}^\ell\Lambda \, ,
\tag{5.19}
$$

$$
\sigma_\ell^*(P^*, N)^2 = \frac{4P^* - 2}{N} \sigma_\ell^2 \, .
\tag{5.20}
$$

Using Eq. (5.6), we see that the logarithm of the conductivity can be estimated from the cepstral coefficients of the flux time series through Eqs. (5.18-5.20), and that the resulting estimator is always normal with a variance that depends on the specific system *only* through the number of these coefficients, P^*. Notice that the absolute error on the logarithm of the conductivity directly and nicely yields the relative error on the conductivity itself.

The value of P^* is a property of the stochastic process underlying the time series, and is therefore independent of N: for any given value of P^* the variance σ_ℓ^{*2} tends to zero in the large-N limit, and ${}^\ell\hat{L}_0^* - \Lambda_\ell$ is thus a consistent estimator of
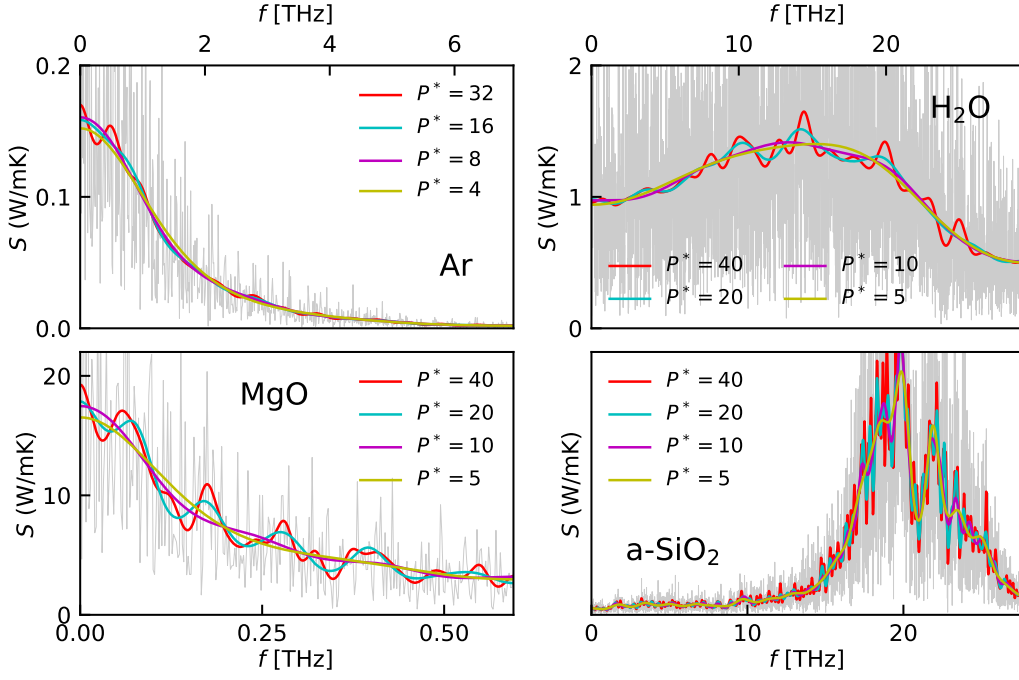
Figure 5.6: Filtered low-frequency region of the power spectrum of Ar, H_2O, MgO, and a-SiO_2 obtained by limiting the number of cepstral coefficients to P^*, as defined in Eq. (5.21). The lowest P^* is the cutoff value suggested by the Akaike's information criterion, Eq. (5.27). Grey curve: unfiltered periodogram obtained from Eq. (5.8).

$\log(S_0)$. In general, all the cepstral coefficients are different from zero and assuming that many of them actually vanish introduces a bias. The efficacy of this approach obviously depends on our ability to estimate the number of coefficients necessary to keep the bias introduced by the truncation to a value smaller than the statistical error (that increases with P^*), while maintaining the magnitude of the latter at a prescribed acceptable level.

The choice of P^* is the subject of *model selection* theory, another vast chapter in the statistical sciences [131]. Among the several tests that have been devised to perform this task, we choose the optimization of the Akaike's information criterion (AIC) [131, 132], as described in Sec. 5.2.4 below, but other more advanced *model selection* approaches [131] may be more effective.

In Fig. 5.6 we report the low-frequency region of the spectrum of the four analysed systems obtained by limiting the number of cepstral coefficients to P^*:

$$^{\ell}\hat{S}_k^* = \exp\left[2\sum_{n=1}^{P^*-1} {}^{\ell}\hat{C}_n e^{2\pi i \frac{kn}{N}} + {}^{\ell}\hat{C}_0 - {}^{\ell}\Lambda\right], \qquad (5.21)$$

thus showing the filtering effect (aka "*lif*tering", playing on the anagram theme)
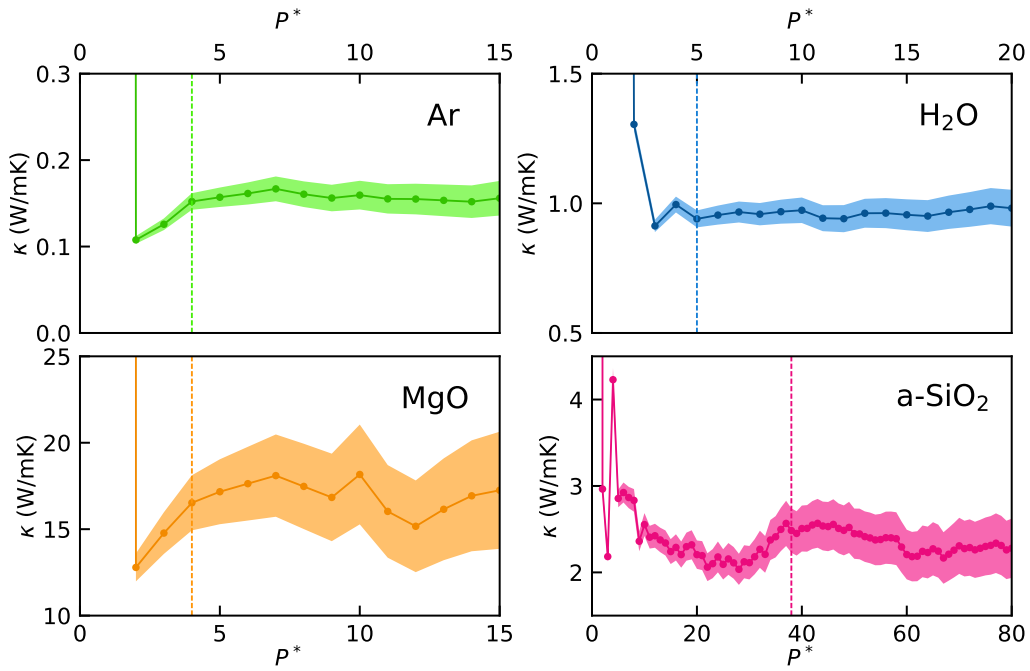
Figure 5.7: Thermal conductivity estimated from Eqs. (5.18-5.20) as a function of the cutoff P^* from one MD trajectory for Ar, H_2O, a-SiO_2 (100 ps), and MgO (500 ps). The colored bands indicate the statistical error estimated by the theory. The vertical dashed line indicates the value suggested by the Akaike's information criterion, Eq. (5.27), P_A^*.
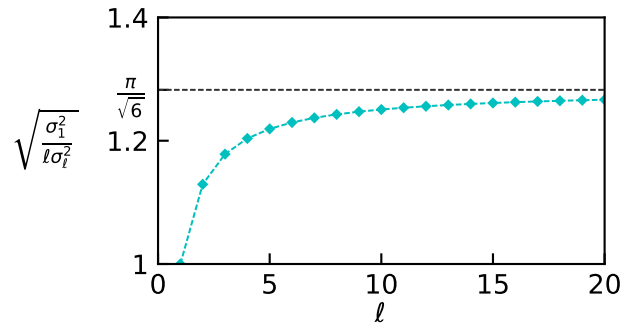
Figure 5.8: Ratio between the theoretical errors obtainable using method **(b)** (Eq. (5.23)) and method **(a)** (Eq. (5.22)). $\frac{\pi}{\sqrt{6}}$ is its asymptotic value.

of this choice. Finally, Fig. 5.7 shows the value of thermal conductivities obtained through Eqs. (5.18-5.20) as a function of P^*.

Single estimate or multiple estimates?

When estimating the value of L_0 from ℓ multiple samples of a same process, one has two options:

(a) compute the mean periodogram ${}^{\ell}\hat{S}_k$, Eq. (5.10), and then compute ${}^{\ell}\hat{L}_0^*$ from Eq. (5.18). This leads to Eq. (5.20):

$$\text{var}\left({}^{\ell}L_0^*\right) = \sigma_\ell^*\left(P^*, N\right)^2 ; \tag{5.22}$$

(b) compute the periodogram of each sample ${}^{1}\hat{S}_k$ individually, then weight average the estimator of ${}^{1}L_0^*$. This gives

$$\text{var}\left(\tfrac{1}{\ell}\sum_{i=1}^{\ell}{}^{1}\hat{L}_0^{*i}\right) = \tfrac{1}{\ell}\sigma_1^*\left(P^*, \tfrac{N}{\ell}\right)^2 . \tag{5.23}$$

In Fig. 5.8 we plot the ratio of the corresponding standard deviations, that is $\sqrt{\frac{\sigma_1^2}{\ell\sigma_\ell^2}} = \frac{\pi}{\sqrt{6\ell\psi'(\ell)}} > 1$: we conclude that it is more convenient to perform the average over the periodograms (a) instead of on the final estimator (b).

The dependence of σ_ℓ on ℓ (displayed in Fig. 5.4) gives us a leverage to reduce the variance of the estimate of L_0, essentially for free. Suppose one partitions each of the ℓ time series of N elements into m segments of N/m elements. When the segments are long enough, the sample average evaluated for each of them has the same variance as the value obtained from the entire trajectory, *i.e.* $\sigma_\ell^*(P^*, N/m)^2/m = \sigma_\ell^*(P^*, N)^2$, thus providing no improvement. If instead one evaluates L_0 from the mean periodogram averaged over the $\ell \times m$ segments, the corresponding variance would be $\sigma_{\ell m}^2(P^*, N/m)$, which is a decreasing function of m (see Fig. 5.4) and tends to $\frac{4P^*-2}{\ell N}$ for $\ell m \gg 1$. In practice the asymptotic behaviour $\sigma_\ell^2 = \psi'(\ell) \approx 1/\ell$ is reached for $\ell \gtrsim 6$ ($6\sigma_6^2 \approx 1.09$), and we propose to use $m = 6$ segments when only one time series is available ($\ell = 1$), thus reducing the standard deviation by a factor $\sqrt{\frac{\sigma_1^2}{6\sigma_6^2}} \approx 1.23$. When three times series are available, such as in the simulation of thermal transport in isotropic materials ($\ell = 3$), the advantage of segmenting the trajectory by choosing *e.g.* $m = 2$ segments would be marginal ($\sqrt{\frac{3\sigma_3^2}{6\sigma_6^2}} \approx 1.04$), and we choose therefore to keep $m = 1$.

5.2.4 Akaike Information Criterion

We summarise here the AIC, a simple model selection criterion that one can adopt to choose an optimal value of P^*, in an easily automatable way and without relying on any subjective criterion.

Given a model depending on P parameters, $\theta = \{\theta_1, \theta_2, \cdots \theta_P\}$, the AIC [131, 132] is a sample statistic defined as

$$\text{AIC}(P) = -2\max_{\theta}\log\mathcal{L}(\theta, P) + 2P, \tag{5.24}$$

where $\mathcal{L}(\theta, P)$ is the likelihood of the parameters. The optimal number of parameters is determined as the argument of the AIC minimum:

$$P_A^* \equiv \arg\min_P \text{AIC}(P). \tag{5.25}$$

In the present case the parameters of the model are the P coefficients $C = \{C_0, C_1, \cdots C_{P-1}\}$ as defined in Eq. (5.17), and the log-likelihood reads, up to additive terms independent of P and C:

$$2\log\mathcal{L}(C, P) = -\frac{N}{2\sigma_\ell^2}\left(C_0 + \Lambda_\ell - \hat{C}_0\right)^2 - \frac{N}{\sigma_\ell^2}\sum_{n=1}^{P-1}\left(C_n - \hat{C}_n\right)^2 - \frac{N}{\sigma_\ell^2}\sum_{n=P}^{N/2}\hat{C}_n^2. \tag{5.26}$$

Evidently, the above expression is maximized, for given P, by $C_n = \hat{C}_n - \delta_{n0}\Lambda_\ell$ for $n = 0, 1, \cdots P - 1$, and the corresponding value of the maximum is: $2\max_C \log\mathcal{L}(C, P) = -\frac{N}{\sigma_\ell^2}\sum_{n=P}^{N/2}\hat{C}_n^2$. We conclude that the value of the AIC is:

$$\text{AIC}(P) = \frac{N}{\sigma_\ell^2}\sum_{n=P}^{N/2}\hat{C}_n^2 + 2P. \tag{5.27}$$

The value of P that minimizes this expression is the optimal number of parameters in the Akaike sense, P_A^*, as defined in Eq. (5.25). In Fig. 5.5 and 5.7 the value P_A^* chosen by the AIC for the four systems is indicated by vertical dashed lines.

5.2.5 Nyqvist frequency

The maximum frequency available for spectral/cepstral analysis is the Nyqvist frequency [108], determined by the sampling period ϵ as $f_{\text{Ny}} = \frac{1}{2\epsilon}$ (*i.e.* angular frequency $\omega_{\text{Ny}} = 2\pi f_{\text{Ny}}$). Transport coefficients only depend on the low-frequency behaviour of the spectrum, which is independent of ϵ, as long as the latter is small enough as to avoid aliasing effects. For this reason it may prove convenient to eliminate the high-frequency portion of the spectrum ($f > f^*$) by applying a low-pass filter to the time series (*e.g.* a moving average [112]) and then resample the latter with a sampling period $\epsilon^* = \frac{1}{2f^*}$, thus resulting in a time series of $N^* = N\frac{f^*}{f_{\text{Ny}}}$ time steps.

The optimal number of cepstral coefficients resulting from Eqs. (5.25) and (5.27), as well as the error in the estimate of the transport coefficients resulting from Eq. (5.20), depends in general on the choice of the cutoff frequency, f^*. The smaller f^*, the smaller will presumably be the number of cepstral coefficients necessary to describe the log-spectrum to any given accuracy over such a shorter frequency range. However, the shorter length of the filtered time series, N^*, results in an increased variance of the estimator $^\ell\hat{L}_0^*$ defined in Eq. (5.18), according to Eq. (5.20). Numerical experiments performed on the MD data reported in Sec. 5.2.7 and Fig. 5.12 show that both the estimated value of $^\ell\hat{L}_0^*$ and its variance are actually fairly insensitive to the value chosen for the cutoff frequency, f^*, provided that the power spectrum of the re-sampled time series faithfully features the first band of the original spectrum (*i.e.* the first prominent feature) and that this band is not too peaked at the origin.

5.2.6   Data analysis work-flow (solids and one-component fluids)

We summarise the steps leading to the estimation of thermal conductivity by the *cepstral analysis* method, in order to highlight the simplicity of its practical implementation.

1. From a MD simulation compute the energy flux time series J_n^i, $i = 1, \cdots \ell$ (usually $\ell = 3$ cartesian components).

2. Compute the discrete Fourier transform of the fluxes, $\tilde{J}_k^i$, and the mean-periodogram $^\ell \hat{S}_k$ from Eqs. (5.8) and (5.10), and smooth it out using *e.g.* a moving average [112] performed over a narrow frequency window, so as to reduce the statistical noise to a level where the shape of the power spectrum of the underlying process can be appreciated.[4]

3. Only a selected low-frequency region shall be used in the next steps (see Sec. 5.2.5 and 5.2.7 for a detailed discussion): choose a cutoff frequency, f^*, so as to encompass the first band of the smoothed power spectrum.

4. Compute the log-periodogram $^\ell \hat{L}_k = \log(^\ell \hat{S}_k)$.

5. Compute the inverse discrete Fourier transform of the result to obtain the cepstral coefficients $^\ell \hat{C}_n$, Eq. (5.15).

6. Apply the Akaike Information Criterion, Eqs. (5.25) and (5.27), to estimate the number of cepstral coefficients to retain, P^*.

7. Finally apply Eq. (5.18) to obtain $^\ell \hat{L}_0^*$, and evaluate the thermal conductivity as

$$\kappa = \frac{\Omega}{2k_B T^2} \exp\left[\hat{L}_0^* - \psi(\ell) + \log(\ell) \right], \qquad (5.28)$$

and its statistical error as

$$\frac{\Delta \kappa}{\kappa} = \sqrt{\psi'(\ell) \frac{4P^* - 2}{N}}. \qquad (5.29)$$

---

[4]Mind the difference between the moving average performed in the frequency domain to smooth out the power spectrum and that performed in the time domain, as suggested before, and acting as a low-pass filter. Spectral smoothing using a moving average in the frequency domain is common practice in the analysis of time series, and it actually provides a consistent estimator of the power spectrum. In fact, the number of frequencies falling within a window of given width increases linearly with the length of the series, so that the variance of the average decreases as the inverse of the product of the length of the series times the width of the window. The resulting spectral estimate is however biased by the variation of the signal within the window, thus strongly reducing the width of the windows that can be afforded. Moreover, both the bias and the statistical error are difficult to estimate, due to the multiplicative nature of the noise; therefore neither the plain periodogram nor a running average thereof are adequate for a quantitative estimate of the zero-frequency value of the power spectrum, which is proportional to the transport coefficient we are after.

5.2.7 Benchmarks

The cepstral analysis method just presented has been implemented in a Python package, THERMOCEPSTRUM [133], and benchmarked for the calculation of the thermal conductivity of the four representative systems presented in Sec. 5.1.1: liquid Ar, liquid H_2O, crystalline MgO and amorphous SiO_2. After equilibration, data were collected in the NVE ensemble for trajectories whose length was chosen so as to represent realistic simulation runs that could be afforded using *ab initio* MD ($\mathcal{T} = 100\,\text{ps}$ for Ar, H_2O, and a-SiO_2, and $\mathcal{T} = 500\,\text{ps}$ for MgO). In order to compare our estimates of the transport coefficients and their statistical errors with reliable and statistically significant reference data, in all cases we ran much longer ($\approx 50\,\text{ns}$) simulations. This allowed us to compare our predicted conductivities with accurate values estimated from the direct integration of the GK equation, Eqs. (5.2) and (5.3), as obtained from a block average [82] performed over the long trajectory (see Sec. 5.1.2). In addition, we could collect abundant statistics of our estimator for the transport coefficients, Eq. (5.18), and validate its normal distribution specified by Eqs. (5.19) and (5.20).

The periodograms of one segment of each system are reported in Fig. 5.3, where a moving average in also computed in order to reveal the main features of the power spectrum. The values of the cutoff frequencies used for cepstral analysis, f^*, are chosen so as to encompass the first prominent feature of the (smoothed) power spectrum. For instance, in H_2O and a-SiO_2 we choose $f^* \approx 29\,\text{THz}$ and $f^* \approx 28\,\text{THz}$, respectively. In MgO we assume $f^* \approx 0.6\,\text{THz}$, just at the upper edge of the first narrow peak, whereas in Ar there is just one band, corresponding to a purely diffusive behaviour of a simple fluid, and we assume $f^* \approx 7\,\text{THz}$, where the spectrum has exhausted most of the available power, but its value is not yet too small (see Fig. 5.3). The corresponding average numbers of cepstral coefficients given by the optimization of the AIC are: $P_A^* = 5$ (Ar), 7 (H_2O), 4 (MgO), and 31 (a-SiO_2). Later we will display the dependence of the number of optimal cepstral coefficients and of the resulting estimate of the thermal conductivity on the choice of f^*, and show that this choice is not critical.

In order to validate our data-analysis protocol, we first computed the heat conductivities from a direct integration of the current autocorrelation function, Eqs. (5.2) and (5.3), combined with standard block analysis over the 50 ns long trajectory (see Sec. 5.1.2), that will be taken as a reference, obtaining: $\kappa_{\text{ref}} = 0.1965 \pm 0.0015$, 0.970 ± 0.009, 19.2 ± 0.4, and $2.115 \pm 0.025\,\text{W/mK}$, for Ar, H_2O, MgO, and a-SiO_2, respectively. Although our simulations were meant for benchmarking purposes only, and no particular attention was paid to exactly match the simulation conditions of previous work, these data are in fair agreement with the foregoing theoretical results: $\approx 0.19\,\text{W/mK}$ (Ar) [103], $\approx 0.85\,\text{W/mK}$ (H_2O) [134], $\approx 12\,\text{W/mK}$ (MgO) [105], and $\approx 2.1\,\text{W/mK}$ (a-SiO_2) [135].

Distribution of the estimator of κ

In Fig. 5.9 we display the distributions of the values of $\log(\kappa/\kappa_{\text{ref}})$ estimated by applying our protocol to multiple MD segments of 100 ps (for Ar, H_2O, a-SiO_2) and
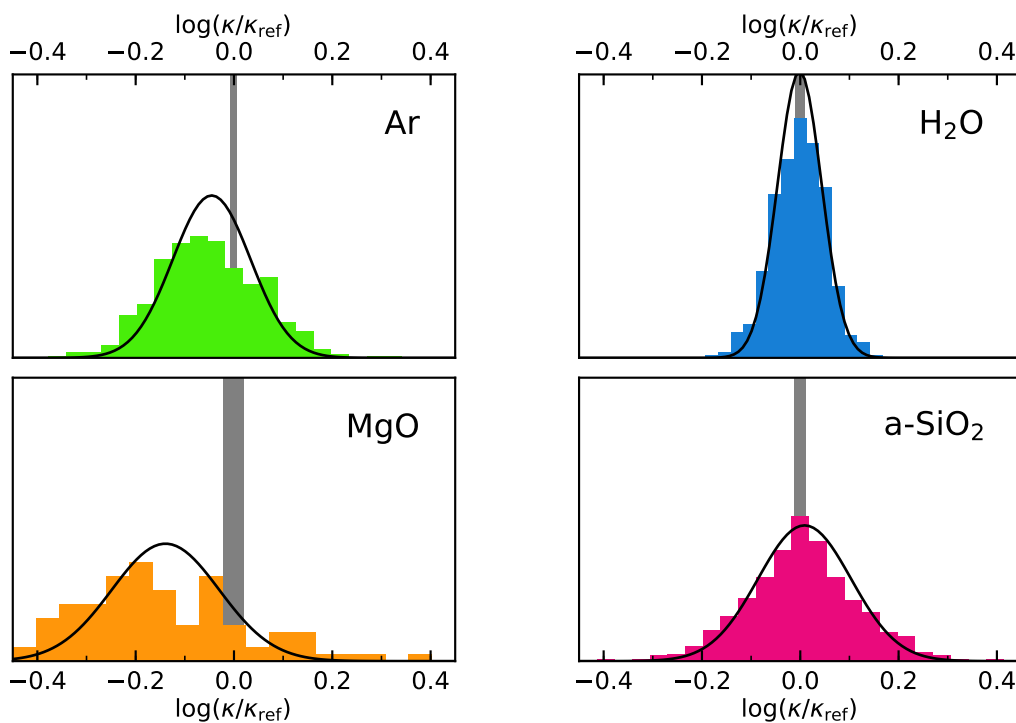
Figure 5.9: Distributions of the logarithm of the thermal conductivities, $\log(\kappa)$, estimated over multiple MD segments (100 ps for Ar, H_2O, and a-SiO_2, and 500 ps for MgO) extracted from a 50 ns long trajectory. The reported data are referred to κ_{ref}, which is the value obtained from a direct integration of the GK equation, combined with standard block analysis over the 50 ns trajectory, and represented by the vertical gray bands. The Gaussian curves represent the distributions predicted by the theory, centered at the sample mean. Remember that the absolute error on $\log(\kappa)$ is the relative error on κ. Reproduced from Ref. [B].

500 ps (for MgO), extracted from the 50 ns long trajectory. The optimal numbers of cepstral coefficients, P^*, have been redetermined for each segment independently, while the values of the cutoff frequency, f^*, which only depends on the qualitative features of the spectrum, have been determined once for all for one of them. The distribution of the resulting number of cepstral coefficients is reported in Fig. 5.10. The observed distributions of $\log(\kappa)$ successfully pass the Shapiro-Wilk normality test [136] (*i.e.* they do not fail it) and the observed sample standard deviations closely match the theoretical values estimated from Eq. (5.20), as reported in Table 5.1. Remember that the error on $\log(\kappa)$ is the relative error on κ: the corresponding absolute errors achievable with a short trajectory of 100 (Ar, H_2O, and a-SiO_2) or 500 (MgO) ps, not to be confused with the long trajectory used to establish the reference data above, are therefore: $\sigma_\kappa \approx 0.015$ (Ar), 0.045 (H_2O), 2 (MgO), and 0.2 (a-SiO_2) W/mK. This indicates that a *single* and short sample trajectory, such as one that is affordable with *ab initio* MD, is sufficient to achieve and accurately estimate a very decent relative error on the computed transport coefficient. In an
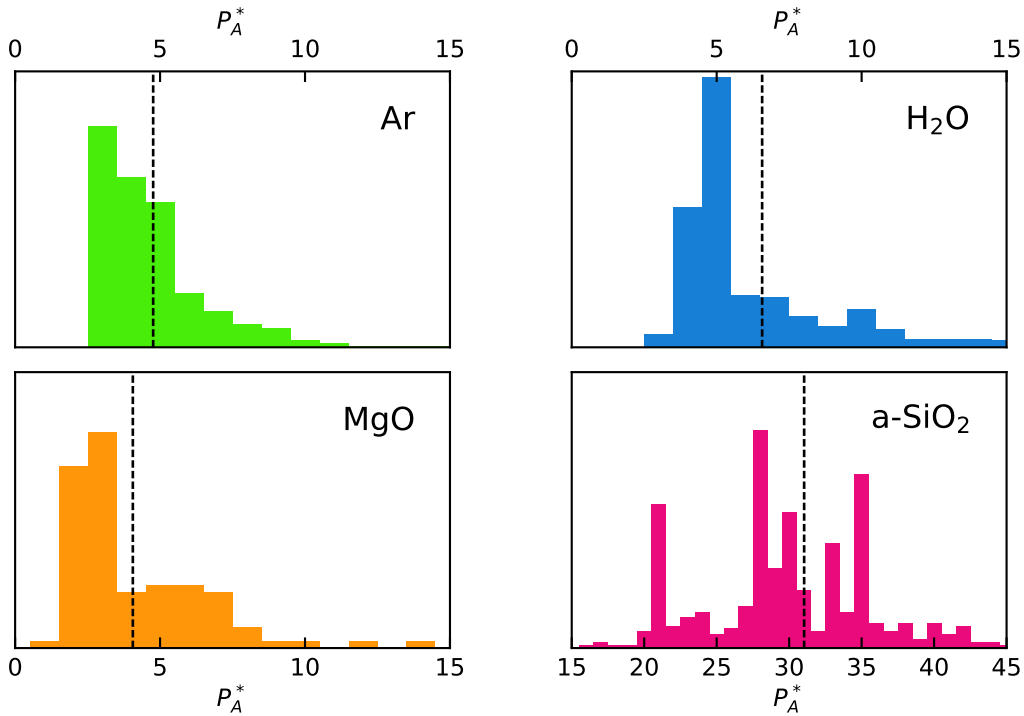
Figure 5.10: Distribution of the optimal numbers of cepstral coefficients, P_A^*, as determined by optimizing the Akaike's information criterion, Eqs. (5.25) and (5.27), for each segment of the 50 ns long MD trajectory, as described in Sec. 5.2.4. The vertical dashed lines indicate the average value of P_A^*. Reproduced from Ref. [B].

	sample	theory
Ar (100 ps)	0.104	0.079
H$_2$O (100 ps)	0.053	0.045
MgO (500 ps)	0.17	0.11
a-SiO$_2$ (100 ps)	0.114	0.095

Table 5.1: Observed and theoretical standard deviations of the distributions of $\log(\kappa)$, displayed in Fig. 5.9. The theoretical values are obtained from Eq. (5.20). Remember that the absolute error on $\log(\kappa)$ is the relative error on κ.

attempt to evaluate the thermal conductivity from the direct computation of the GK equation, Eqs. (5.2) and (5.3), and standard block analysis using similarly short MD trajectories, our best estimate of the resulting statistical error was 2-3 times larger than using our protocol (meaning $5 - 10\times$ longer trajectories to achieve a comparable accuracy) in all cases but liquid Ar, where only a marginal improvement is achieved using our methodology. Much more than this, the standard analysis of MD data depends on a number of hidden parameters, such as the upper limit of the
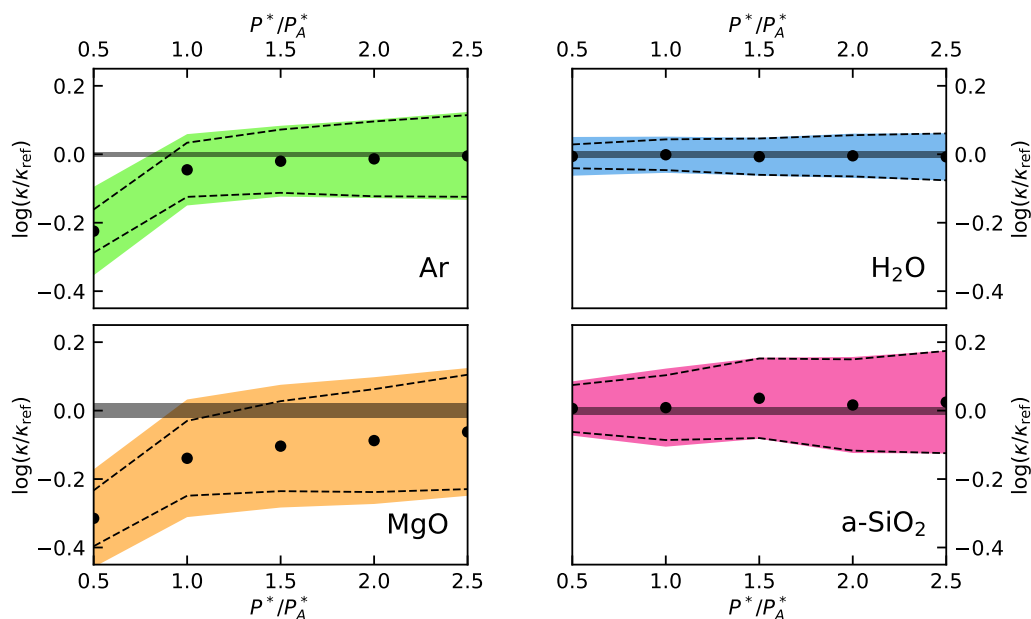
Figure 5.11: Dependence of $\log(\kappa)$, as estimated from Eq. (5.18), on the number of cepstral coefficients P^*. P_A^* is the optimal number of coefficients estimated from the AIC using Eqs. (5.25) and (5.27). The black dots represent the mean values of $\log(\kappa)$ computed over multiple MD segments (100 ps for Ar, H_2O, and a-SiO_2, and 500 ps for MgO) extracted from a 50 ns long trajectory; the colored bands and dashed lines represent one standard deviation as estimated from the empirical statistics and from Eq. (5.20), respectively. The reported data are referred to κ_{ref}, which is the value of thermal conductivity obtained from a direct integration of the GK equation, combined with standard block analysis over the 50 ns trajectory, and represented by the horizontal gray bands. Remember that the absolute error on $\log(\kappa)$ is the relative error on κ. Reproduced from Ref. [B].

GK integral, Eq. (5.2), or the width of the blocks for error analysis, that are hard to determine and keep under control, as discussed in Sec. 5.1.2. Our method, instead, only depends on a single parameter, the number of cepstral coefficients, whose optimal value can be easily determined from the Akaike's information criterion, or other more sophisticated model-selection methods [131, 137], as appropriate.

Bias

In order to estimate the bias introduced by limiting the number of cepstral coefficients, we examined the sample mean of the estimator of κ, $\langle\kappa\rangle$, computed over the distributions displayed in Fig. 5.9, obtaining the values reported in Table 5.2. Comparing these data with the reference data obtained from the direct evaluation of the GK integral, we see that the bias is negligible for H_2O and a-SiO_2, very small for Ar, and small but not negligible for MgO. In Fig. 5.11 we display the dependence of $\log(\kappa/\kappa_{ref})$ on the number of cepstral coefficients, P^*, as estimated from Eq. (5.18). We observe that when the number of cepstral coefficients, P^*, is larger than the

	$\langle \kappa \rangle$	κ_{ref}
Ar	0.1878 ± 0.0007	0.1965 ± 0.0015
H$_2$O	0.969 ± 0.002	0.970 ± 0.009
MgO	16.7 ± 0.2	19.2 ± 0.4
a-SiO$_2$	2.131 ± 0.009	2.115 ± 0.025

Table 5.2: Sample mean of the estimated κ, computed over the distributions displayed in Fig. 5.9; and reference values of thermal conductivity, κ_{ref}, obtained from the direct integration of the GK equation over the 50 ns trajectory. Units are W/mK.

optimal value determined from the AIC, P_A^*, the estimated value of κ seems not to depend on P^* for all systems but MgO, for which a slight bias seems to persist, and to a much lesser extent for Ar. Also, Eq. (5.20) seems to slightly underestimate the sample variance for small P^* in these cases. In the case of MgO this behaviour is likely due to the difficulty of the AIC to cope with the sharp low-frequency peak in the power spectrum, due to the highly harmonic character and slow decay of the vibrational heat carriers in periodic crystals [42], thus requiring longer simulation times. In the case of Ar the very small bias observed for $P^* = P_A^*$ may be due to the difficulty of choosing a suitable cutoff frequency when only a single diffusive band is present in the spectrum, and to the divergence of the log-spectrum at high frequency. In all cases, use of the Aikake's information criterion results in a bias that is smaller than the statistical error estimated from an individual short sample trajectory and that can be systematically removed by increasing the value of P^*, at the price of increasing the statistical error, if and when needed.

Cutoff frequency f^*

In Fig. 5.12 we report the dependence of the optimal number of cepstral coefficients, P_A^*, as a function of the cutoff frequency, f^*, along with the dependence of the resulting estimate of $\log(\kappa/\kappa_{\mathrm{ref}})$. P_A^* increases (roughly linearly) with f^*. Notwithstanding, the estimated value of the heat conductivity, as well as its variance, is fairly insensitive on the precise value of f^* as long as the latter is large enough as to encompass the lowermost prominent feature of the spectrum. Some more comments are in order for MgO. In this case the high thermal conductivity, due to the strong harmonic character of slowly decaying phonon modes, manifests in the form of a narrow peak centered at $f = 0$, followed by a broad plateau that carries little spectral weight. This feature determines a more pronounced increase in the number of significant cepstral coefficients as f^* increases and a corresponding increase of the bias when keeping P^* at the value given by the AIC. In this case, the AIC is a less reliable indicator of the number of cepstral coefficients necessary to keep the bias low. By increasing this number by a factor of two or more, the bias decreases, as indicated by the results reported in lighter colors in Fig. 5.12, and eventually vanishes, as shown in Fig. 5.11.
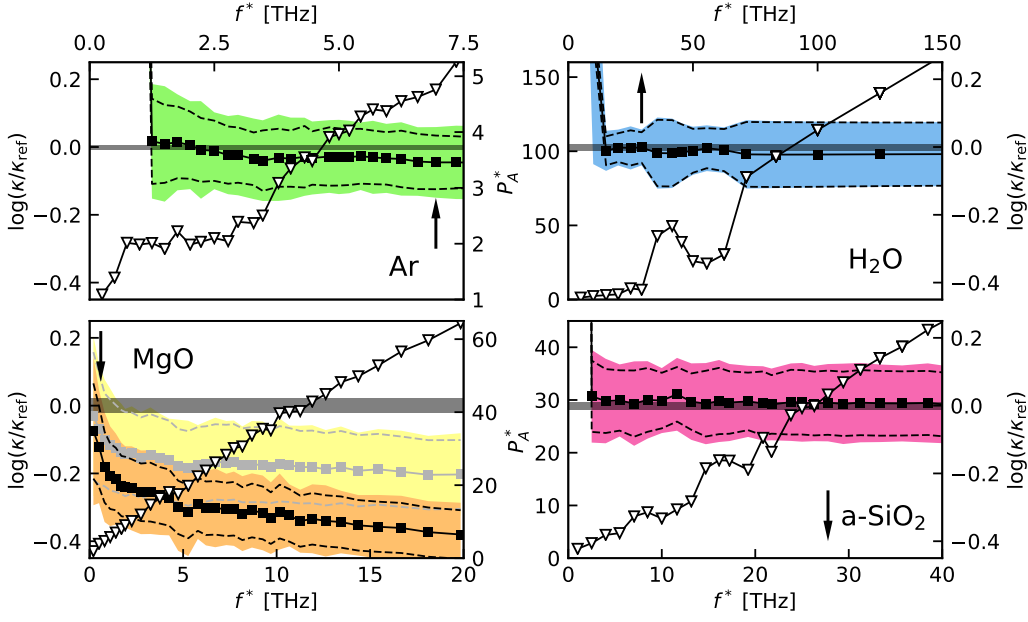
Figure 5.12: Triangles: average optimal number of cepstral coefficients, P_A^*, as determined by the AIC, Eqs. (5.25) and (5.27), as a function of the cutoff frequency used for cepstral analysis, f^* (see discussion just after Eq. (5.27)). Squares: $\log(\kappa)$ resulting from a given choice of f^* and of the corresponding value of P_A^*. All the values are averages performed over multiple 100 ps long segments (500 ps for MgO) extracted from a 50 ns long MD trajectory, as discussed in the text. The colored bands indicate the sample standard deviation and the dashed lines that resulting from our theoretical analysis (see Eq. (5.20)). The vertical arrows indicate the cutoff frequencies, f^*, used for the cepstral analysis in this paper (see Fig. 5.3 and text). In the case of MgO, the data indicated with lighter colors are obtained using a number of cepstral coefficients twice as large as that provided by the AIC, $P^* = 2P_A^*$. The data are referred to κ_{ref}, which is the value of thermal conductivity obtained from direct integration of the GK equation over the 50 ns trajectory, and represented by the horizontal gray bands. Remember that the absolute error on $\log(\kappa)$ is the relative error on κ. Reproduced from Ref. [B].

Trend with simulation length

The estimate of κ of Ar, H_2O, and a-SiO_2 obtained from a *single* trajectory segment of 100 ps is very good. As a function of the cutoff frequency f^*, $\log(\kappa)$ oscillates around an average value that is compatible with the distributions of Fig. 5.9. Using a longer trajectory segment the magnitude of these oscillations decreases, making the estimate of κ more stable at different f^*, which is compatible with the reduced variance of its distribution. In the case of MgO, instead, it appears that by increasing the trajectory length N the bias decreases, and the value of $\log(\kappa)$ becomes less and less dependent upon the f^* choice, if we set $P^* = P_A^*$. The number of frequencies used for the cepstral analysis is equal to $N/2$, and the frequency resolution is $\Delta f = \frac{1}{N\epsilon}$. In a crystalline system like MgO, the long-living phonon modes

manifest themselves as a slowly decaying HCACF (*i.e.* a long autocorrelation time) and a sharp peak at $f \approx 0$ in the spectrum. In order to adequately sample the low-frequency region, a longer trajectory is thus required. Whether it is possible to define a minimum simulation length necessary to optimize the estimate of κ in such critical cases is an issue that should be studied more extensively, possibly by analysing synthetic analytic stochastic time series that can reproduce similar power spectra. We believe that our model selection criterion can be improved to perform better in this critical class of systems.

There are two filtering operations that can possibly introduce some spurious effect into the estimate of κ. The first is the low-pass filter applied to the time series before resampling, usually a moving average, that is a rectangular window. The type of filter used in this instance will affect the highest frequencies of the spectrum of the resampled heat current (due to aliasing effects and to an effect called *spectral leakage*). The second effect happens when we cut off the cepstrum at P^*. Setting a hard cutoff at P^* will result in a low-filtered signal equal to the original log-periodogram convolved with a sinc function (the Fourier transform of a rectangular window). This may not be the optimal choice and the estimated log-periodogram will be affected by this, in a certain measure. Therefore, both these filtering operations may add some subtle effects to the estimate of κ and should be studied more extensively, in the future.

5.3 Multi-component fluids

In Sec. 2.3.2 we have seen that in a fluid made of Q atomic species there are in general Q macroscopic fluxes interacting with each other through Onsager's phenomenological equations, Eq. (2.9), not counting the different Cartesian components that do not interact amongst themselves because of space isotropy. A MD simulation thus samples Q stochastic processes, one for each interacting flux, that we suppose to be stationary. These processes can be thought of as different components of a same multivariate process. Therefore, we can easily generalize the cepstral analysis method presented in Sec. 5.2 to these systems [D].

5.3.1 Cepstral analysis

As in Sec. 5.2, for the sake of generality we suppose to have ℓ independent samples of such a process, described by a multivariate time series of length N: $\{{}^pJ_n^i\}$; $p = 1, \ldots \ell$; $i = 1, \ldots Q$; $n = 0, \ldots N - 1$. Stationarity implies that $\langle J_n^i \rangle$ does not depend on n and that $\langle J_n^i J_m^j \rangle$ only depends on $n - m$. We will further assume that $\langle J_n^i \rangle = 0$ and that $\langle J_n^i J_0^j \rangle$ is an even function of n, which is the case when J^i and J^j have the same signature under time-reversal. By combining Eq. (2.48) with Eq. (2.25), we see that in order to evaluate the thermal conductivity in the multi-component case we need an efficient estimator for $\left(S_0^{-1}\right)^{11}$, where $S_0^{kl} = S^{kl}(\omega = 0)$ is the zero-frequency

cross-spectrum of the relevant fluxes, ordered in such a way that the energy one is the first.

Similarly to the one-component case, we define a mean sample cross-spectrum (or *cross-periodogram*) as

$$^{(\ell Q)}\hat{S}_k^{ij} = \frac{1}{\ell} \sum_{p=1}^{\ell} \frac{\epsilon}{N} \left(^p\tilde{J}_k^i\right)^* {}^p\tilde{J}_k^j. \tag{5.30}$$

By discretizing Eq. (2.24) we see that $^{(\ell Q)}\hat{S}_k^{ij}$ is an unbiased estimator of the cross-spectrum, $\left\langle ^{(\ell Q)}\hat{S}_k^{ij} \right\rangle = S^{ij}\left(\omega_k = \frac{2\pi k}{N\epsilon}\right)$. As it was the case for univariate processes, in the large-N limit the real and imaginary parts of $\tilde{J}_k^i$ are normal deviates that are uncorrelated for $k \neq k'$. We conclude that the cross-periodogram is a random matrix distributed as a complex Wishart deviate [138, 139]:

$$^{(\ell Q)}\hat{S}_k \sim \mathcal{CW}_Q\left(S(\omega_k), \ell\right). \tag{5.31}$$

The notation $\mathcal{CW}_Q\left(S, \ell\right)$ in Eq. (5.31) indicates the distribution of the $Q \times Q$ Hermitian matrix $^{(\ell Q)}\hat{S}^{ij} = \frac{1}{\ell}\sum_{p=1}^{\ell} {}^pX^i\, {}^pX^{j*}$, where $\{^pX^i\}$ ($p = 1, \cdots \ell$, $i = 1, \cdots Q$) are ℓ samples of an Q-dimensional zero-mean normal variate whose covariance is $S^{ij} = \langle X^i X^{j*} \rangle$.

Similarly to the real case, a Bartlett decomposition [140] holds for complex Wishart matrices [141], reading:

$$^{(\ell Q)}\hat{S} = \frac{1}{\ell}\mathcal{S}RR^\top\mathcal{S}^\dagger, \tag{5.32}$$

where "$\top$" and "$\dagger$" indicate the transpose and the adjoint of a real and complex matrix, respectively; $\mathcal{S}$ is the Cholesky factor of the covariance matrix, $S = \mathcal{S}\mathcal{S}^\dagger$, and R is a real lower triangular random matrix of the form

$$R = \begin{pmatrix} c_1 & 0 & 0 & \cdots & 0 \\ n_{21} & c_2 & 0 & \cdots & 0 \\ n_{31} & n_{32} & c_3 & \cdots & 0 \\ \vdots & \vdots & \vdots & \ddots & \vdots \\ n_{Q1} & n_{Q2} & n_{Q3} & \cdots & c_Q \end{pmatrix}, \tag{5.33}$$

where $c_i^2 \sim \chi_{2(\ell-i+1)}^2$ and $n_{ij} \sim \mathcal{N}(0,1)$. We stress that R is independent of the specific covariance matrix, and only depends upon ℓ and Q. In particular it is independent of the ordering of the fluxes J^i. By expressing the QQ matrix element of the inverse of $^{(\ell Q)}\hat{S}$ in Eq. (5.32) as the ratio between the corresponding minor and the full determinant, and using some obvious properties of the determinants and of triangular matrices, we find that:

$$\frac{\ell}{\left(^{(\ell Q)}\hat{S}_k^{-1}\right)^{QQ}} = \frac{1}{\left(S_k^{-1}\right)^{QQ}}c_Q^2, \tag{5.34}$$
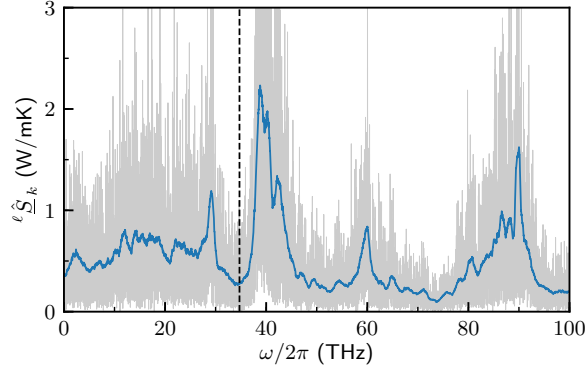
Figure 5.13: Multi-component power spectrum, as defined in Eq. (5.35), for a classical flexible model of a solution of water and ethanol 50 mol%, obtained from a 100 ps trajectory. Grey: $^{\ell}\hat{\underline{S}}_k$ obtained directly from Eq. (5.35), with $\ell = 3$ and $Q = 2$. Blue: $^{\ell}\hat{\underline{S}}_k$ filtered with a moving average window of width 1 THz in order to reveal its main features. The vertical dashed line delimits the low-frequency region used in the subsequent cepstral analysis. Reproduced from Ref. [D].

As the ordering of the fluxes is arbitrary, a similar relation holds for all the diagonal elements of the inverse of the cross-periodogram. We conclude that the generalization of Eq. (5.10) for the multi-component case is:

$$^{\ell}\hat{\underline{S}}_k \equiv \frac{\ell}{2(\ell - Q + 1)} \frac{1}{\left(^{(\ell Q)}\hat{S}_k^{-1} \right)^{11}} = \frac{1}{\left(S_k^{-1} \right)^{11}} \xi_k, \qquad (5.35)$$

where ξ_k are independent random (with respect to k) random variables, distributed as

$$\xi_k \sim \begin{cases} \frac{1}{\ell - Q + 1} \chi^2_{\ell - Q + 1} & \text{for } k \in \{0, \frac{N}{2}\}, \\ \\ \frac{1}{2(\ell - Q + 1)} \chi^2_{2(\ell - Q + 1)} & \text{otherwise.} \end{cases} \qquad (5.36)$$

Starting from here we can apply the cepstral analysis as in the one-component case. The only difference is the number of degrees of freedom of the χ^2 distribution, that becomes $2(\ell - Q + 1)$, and a different factor in front of the result. Fig. 5.13 shows an example of multi-component power spectrum for a solution of water and ethanol.

5.3.2 Discussion

The method discussed so far shows a fundamental advantage with respect to a naïve implementation of direct time-integration approach. Fig. 5.14 shows the two-component conductivity κ, obtained via Eq. (5.3) as a function of the upper time-integration limit $\mathcal{T}$,

$$\kappa(\mathcal{T}) = \frac{1}{T^2} \left(L^{EE}(\mathcal{T}) - \frac{(L^{EQ}(\mathcal{T}))^2}{L^{QQ}(\mathcal{T})} \right), \qquad (5.37)$$

(a)   (b)
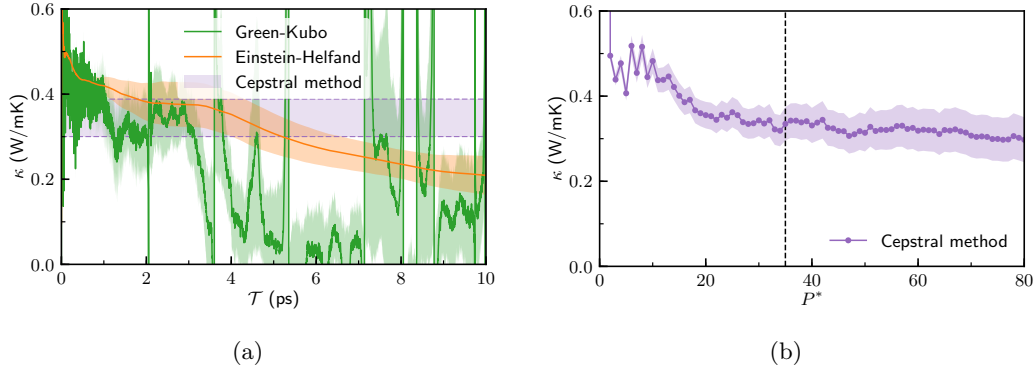
Figure 5.14: Convergence of the multi-component thermal conductivity estimator κ using the direct time-integration approach and the cepstral method, for a classical flexible model of a solution of water and ethanol $50\,\text{mol}\%$, obtained from a $100\,\text{ps}$ trajectory. (a) Direct time-integration approach in its Green-Kubo (green, as obtained from the matrix $L^{ij}(\mathcal{T}) \propto \int_0^{\mathcal{T}} \left\langle J^i(t)J^j(0) \right\rangle dt$) and Einstein-Helfand (orange – obtained from the matrix $\left(L^{ij}\right)'(\mathcal{T}) \propto \int_0^{\mathcal{T}} \left(1 - \frac{t}{\mathcal{T}}\right) \left\langle J^i(t)J^j(0) \right\rangle dt$) formulations. The horizontal purple band indicates the value obtained by the cepstral method. (b) Estimate of κ with the cepstral method as a function of the number of cepstral coefficients, P^*, see Eqs. (5.18-5.20). The dashed vertical line indicates the value of P^* selected by the AIC, Eq. (5.27). Reproduced from Ref. [D].

in the case of a water-ethanol solution. Both the Green-Kubo and the Einstein-Helfand definitions of the finite-time expression of Onsager's coefficients (see Eq. (2.21)) are displayed. Due to thermal fluctuations, the integral of the correlation function becomes a random walk as soon as the latter vanishes, eventually assuming any value. Therefore, there will be a set of times (see Fig. 5.14) where the term L^{QQ} at the denominator in Eq. (5.37) vanishes, leading to divergences in the evaluation of κ; an issue not affecting the one-component case. Hence, in such a formulation of the multi-component case, the mean value of the thermal conductivity estimator *in the time domain* does not exist. On the contrary, the multi-component frequency-domain approach presented in this section, and built on sound statistical basis, provides a well defined expression for the estimator of κ and its statistical error.

5.3.3 Data analysis work-flow (multi-component fluids)

We summarise the steps leading to the estimation of thermal conductivity by the *cepstral analysis* method for multi-component fluids, in the same way we did in Sec. 5.2.6 for solids and one-component fluids.

1. From a MD simulation compute the heat flux time series J_n^1 and the independent particle fluxes J_n^q, $q = 2, \ldots, Q$.

2. Compute the discrete Fourier transform of the fluxes, $\tilde{J}_k^i$, and the element

$1/(\hat{S}^{-1})^{11}$. In practice, only a selected low-frequency region shall be used (see [B] for a detailed discussion).[5]

3. Calculate $\log\left[1/(\hat{S}^{-1})^{11}\right]$.

4. Compute the inverse discrete Fourier transform of the result to obtain the cepstral coefficients $\hat{C}_n$.

5. Apply the Akaike Information Criterion, Eq. (5.27), to estimate the number of cepstral coefficients to retain, P^*.

6. Finally apply Eq. (5.18) to obtain $\hat{L}_0^*$, and evaluate the thermal conductivity as

$$\kappa = \frac{\Omega}{2k_B T^2} \exp\left[\hat{L}_0^* - \psi(\ell - Q + 1) + \log(\ell - Q + 1)\right], \qquad (5.38)$$

and its statistical error as

$$\frac{\Delta\kappa}{\kappa} = \sqrt{\psi'(\ell - Q + 1)\frac{4P^* - 2}{N}}. \qquad (5.39)$$

5.4 Optimization of heat currents

In this section we exploit the gauge invariance principle, presented in Sec. 3.2, to define alternative equivalent expressions for the energy current. This procedure is particularly useful when dealing with multi-component systems where energy is the only relevant conversed quantity, such as solids where atoms do not diffuse or molecular liquids, as discussed in Sec. 3.3. These ideas reveal to be particularly useful in the analysis of *ab initio* energy flux time series, that are typically characterised by a much larger variance than classical energy fluxes. In order to illustrate the origin of this phenomenon, we consider the case of liquid heavy water that was simulated by Marcolongo et al. [31] from first-principles.

Formation energies contributions in heavy water simulations

Marcolongo et al. [31] computed the thermal conductivity of heavy water at $400\,\mathrm{K}$, a temperature that is know to predict qualitatively the self-diffusion coefficient of water at ambient conditions [142] using the PBE exchange-correlation energy functional [143]. A system of 64 heavy-water molecules was considered and sampled for $90\,\mathrm{ps}$ in the NVE ensemble at the experimental density of $1.11\,\mathrm{g\,cm^{-3}}$.

As commented in Sec. 3.3, the *ab initio* energy fluxes of molecular fluids contain non-diffusive components that, while not contributing to the conductivity, do increase the noise of the flux time series to a level that may compromise its analysis. To see where the problem comes from, let us split the potential energy of the

---

[5]To lighten the notation, we drop the left superscripts of the variables in this subsection.

system into the sum of non-interacting atomic energies plus an interaction energy, as: $V(\{\mathbf{R}_n\}) = \sum_n \epsilon_n^\circ + V_{int}(\{\mathbf{R}_n\})$, where ϵ_n° is the energy of the n-th atom when it is isolated from the rest. In classical simulations the energy of isolated atoms never enters the description of the system, and the ϵ_n°'s can be simply set to zero. In quantum simulations, instead, atomic and interaction energies enter on a same footing and the former give a large and fluctuating contribution to the total energy flux, $\mathbf{J}^\circ = \sum_X \epsilon_X^\circ \mathbf{J}^X$, where $\mathbf{J}^X$ is the number flux defined in Eq. (3.18). In a monoatomic fluid $\mathbf{J}^X$ is constant because of momentum conservation and it is actually equal to zero in the center-of-mass reference frame. In molecular fluids the $\mathbf{J}^X$ do not vanish but they are non-diffusive and hence do not contribute to the heat conductivity, while adding considerable noise to the energy-flux time series. In order to remove them, instead of estimating $\mathbf{J}^\circ$ from the non-interacting atomic energies, one can apply one of the techniques described in the following, that exploit the gauge invariance principle

Decorrelation technique

Current decorrelation builds on the Lemma 1 presented in Sec. 3.2.1. Let us now suppose that a set of fluxes $\{\mathbf{Y}^u\}$, $u = 1, \ldots U$ is known to exhibit a non-diffusive behavior. Lemma 1 shows that the auxiliary flux defined as

$$\mathbf{J}' \equiv \mathbf{J} - \sum_w \lambda^w \mathbf{Y}^w, \tag{5.40}$$

will yield the same thermal conductivity as $\mathbf{J}$. Optimal values of the $\{\lambda^u\}$ coefficients can then be determined by imposing that the new time series $\mathbf{J}'$ is uncorrelated with respect to the non-diffusive ones, *i.e.*:

$$\langle \mathbf{J}\mathbf{Y}^u \rangle - \sum_w \lambda^w \langle \mathbf{Y}^w \mathbf{Y}^u \rangle = 0, \quad u = 1, \ldots U. \tag{5.41}$$

This procedure is particularly useful when the $\mathbf{Y}^u$ fluxes give a slowly converging contribution to the Green-Kubo integral, which is thus difficult to evaluate numerically.

The decorrelation technique has been applied to heavy water considering two non-diffusive number fluxes: $\mathbf{Y}^1 = \mathbf{J}^H + \mathbf{J}^O$, *i.e.* the sum of hydrogen and oxygen average velocities,[6] and $\mathbf{Y}^2 = \mathbf{J}^{el}$, the adiabatic electronic current defined in Eq. (4.16), that is also non-diffusive. We denote by $(\mathbf{J}^1)'$ and $(\mathbf{J}^{12})'$ the currents decorrelated with respect to $\mathbf{Y}^1$ alone, and with respect to both $\mathbf{Y}^1$ and $\mathbf{Y}^2$, respectively. The power spectra of the two currents are plotted in Fig. 5.15 and feature a total spectral power that is some order of magnitude smaller than that of $\mathbf{J}$ (not shown). The low-frequency region of the spectra (up to $\sim 9.0\,\mathrm{THz}$) was used to estimate κ from cepstral analysis. The resulting thermal conductivities are $\kappa^1 = 0.80 \pm 0.12\,\mathrm{W/mK}$ for the $(\mathbf{J}^1)'$ flux, and $\kappa^{12} = 0.93 \pm 0.14\,\mathrm{W/mK}$ for $(\mathbf{J}^{12})'$, compatible with each other. By comparison, experiments give a value $\kappa \approx 0.6\,\mathrm{W/mK}$

---

[6]Note that the two time series $\mathbf{J}^H$ and $\mathbf{J}^O$ are trivially related, because of momentum conservation. Therefore $\mathbf{J}^H$, $\mathbf{J}^O$, or $\mathbf{J}^H + \mathbf{J}^O$ would all be equivalent choices.
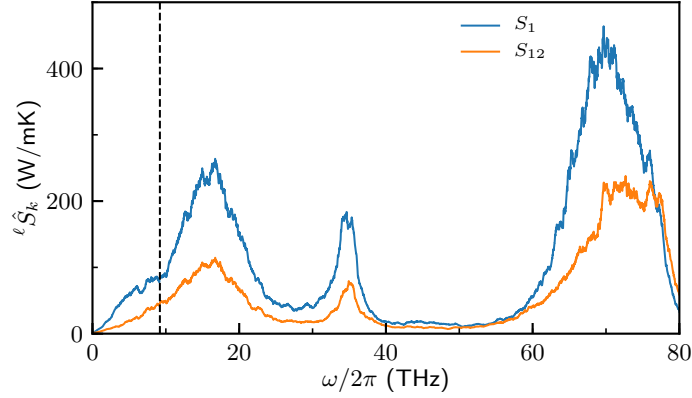
Figure 5.15: Periodogram of the $\left(\mathbf{J}^1\right)'$ and $\left(\mathbf{J}^{12}\right)'$ currents, filtered with a moving average window in order to reveal the prominent features. The vertical dashed line delimits the low-frequency region used for cepstral analysis. Adapted from Ref. [C].

[144, 145]. Let us remark that in this case, data analysis would not have yielded any meaningful results failing a proper decorrelation of the heat flux time series.

Velocity-Renormalization

An alternative "velocity-renormalization" (VR) can be applied *before* the energy flux computation by redefining the particle velocities entering the definition of the flux. Each velocity is renormalized by subtracting the velocity of the center of mass of its species from it, that is

$$\mathbf{V}_n^{\mathcal{R}}(t) = \mathbf{V}_n(t) - \frac{1}{N_X} \sum_{m \in X} \mathbf{V}_m(t), \tag{5.42}$$

where X is the species of atom n, and the sum is performed over all atoms of that species. The "renormalized" energy flux is thus defined by using the renormalized velocities and keeping the positions unchanged, *i.e.*

$$\mathbf{J}^{\mathcal{R}}\left(\{\mathbf{R}_n, \mathbf{V}_n\}; t\right) = \mathbf{J}\left(\{\mathbf{R}_n, \mathbf{V}_n^{\mathcal{R}}\}; t\right). \tag{5.43}$$

It is possible to prove that each species' center of mass velocity gives a vanishing particle current that do not contribute to the thermal conductivity in the thermodynamic limit. This techniques removes this spurious signal without affecting the thermal conductivity and possibly making the convergence faster, by decreasing the magnitude of statistical fluctuations.

5.5 Outlook

Although a large variety of methods has been formulated in the literature, none of them seems to provide a sufficiently rigorous and accurate estimator of the ther-

mal conductivity that can be applied to different classes of materials and especially to disordered systems. The cepstral analysis method introduced in this chapter promises to be a very powerful tool to estimate the thermal conductivity from relatively short MD runs, in a more rigorous way than done so far by other methods. Its implementation is straightforward and its use robust, as the only parameter to be determined is the optimal number of cepstral coefficients, using *e.g.* the Akaike's information criterion. The most impressive results are achieved for disordered systems, *e.g.* liquids and amorphous solids, where a low conductivity results from large cancellations in the integral of a highly oscillatory HCACF, for which all the traditional methods fail or give very subjective results. In these systems, simulation times of the order of 100 ps seem sufficient to obtain accuracies of the order of 10% in the estimated thermal conductivities. The performance is less spectacular in periodic crystals, where slowly-decaying strongly-harmonic phonon modes require longer simulation times and the ensuing sharp peak in the low-frequency region of the power spectrum requires a larger number of cepstral coefficients than predicted by the optimization of the AIC. Even so, simulation times of the order of a few hundred picoseconds seem sufficient to achieve a comparable accuracy. In the latter case, it is possible that a combination of the methodology introduced here with specialised techniques based on normal-mode analysis, such as that presented in Ref. [42], will result in further improvements. Leveraging more general (possibly non-Fourier) representations of the log-spectrum of the currents to be analysed, and replacing the optimization of the AIC with more sophisticated and possibly more efficient approaches, such as *e.g.* weighted multi-model inference techniques [131, 137], may also assist in this and other difficult cases. Finally, we expect that our methodology will impact on the simulation of any transport phenomena to which the Green-Kubo theory applies, such as ionic conduction, viscosity, and many others: benchmarks on these properties should be performed.

Thanks to this achievement, we are finally able to undertake the quantum simulation of heat transport in materials like liquids, highly-anharmonic crystals, and amorphous solids, that was considered impracticable due to the long trajectories usually required.

6

Thermal conductivity simulations of Silica glass

The calculation of the lattice thermal conductivity of a material using equilibrium MD simulations requires an accurate knowledge of the *interatomic interactions*, a sample of adequate *size*, and a sufficient *simulation length*. A good interatomic force field should faithfully reproduce the structural and dynamical properties of the material, as both will be important to correctly predict the thermal conductivity. An adequately large size is required to account for all the vibrational contributions to heat transport: if the system is too small, the long-wavelength modes will be neglected or severely affected, thus altering the value of thermal conductivity estimated via the GK equation. A sufficiently long simulation is needed to let the GK estimate converge within a target statistically accuracy.

The simulation of amorphous systems such as silica glass, though, presents additional challenges. The structure of an amorphous solid is a non-equilibrium configuration, with extremely long relaxation times. In order to generate it, one can perform a virtual *quenching* experiment: the system is melted at high temperature and then cooled gradually down to a target temperature, where it is then equilibrated and data can be collected. This procedure is in all respects a simulated annealing experiment looking for the most stable configuration in an extremely rough free energy landscape. The quenching protocol adopted will affect the final structural and vibrational properties of the sample, hence we expect the thermal conductivity to be affected by its details as well.

Very few studies have attempted to compute the thermal conductivity of a-SiO_2 with classical MD simulations and no *ab initio* study has ever been performed. Al-

most all of the existing simulations were carried out with non-equilibrium methods, where strong finite-size effects are accounted for with difficulty, whereas only one of them was performed at equilibrium via the GK equation. These facts demonstrate the practical difficulties involved in the numerical estimation of κ and the lack of a reliable method to do so, as we discussed in Chapter 5.

In this chapter we apply the *ab initio* GK theory and many of the methods discussed in the previous chapters to the calculation of the thermal conductivity of silica glass. In Section 6.1 we review the classical and *ab initio* studies of a-SiO$_2$ available in the literature, pointing out how the force field, the sample size, and the preparation protocol affect its structural, vibrational, and thermal properties. We find that although the structural properties are described fairly well by classical potentials, the vibrational properties are poorly accounted for and thus call for an *ab initio* approach. In Section 6.2, we use classical simulations to study the dependence of the computed thermal conductivity on many of the simulation details, such as the sample size and quenching protocol, and to determine the feasibility of *ab initio* simulations. In Section 6.3, we choose one sample of silica and we simulate it with Car-Parrinello MD at four different temperatures. The trajectories thus generated are used to compute the *ab initio* heat flux and the GK thermal conductivity, making use of many of the concepts and techniques discussed so far. Finally, we compare our classical and *ab initio* results with experiments.

6.1　State of the art

6.1.1　BKS force field

The structure of amorphous silica is made of SiO$_4$ tetrahedral units, where silicon is at the center, bonded to 4 oxygen atoms located at the vertices. Each oxygen, in turn, bridges the tetrahedral vertices, thus bonding between two silicon centers. The variation in orientation of adjacent tetrahedra makes the medium- and long-range structures disordered, forming a typical glass network.

One of the most successful and broadly adopted force fields for a-SiO$_2$ is the so-called BKS potential [106]. The BKS potential is a two-body potential devised by Beest et al. who fitted self-consistent-field Hartree-Fock calculations on small silica clusters, and it is defined as the sum of a Coulomb and a Buckingham potential:

$$v_{\alpha\beta}^{\text{BKS}}(R) = \mathrm{e}^2 \frac{q_\alpha q_\beta}{R} + A_{\alpha\beta}\mathrm{e}^{-B_{\alpha\beta}R} - \frac{C_{\alpha\beta}}{R^6}, \tag{6.1}$$

where $\alpha, \beta \in [\text{Si}, \text{O}]$, and R is the distance between the ions α and β.

Despite its simplicity, BKS was showed to predict remarkably well many properties of SiO$_2$, among which its complicated phase diagram [146]. Other force fields have been used in the literature, ranging from re-parametrizations of the BKS potential [147], to polarizable force fields (*e.g.* Tangney and Scandolo [148]) and reactive ones (*e.g.* ReaxFF [149]). Notwithstanding, the BKS potential is still the mostly

adopted force field in classical simulations of a-SiO$_2$, thanks to its ability to generate very good glass structures. In the following, and partly in Sec. 6.1.3, we are going to summarize how well the properties of amorphous silica are described by this potential and others.

Structural properties

Si-O bonds are generally considered to have partial ionic and covalent character. The BKS potential is spherical, therefore it does not describe the directional nature of the covalent bond, but it can anyway achieve the tetrahedral structure through a strictly repulsive interaction between oxygen atoms. We can expect that the bond's directionality could be better described by other more sophisticated potentials or by *ab initio* methods, yet the BKS' abilities in predicting the amorphous structure of silica glass are very remarkable. For example, Tian et al. [150] compared the structures of silica obtained from different force fields, *e.g.* BKS and ReaxFF. They quenched a fully melted silica box of density $\rho = 2.2 \, \text{g/cm}^3$ from $5000 \, \text{K}$ to $300 \, \text{K}$ at $5 \times 10^{12} \, \text{K/s}$ in the NVT ensemble. The BKS and ReaxFF potentials both generate realistic silica structures [149, 151], with radial distribution functions, neutron structure factors, and coordination numbers that reasonably reproduce the experimental observations. The radial distribution functions, in very good agreement with experiment, show a sharp peak corresponding to the Si-O bond length at $\sim 1.6 \, \text{Å}$, the peak corresponding to the O-O distance at $\sim 2.6 \, \text{Å}$, and the one corresponding to the Si-Si distance at $\sim 3.1 \, \text{Å}$. The coordination numbers can be used to detect coordination defects. By choosing a cutoff length for Si-O pairs of $\sim 2.15 \, \text{Å}$, BKS reproduces a realistic coordination environment for Si and O, with over 99.6% of atoms being normally coordinated (4-fold Si and 2-fold O). ReaxFF, instead, tends to generate more coordination defects, with $\sim 97.5\%$ of normally coordinated atoms. Nevertheless, the quenching process largely influences the macroscopic and microscopic properties of the generated glass, as we will comment diffusively later, in Sec. 6.1.3.

Vibrational properties

Besides the structure of the generated sample, the thermal conductivity of a system is mainly determined by its vibrational properties, that come from the interaction potential and can be analysed by the vibrational density of states (VDOS). Experimentally, the VDOS obtained from neutron scattering shows three significant peaks at about 400, 800, and $1100 \, \text{cm}^{-1}$, that represent the rocking, bending, and stretching modes respectively [154], as shown in Fig. 6.1(b).

Classical force fields struggle to correctly reproduce the features of the VDOS of a-SiO$_2$. In Fig. 6.1(a) we report the VDOS obtained for the BKS and ReaxFF potentials [150], compared to *ab initio* calculations [152]. The low-frequency band is dominated by O contributions and agrees well with the results of first-principles simulations and experiments, even though it wrongly elongates up to $600 \, \text{cm}^{-1}$ using the BKS potential. For this model, the modes in the $400 - 500 \, \text{cm}^{-1}$ range do not agree well with experiment, a sign suggesting that BKS struggles to reproduce correctly
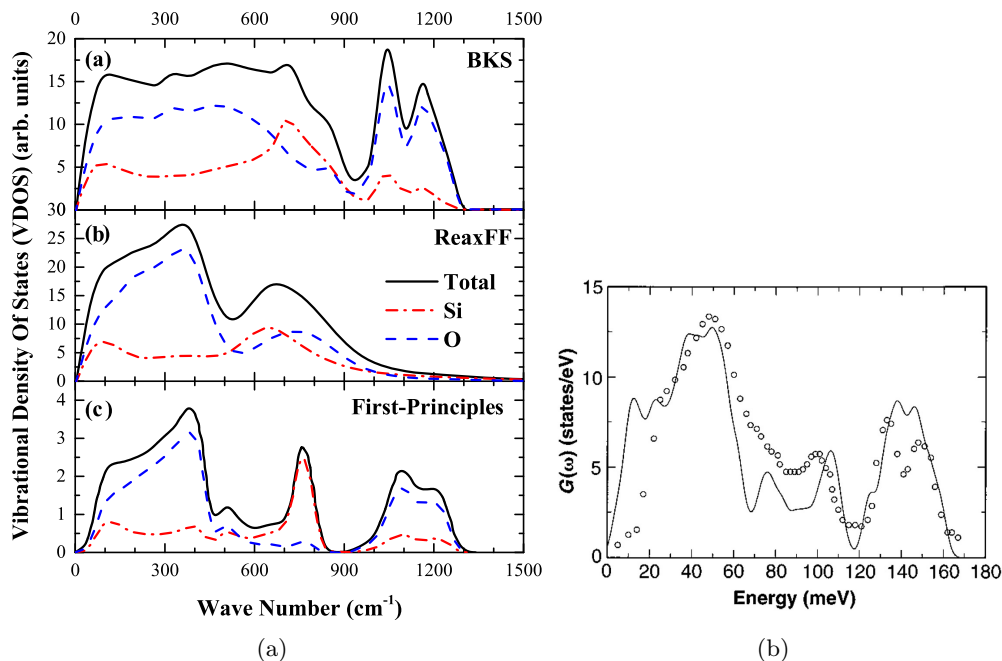
Figure 6.1: (a) Total and partial VDOS of a-SiO$_2$ computed for the BKS and ReaxFF, and compared with the first-principles results of Bhattarai and Drabold [152]. Adapted from Ref. [150]. (b) Effective VDOS of an a-SiO$_2$ sample of 72 atoms at experimental density $2.20\,\mathrm{g/cm^3}$, computed from AI-CPMD simulations within the local density approximation (solid line) and compared to neutron scattering data (circles). Reproduced from Ref. [153].

the forces over intermediate-range distances [151, 155]. The intermediate-frequency band of *ab initio* simulations is dominated by Si contributions and presents an isolated peak at about $800\,\mathrm{cm^{-1}}$, but this is not reproduced by the BKS potential, while ReaxFF does not account correctly for the contributions of Si and O atoms. The high-frequency band, that corresponds to Si-O stretching vibrations, is well reproduced by the BKS potential, but is notably missing in ReaxFF.

On the other hand, first-principles simulations have shown to successfully account for all the main peaks of the VDOS. Sarnthein et al. [153] studied a sample of 72 atoms of a-SiO$_2$ obtained by a quench from the melt with AIMD at experimental density $(2.20\,\mathrm{g/cm^3})$, within the local density approximation of DFT, and computed the VDOS by diagonalization of the dynamical matrix. Their results, reported in Fig. 6.1(b), are in very good agreement with the experiments. The same calculation has been reproduced more recently by Bhattarai and Drabold [152] using a 648-atom model of a-SiO$_2$ (see Fig. 6.1(a)).

The vibrational excitations of silica include very localized modes and collective ones (most modes with frequencies below $700\,\mathrm{cm^{-1}}$ have a collective nature, while the ones at higher frequencies are more localized). Compared to the *ab initio* description, the BKS does not reproduce well the nature of modes in the intermediate frequency range [155]. Since the BKS model was designed to optimize the elastic

constants of a small silica cluster and a crystal, it is not very surprising that it performs well at very high and low frequencies, but it is not reliable in the intermediate range. Therefore we can expect that ReaxFF would provide more realistic predictions of thermal conductivity at room temperature, where thermal conduction is mainly contributed by acoustic-like phonon vibrations whose frequencies are typically below $400\,\mathrm{cm}^{-1}$ [152], whereas the BKS potential will probably be more suitable to study high-temperatures cases, where the contribution of stretching vibrations to thermal conduction increases significantly [150].

Thermal conductivity

Many studies of the thermal conductivity of a-SiO$_2$ are based on NEMD simulations, that are strongly size dependent due to the scattering of phonons with the heat sink, and thus require the study of its convergence at large cell sizes. For example, Tian et al. [150] simulated a-SiO$_2$ with the BKS potential at $T = 300\,\mathrm{K}$, $\rho = 2.2\,\mathrm{g/cm}^3$, and obtained a value of thermal conductivity of $\kappa = (2.27 \pm 0.06)\,\mathrm{W/mK}$ at the maximum size simulated, whereas Coquil et al. [156] obtained $\kappa = (2.10 \pm 0.10)\,\mathrm{W/mK}$, to be compared with an experimental value of $\kappa_{\mathrm{exp}} \approx 1.3 - 1.4\,\mathrm{W/mK}$.

An extrapolation technique is needed to estimate the convergence of κ as a function of the size of the simulation cell in the direction of the applied heat flux (or temperature gradient), L_z. According to the kinetic theory: $\kappa = \frac{1}{3}c_v v_s\, l$, where c_v is the lattice specific heat at constant volume, v_s is the sound velocity, and l is the mean-free path of the phonons. The thermal conductivity can be obtained by linear fitting $1/\kappa$ vs $1/L_z$ and extrapolating the value at $1/L_z = 0$ [57]. Despite being broadly applied in the literature, this method has to be used with extreme care. Indeed, if the distribution of phonon mean-free paths cannot be approximated by its average value, the linear dependence of $1/\kappa$ on $1/L_z$ is no longer valid, as higher-order terms are not negligible, as Sellan et al. [88] ascertained studying Ar and Si crystals. If the considered system sizes are smaller than the largest bulk mean-free paths that dominate thermal transport, then the linear relationship may not work and the thermal conductivity can be severely underestimated. In the case of amorphous silica, the maximum phonon mean-free path is quite short (between ~ 20 and $\sim 6\,\mathrm{\AA}$, depending on temperature [157]), a fact that may explain why Tian et al. [150] find the linear fit to work well in this case, allowing them to extrapolate a value of $\kappa = 2.5\,\mathrm{W/mK}$ for the BKS and Teter potentials, and of $1.28\,\mathrm{W/mK}$ for the ReaxFF potential, at $300\,\mathrm{K}$. Therefore, the ReaxFF potential seems to best reproduce the experimental value at this temperature.

To the best of our knowledge, only one numerical study has ever been performed using EMD, likely due to high difficulty of estimating the thermal conductivity from the GK equation, as we discussed in Sec. 5.1. McGaughey and Kaviany [111] estimated the thermal conductivity of a system of 576 atoms ($\rho = 2.35\,\mathrm{g/cm}^3$ at $T = 50 - 400\,\mathrm{K}$), obtaining a thermal conductivity of $\approx 2\,\mathrm{W/mK}$ at $300\,\mathrm{K}$. The GK method is much less affected by finite-size effects, and can simulate the bulk from much smaller systems with respect to NEMD. However, tests for the convergence of κ with the cell size should always be performed, as discussed in the following.

6.1.2 Sample size

In contrast to crystals, glasses have a completely disordered and non-periodic structure, therefore we should understand what is the minimum sample size that one can simulate to ensure that the distribution of structures at the various relevant length scales is well represented. This is of particular importance in view of performing AIMD simulations, in which the computationally affordable sizes are of the order of a few hundreds of atoms at most. Previous studies have tried to survey this limit.

Structural properties

Few studies have been performed using *ab initio* techniques and all involved a small sample of ~ 70 atoms (~ 25 SiO$_2$ units). In the first *ab initio* simulation of a-SiO$_2$, Sarnthein et al. [158] performed a quench from the melt completely by CPMD, obtaining a first model of vitreous silica. Even though good agreement with experiments was found for some structural, vibrational and electronic properties [153, 158, 159], a very fast quenching rate (of the order of 10^{15} K/s) was used, due to the high computational cost, that may have strongly influenced the results. In Sec. 6.1.3 we will debate more this issue. Some years later, Benoit et al. [160] combined classical MD with CPMD: samples generated with the BKS potential (with a quenching rate $\sim 10^{13}$ K/s) were then equilibrated in CPMD. It was shown that the structural properties thus obtained were weakly modified with respect to the classical calculations, thus validating the structural model generated with the BKS potential. Besides, these results were even in better agreement with experiments than previous studies performed completely in CPMD, which was probably due to the slower quenching employed. Other five years later, Van Ginhoven et al. [161] studied a set of small silica samples of 72 atoms generated by the BKS potential and optimized by DFT, and showed that by creating multiple small samples it is possible to achieve a good statistical sampling of structural features consistent with larger simulated glass systems. An ensemble of small samples is necessary to capture the statistical distribution of structures of silica glass, *i.e.* all the possible arrangements of its medium-range features.

Thermal conductivity

In spite of the reliability of BKS with regard to structural properties, as mentioned in the previous section, the vibrational properties reproduced by this classical force field are strongly modified by using an *ab initio* treatment of the forces [155], therefore we do not expect it to be reliable in this respect. Furthermore, it is not yet clear how much the thermal conductivity is affected by the size of the sample. Even if we average over a set of small samples, it is possible that finite-size effects may be relevant and influence the value of κ we compute, that thus would require larger size cells to converge. Therefore, a preliminary study on this point should be performed before attempting an *ab initio* computation of the thermal conductivity of a-SiO$_2$. We will present the results of this study in Sec. 6.2.2.
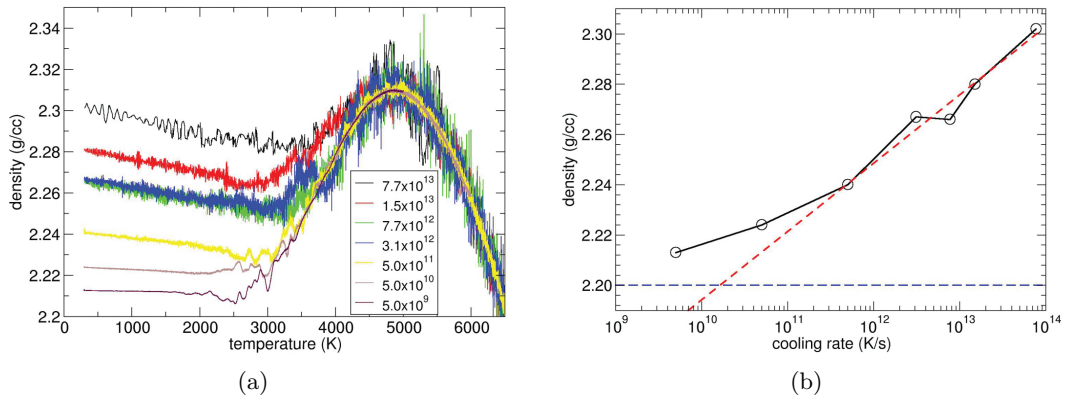
Figure 6.2: (a) Density vs temperature of a-SiO$_2$, modeled with the BKS potential, for seven quenches completed with linear cooling rates γ from 8000 K to 300 K. Silica's density anomaly is visible at high temperatures; density becomes independent of γ at $T \gtrsim 4500$ K. (b) Density at 300 K as a function of the quench cooling rate γ. The horizontal dashed line is the experimental value. The red dashed line is a linear extrapolation fit to data above 3×10^{12} K/s. Reproduced from Ref. [162]

6.1.3 Sample preparation (quenching)

The properties of the simulated glass may depend considerably on the quenching protocol adopted to generate the virtual sample. When the relaxation times of a supercooled liquid exceed the time scale of the (virtual) experiment, the system will be in a non-equilibrium state and undergo a glass transition, provided it does not crystallize. The thus obtained glass is a nonequilibrium structure whose properties will generally depend on its production history. The *quenching rate* at which it was cooled will determine its macroscopic and microscopic properties [151]. For example, the glass transition temperature computed by simulations is significantly higher than the glass transition temperature observed in the laboratory. The time scales reachable by computer simulations are many orders of magnitude shorter than the typical time scales of laboratory experiments, hence the minimum quenching rates attainable in classical MD simulations are of the order of $10^{11} - 10^{13}$ K/s, a rate that can only be replicated experimentally by strong laser pulses or ion bombardment [16].

Macroscopic properties

Vollmayr et al. [151] studied extensively the effects of quenching rate on the properties of BKS amorphous silica. They used a sample of ~ 1000 atoms at zero pressure, melted at 7000 K and then cooled down to 0 K at different temperature rates γ, ranging from 10^{12} to 10^{15} K/s. More recently, Lane [162] extended their study, reaching cooling rates down to 5×10^9 K/s with microsecond MD simulations of ~ 13000 atoms.

The glass transition temperature, that they estimated from the enthalpy curves, increases with γ. As one can expect, fast cooling rates make the system fall out

of equilibrium more quickly during the quench. The density ρ of the final sample also depends on the quenching rate: at temperatures below $2000 - 3000$ K, higher γ determine higher densities, as can be observed in Fig. 6.2, that seem to approach the experimental value of 2.202 g/cm^3. Between 10^{14} K/s and 10^9 K/s density decreases of less than 5%. This behaviour is unusual: in most glasses density increases as cooling rates are slowed down. This can be explained by observing the trend at higher temperatures, where the density reaches a maximum at $T \sim 4800$ K that does not depend on γ: this "density anomaly" is also observed in experiments, at a much lower temperature of 1820 K. This discrepancy can be attributed to the BKS potential. Furthermore, the thermal expansion coefficient at constant pressure, $\alpha_p = \frac{1}{V} \left. \frac{\partial V}{\partial T} \right|_p = -\frac{1}{\rho} \left. \frac{\partial \rho}{\partial T} \right|_p$, increases with γ.

Structural properties

The structure is even more affected by the quenching rate. By analysing the radial distribution function (RDF) between different species it is possible to observe that a low cooling rate makes the structural order at short and intermediate distances increase, *i.e.* the RDF peaks and minima are sharpened and the structure is more relaxed. However, the location of the RDF's peaks is very little affected by γ (*i.e.* the Si-O tetrahedra do not change much their size with γ) and compares quite well with experiment, thus making BKS a good potential to reproduce the short- and medium-range structure of a-SiO$_2$. Since the size of Si-O tetrahedra does not change much their size with γ, the variation of density with the changes in the cooling rate is due to relative arrangement of neighboring tetrahedra. This can be observed in variations of the distributions of angles and rings. The O-Si-O angle distribution sharpens by decreasing γ and approaches the ideal tetrahedron angle of 109.47°; the Si-O-Si angle distribution, instead, does not sharpen but shifts to larger angle values, indicating a more open arrangement of tetrahedra, which is consistent with the observed lower density; 6-vertex rings become more frequent with decreasing γ, indicating that the local structure of the system approaches the one of β-crystobalite. The study of coordination numbers of each atom type shows that local order increases fast with decreasing cooling rate: for example, the number of Si atoms that are 4-fold coordinated with O atoms increases from 95% to 99.5% by decreasing the cooling rate from 10^{15} K/s to 10^{13} K/s, and even further at 10^{10} K/s, indicating a gradually decreasing number of coordination defects.

Vibrational properties

The two high-frequency peaks of VDOS depend on the quenching rate in that their height increases significantly with decreasing γ, hence improving the agreement with experiment. The low- and mid-frequency bands obtained with the BKS, are quite featureless and do not change very much with γ, thus remaining quite in discordance with experimental results.

To our knowledge, a study of the dependence of the thermal conductivity of a-SiO$_2$ on the quenching rate has never been performed, and should be completed
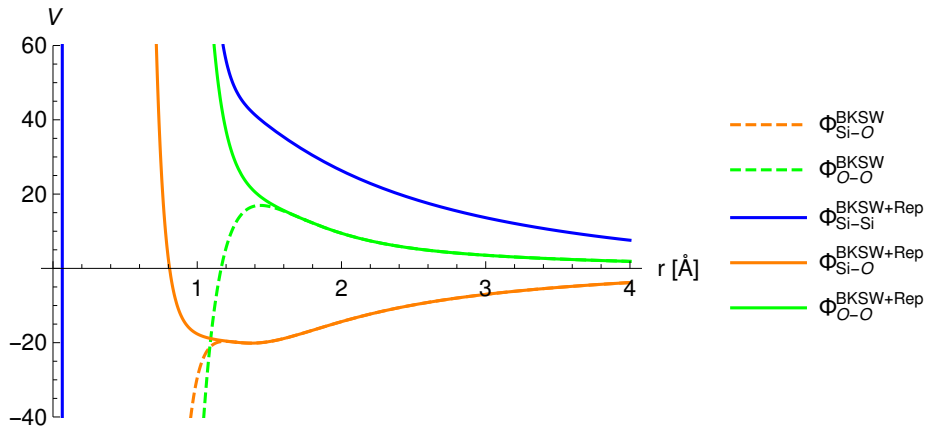
Figure 6.3: Dashed lines: BKS potential with Wolf truncation, as defined in Eq. (6.2). Solid lines: the same with a repulsive core added, defined in Eq. (6.5).

before attempting a first-principles calculation. In Sec. 6.2.2 we will present this study.

In conclusion, even though these studies have been performed using the BKS potential and not with DFT (for obvious computational reasons), it is very reasonable to assume that their results will also hold for AIMD simulations of amorphous silica. The demonstrated capabilities of the BKS potential in structure prediction and the very large range of time scales analysed leads us to conclude that a reliable a-SiO$_2$ structure can only be obtained by a "slow" quenching protocol with classical MD. AIMD simulations can then be used to optimize the structure, generate a trajectory and, finally, a heat current time series ready to be analysed.

6.2 Classical preliminaries

6.2.1 Force field

We performed classical MD simulations of amorphous silica using the LAMMPS package [56]. We used a modified version of the BKS potential [147], in which the long-range Coulomb interaction is truncated with the Wolf method [163–165], thus avoiding the use of Ewald summations [81, 82]. This truncation is possible thanks to Coulomb screening effects, and it only needs the addition of a correction term that recovers the requirement of charge neutrality. The final form we used is the one of Ref. [107]:

$$v_{\alpha\beta}^{\mathrm{BKS}}(R) = q_\alpha q_\beta e^2 V_W(R) G_W(R) +$$
$$\left[A_{\alpha\beta} e^{-\frac{R}{\rho_{\alpha\beta}}} - \frac{C_{\alpha\beta}}{R^6} - \left(A_{\alpha\beta} e^{-\frac{R_{c,\mathrm{sh}}}{\rho_{\alpha\beta}}} - \frac{C_{\alpha\beta}}{R_{c,\mathrm{sh}}^6} \right) \right] G_{\mathrm{sh}}(R), \quad (6.2)$$

α-β	$A_{\alpha\beta}$ (eV)	$\rho_{\alpha\beta}$ (Å)	$C_{\alpha\beta}$ (eVÅ^6)	$D_{\alpha\beta}$ (eVÅ^{12})
O-O	1388.773	0.3623	175.0	142.209126863
Si-O	18003.7572	0.2052	133.5381	1.434274208
Si-Si	872360308.1	0.0657	23.299907	0.0

α-β	$E_{\alpha\beta}$ (eVÅ^{-1})	$F_{\alpha\beta}$ (eV)	r_{inf} (Å)
O-O	-14.9704268	39.035745917	1.75
Si-O	-3.2771769	-15.797166326	1.27
Si-Si	0.0	0.0	0.0

Table 6.1: Parameters of the BKS potential used in classical MD simulations, defined in Eq. (6.2) and (6.5).

with

$$V_W(R) = \left(\frac{1}{R} - \frac{1}{R_c}\right) + \frac{1}{R_c^2}\left(R - R_c\right), \tag{6.3}$$

$$G_W(R) = \exp\left(-\frac{\gamma_W^2}{(R - R_{c,W})^2}\right), \quad G_{\mathrm{sh}}(R) = \exp\left(-\frac{\gamma_{\mathrm{sh}}^2}{(R - R_{c,\mathrm{sh}})^2}\right), \tag{6.4}$$

$q_{\mathrm{Si}} = 2.4$, $q_{\mathrm{O}} = -1.2$, $\gamma_W = \gamma_{\mathrm{sh}} = 0.5$, $R_{c,W} = 10.17\,\text{Å}$, and $R_{c,\mathrm{sh}} = 5.5\,\text{Å}$. This potential, whose form is depicted in Fig. 6.3, was shown to give results comparable to the original BKS formula [147]. Since the potential becomes attractive at very short distances, its short-range part at $R < R_{\mathrm{inf}}$ has been substituted by a repulsive core, in order to prevent atoms from getting too close to each other: a problem that may arise at high temperatures during melting. The form of this repulsive part is:

$$V_{\alpha\beta}^{\mathrm{rep}}(R < R_{\mathrm{inf}}) = \frac{D_{\alpha\beta}}{R^{12}} + E_{\alpha\beta}R + F_{\alpha\beta}, \tag{6.5}$$

that we designed such that the potential and its first and second derivatives are continuous, as depicted in Fig. 6.3. The parameters of the potential are reported in Table 6.1.

Simulation protocol

We started the simulation from a 72-atom sample of β-cristobalite, corresponding to 24 SiO$_2$ units, that we eventually replicated to obtain larger cubic supercells at the experimental density of a-SiO$_2$, $\rho = 2.202\,\mathrm{g/cm^3}$. Each system was melted and equilibrated at constant temperature 7000 K for more than $t_{\mathrm{melt}} = 500\,\mathrm{ps}$ in the NVT ensemble, using the Bussi-Donadio-Parrinello stochastic velocity-rescaling thermostat [166] with a coupling time constant $\tau_{\mathrm{NVT}} = 200\,\mathrm{fs}$. The equations of motion were integrated using the velocity Verlet algorithm with a time step of $\epsilon_{\mathrm{MD}} = 1\,\mathrm{fs}$. Subsequently, the temperature was decreased linearly in a time t_{quench} down to $T_{\mathrm{eq}} = 500\,\mathrm{K}$, in the NVT ensemble, thus resulting in a quenching rate of $\gamma = \frac{6500\,\mathrm{K}}{t_{\mathrm{quench}}}$. The effects of different quenching rates will be studied in Sec. 6.2.2. The system was equilibrated at T_{eq} in the NVT ensemble for other 400 ps, and finally in

the microcanonical (NVE) ensemble for 100 ps. At this point, we started to collect data for at least $t_{\mathrm{run}} = 1$ ns.

The computational cost of these classical simulations is very low, so it was possible to run different replicas of each system from different initial conditions, thus providing us with abundant statistics. The thermal conductivity was estimated from $t_{\mathrm{run}} = 1$ ns of trajectory for each sample, using the *cepstral analysis* method presented in Sec. 5.2.

6.2.2 Sample preparation: size and quenching rate dependence of κ

In order to study the convergence of lattice thermal conductivity with the size of the system and the quenching rate, we considered cells containing 72, 144, 288, 432, 576, 864, 1152, 2304, 5184, and 10800 atoms. For each cell size we analysed the data obtained from 10 independent replicas with different initial conditions. For each replica, we considered 10 different quenching times: $t_{\mathrm{quench}} = 5$, 10, 25, 50, 100, 250, 500 ps, 1, 5, and 10 ns, that correspond to quenching rates γ ranging from 1.3×10^{15} to 6.5×10^{11} K/s. We computed the thermal conductivity κ of each of these samples, from a trajectory of $t_{\mathrm{run}} = 1$ ns, using *cepstral analysis*. More technical details on this procedures are reported in Sec. 5.2.

In Fig. 6.4 we plot the thermal conductivity as a function of the number of atoms of the system N_{at}, for the ten quenching rates considered. The κ measured for each replica is depicted with a circle. For each N_{at} and γ, we computed a weighted average over the replicas' results (depicted with a solid line) using the errors estimated from cepstral analysis as weights. We can infer that κ is underestimated by the smallest systems considered, and seems to converge to a stable value for $N_{at} \gtrsim 500$ atoms. This is likely due to two effects, both entering this analysis. The first is the fact that small replicas cannot account for the whole ensemble of possible amorphous structures. In particular, the variety of medium- and long-range structures needs larger systems to be correctly accounted for. However, as we mentioned in Sec. 6.1.2, some authors found that averaging over a little set of small structures ($N_{at} = 72$) should be enough to reproduce fairly well the range of glass-network structures found in larger cells [161]. Nevertheless, the smallest systems lead to an underestimate of κ by more than 20%. We can probably attribute this behaviour to a second effect, affecting the vibrational modes: the finite-size of the system dictates an upper limit to the wavelength that can be accommodated into the simulation cell, and alters the the low and medium vibrational frequencies, which are largely attributed to the collective modes of silica. The Green-Kubo equation thus requires a sufficiently large volume to correctly account for all the contributions. We should however point out that this value is remarkably lower (approximately ten times lower) than the typical cell volumes required by NEMD calculations.

In Fig. 6.5, the same data are plotted as a function of the quenching rate $\gamma = \frac{6500\,\mathrm{K}}{t_{\mathrm{quench}}}$, for each of the sizes considered. Slower quenching rates (longer quenching times, of the order of a few nanoseconds) definitely lead to higher thermal conductivities. This is not very surprising: as we discussed in Sec. 6.1.3, a slower quenching allows the system to relax more and to build glass structures with higher

local order, less defects, and structural features that are in better agreement with experiments. Therefore, a quenching rate $\gamma \lesssim 10^{13}$ K/s seems to be the requirement for almost all the simulated sizes.

In Fig. 6.4 and 6.5 the error on the weighted average is indicated as a thin shaded area surrounding the solid line. Two other lines are reported. The dashed lines delimit the average error that we expect to obtain from a single trajectory sample of $t_{\text{run}} = 1$ ns (it is about the error on the weighted averaged times $\sqrt{10}$). We observe that in general the single calculations of κ (10 replicas for each abscissa, represented by single circles), fall mostly inside this error bars, for the medium and large systems. For the smaller systems, the fluctuations of the single values become larger, probably due to larger differences in their structures, in addition to the intrinsically larger fluctuations due to the smaller size. The trend of the relative error estimated for a 1 ns trajectory as a function of the number of atoms is shown in Fig. 6.6(a), for 4 selected quenching rates, and seems to decrease as $\sim 1/\sqrt{N_{\text{nat}}}$. The quenching rate, instead, does not appear to affect the error on κ, as shown in Fig. 6.6(b).

From this analysis we conclude that system size and cooling rate considerably affect the thermal conductivity of BKS silica glass. In order to perform an *ab initio* study of the thermal conductivity, we need to select a sample size that can be simulated with AIMD at a reasonable computational cost. We decided to use one of the samples with $N_{\text{at}} = 432$ atoms that were generated using the smallest cooling rate analysed, $\gamma = 6.5 \times 10^{11}$ K/s, corresponding to a quenching time of 10 ns. In the following we dub this sample $\mathbb{S}_1$. We first made sure that $\mathbb{S}_1$ did not exhibit any coordination defects, then we computed its thermal conductivity, that results to be $\kappa_{\mathbb{S}_1} = (2.207 \pm 0.045)$ W/mK, using a 1 ns-long trajectory. This value differs from the average values obtained for the largest systems analyzed by less than 5% (≈ 0.1 W/mK). Further data analysis showed that an error of the order of 12% (≈ 0.25 W/mK) could be obtained from a trajectory of 100 ps, a simulation length reasonably affordable with CPMD, hence making this bias in the thermal conductivity negligible.

6.2.3 Cepstral analysis

The thermal conductivity of each classical replica of silica was computed with the cepstral analysis technique described in Sec. 5.2. The P^* cutoff was chosen using the Akaike Information Criterion (see Sec. 5.2.4) without any correction factor, because in Sec. 5.2.7 we showed that this was not necessary for the case of classical a-SiO$_2$. The heat flux calculated by LAMMPS at each time step (1 fs) was filtered with a moving average and resampled at a rate of one step every 18 fs, corresponding to a cutoff frequency $f^* \approx 28$ THz. The resulting spectrum was analyzed using our ThermoCesptrum code [133]. In the following we perform an additional analysis on the dependence of the thermal conductivity of the $\mathbb{S}_1$ sample on some of the parameters.

We first study the value of the thermal conductivity estimator as a function of the cutoff frequency f^* and the length of the trajectory. In Fig. 6.7(a-c) we report the

t_{run}	standard-HC	VR-HC	$\langle P^* \rangle$
100 ps	2.19 ± 0.25 (12%)	2.17 ± 0.27 (12%)	$47 - 36$
1 ns	2.18 ± 0.15 (9.5%)	2.18 ± 0.20 (9.2%)	$176 - 154$
10 ns	2.24 ± 0.08 (3.5%)	2.25 ± 0.07 (3.3%)	$448 - 377$

Table 6.2: Estimated statistical error on the thermal conductivity of sample $\mathbb{S}_1$ for a trajectory length t_{run}. "Standard-HC" and "VR-HC" refer to the standard definition of the heat current and the equivalent definition with renormalized atomic velocities, respectively. The last column contains the average number of cepstral coefficients retained using the standard and VR heat current, respectively.

average κ obtained for a 100 ps, 1 ns, and 10 ns trajectory, respectively. In general, all the f^* in the middle region give compatible results, with more instabilities arising at the lowest frequency values (likely due to increasing aliasing effects that alter the spectrum), that indeed show an increased error and and should be avoided in this case. These fluctuations decrease in longer trajectories, as the statistical error obviously decreases. Besides, a too high f^* ($f^* \gtrsim 60\,\mathrm{THz}$, not shown) induces a bias in κ, due to the fact the log-periodogram diverges to negative values and we start to have problems of numerical accuracy. A 100 ps trajectory ultimately gives compatible results with the 10 ns one, as reported in Table 6.2. Incidentally, we also notice that the error on κ estimated by cepstral analysis decays slower than expected with the length of the trajectory. Indeed the error should decrease as the inverse of the trajectory length (see Eq. (5.20)), but from 100 ps to 1 ns it decreases of a factor $\approx \frac{1}{\sqrt{3}}$, and a factor $\approx \frac{1}{\sqrt{10}}$ from 100 ps to 10 ns. This effect can be explained by the increased number of cepstral coefficients retained by the AIC, that tries to reproduce the finest features of the spectrum with greater precision.

We also analyzed a "decorrelated" heat current, obtained by the velocity-renormalization (VR) method described in Sec. 5.4. As shown in Fig. 6.7(d), this method reduces the power of the spectrum by a large amount, removing part of the signal at finite frequencies that does not contribute to the thermal conductivity, without affecting the low-frequency region, hence the value at zero frequency. This procedure is very useful to reduce the variance of the energy current signal obtained from *ab initio* simulations, however here it does not change much the results, nor the statistical error in a significant way, as reported in Table 6.2. The number of cepstral coefficients P^* is reduced as the spectrum is smoother, but the error ultimately increases if we use a low f^*, due to the fact that the optimal P^* becomes too low.

6.2.4 Density dependence of κ

The dependence of κ of a-SiO$_2$ on the pressure can be safely neglected for the range of temperatures considered later ($300 - 1500\,\mathrm{K}$). Silica glass has a anomalously low thermal expansion coefficient, with an experimental value of $\alpha = \frac{1}{V}\left(\frac{\partial V}{\partial T}\right)_T \approx 5.5 \times 10^{-7}\,\mathrm{K}^{-1}$ at $300\,\mathrm{K}$, about 20 times smaller than that of crystalline forms of

silica. The relative variation in density from $300\,\mathrm{K}$ to $1500\,\mathrm{K}$ can be estimated to be $\frac{\Delta\rho}{\rho} \approx 7{\times}10^{-4}$. Using the experimental bulk modulus $K = -V\frac{dP}{dV} = \rho\frac{dP}{d\rho} \approx 36.7\,\mathrm{GPa}$ and experimental density at $300\,\mathrm{K}$, $\rho = 2.202\,\mathrm{g/cm}^3$, we can expect a consequent variation in pressure of about $\Delta P \approx 30\,\mathrm{MPa}$, quite negligible. Experimental measures of thermal conductivity of silica at high pressures estimate a variation of κ with pressure of the order of $5\%/\mathrm{GPa}$ [167], hence we can safely neglect this effect.

In classical simulations these values may change slightly, but we do not expect significant differences. In the preliminary phases of this work we also performed quenching simulations at constant pressure, in the NPT ensemble. We found, in accordance with previous studies discussed in Sec. 6.1.3, that the density of the sample increases with the quenching rate. A slow quenching leads to lower densities, closer to the experiment. The average equilibrium density obtained from the slowest quench at zero pressure is equal to $\rho_{P=0} = 2.31\,\mathrm{g/cm}^3$, slightly larger than the experimental one. We can attribute this discrepancy to a combined effect of the BKS potential and of the fast quenching rate. The thermal expansion coefficient is 5 times larger than experiment, with a value of $\alpha \approx 2.8 \times 10^{-6}\,\mathrm{K}^{-1}$. Finally, the thermal conductivities obtained from quenches in the NPT ensemble show values that are up to 10% larger than those obtained by quenches at fixed volume, for the fastest quenching rates and smallest sizes, and of similar values for the slowest rates (plots obtained from the NPT simulations are reported in Appendix B). The slightly higher densities (up to $\approx 2.5\,\mathrm{g/cm}^3$) that are obtained by using very fast quenching rates are probably the reason of this difference. We decide therefore to set the density at the experimental value and to equilibrate our simulations in the NVT ensemble, as previously done by many authors.
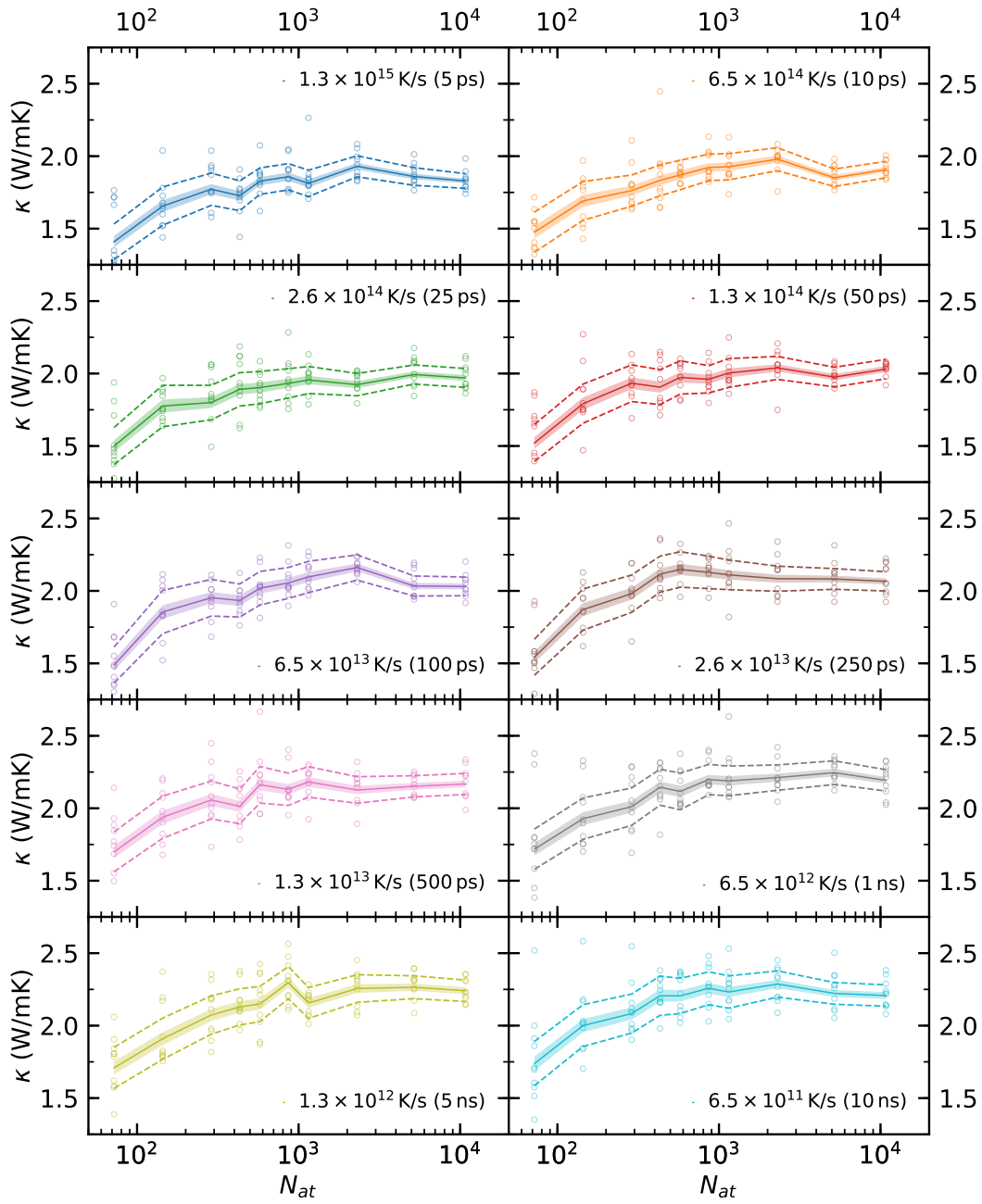
Figure 6.4: Study of convergence of the thermal conductivity of a-SiO$_2$ at 500 K with the size of the system, estimated from classical simulations, as described in Sec. 6.2.2. The abscissa indicates the number of atoms of the system, each panel corresponds to a different quenching rate γ (the relative quenching time t_{quench} is indicated in brackets). Circles are the results of 10 independent replicas simulated with the same quenching protocol. The solid line is a weighted average computed over the replicas and weighted using the errors estimated from cepstral analysis. Three different error limits are indicated. Dashed area: standard deviation of the weighted mean. Dashed lines: statistical error estimated for a *single* 1 ns-trajectory.
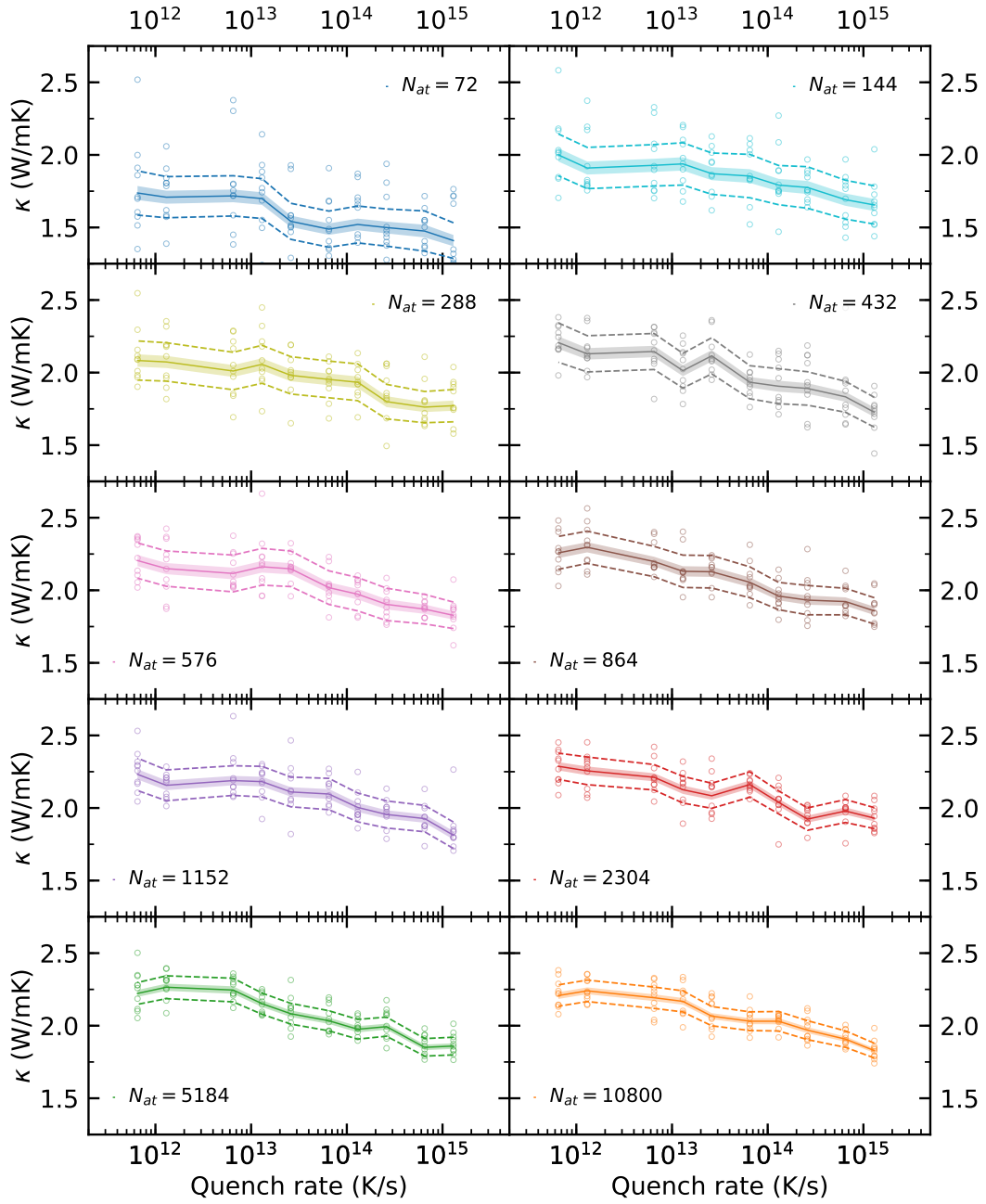
Figure 6.5: Study of convergence of the thermal conductivity of a-SiO$_2$ at 500 K with the cooling quenching rate γ, estimated from classical simulations, as described in Sec. 6.2.2. Each panel corresponds to a different system size with N_{at} atoms. Circles are the results of 10 independent replicas simulated with the same quenching protocol. The solid line is a weighted average computed over the replicas and weighted using the errors estimated from cepstral analysis. Three different error limits are indicated. Dashed area: standard deviation of the weighted mean. Dashed lines: statistical error estimated for a *single* trajectory of 1 ns.
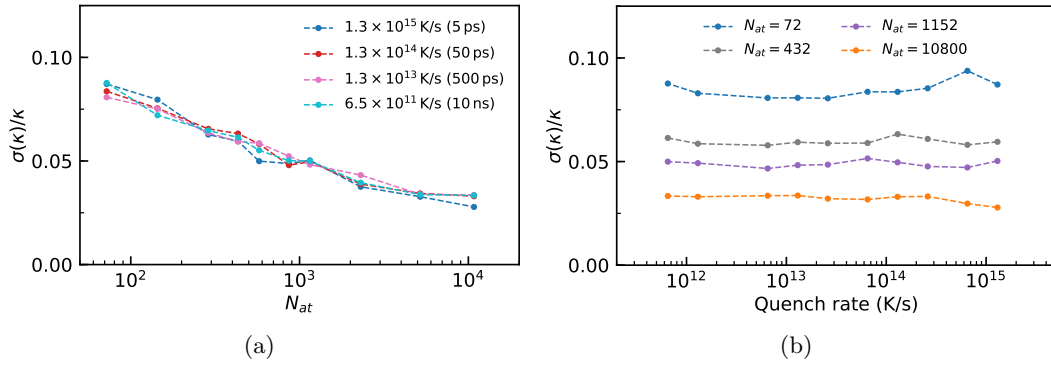
Figure 6.6: Estimated relative error on the thermal conductivity of a-SiO$_2$ for a 1 ns trajectory (dashed lines) as a function of (a) the number of atoms, (b) the cooling quenching rate.
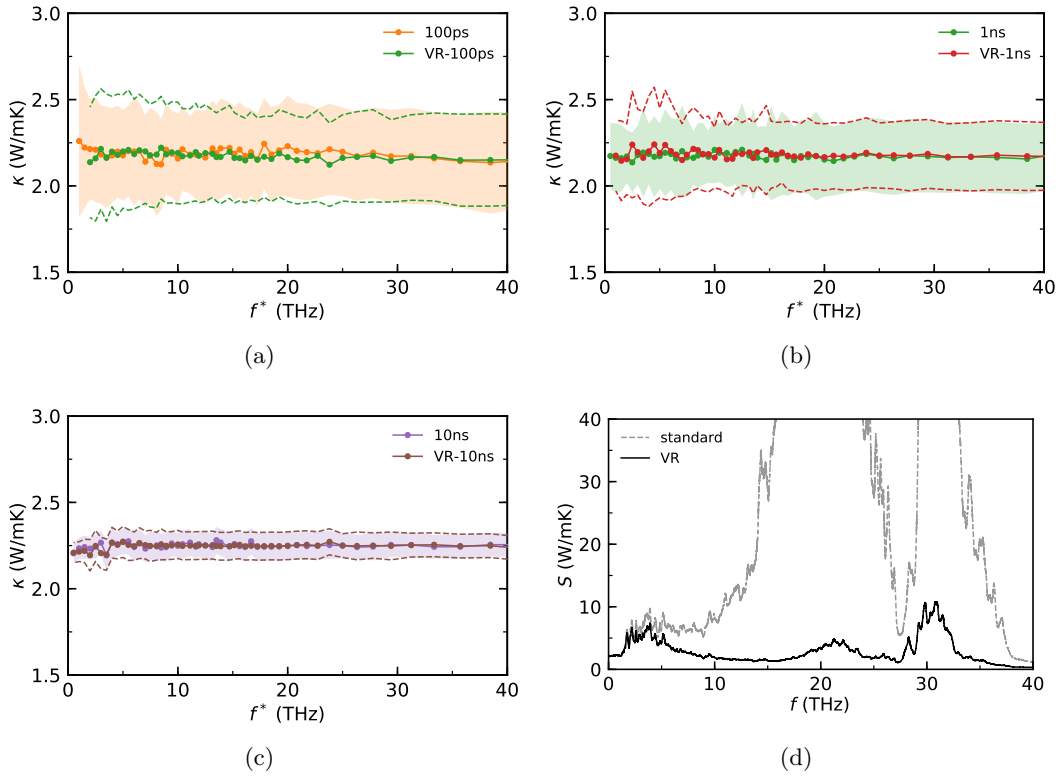
Figure 6.7: Dependence of κ on the choice of the cutoff frequency f^*, estimated from *one* sample of (a) 100 ps, (b) 1 ns, and (c) 10 ps of the "original" and VR heat flux time series; (d) periodograms of the original and the VR heat flux time series.

6.3   Quantum simulations: results

The $\mathbb{S}_1$ sample has been simulated with Car-Parrinello MD using the `cp.x` code of the QUANTUM ESPRESSO suite [95, 97]. We used the PBE-GGA exchange-correlation functional [143], wave functions were expanded in plane waves with a kinetic-energy cutoff of 70 Ry and using the optimized norm-conserving Vanderbilt pseudopotentials (ONCVP) [168, 169]. The cutoff was chosen so that energies and forces were converged. The system contained 432 atoms (144 Si, 288 O) and 2304 electrons. A time step of $\epsilon_{CP} = 15$ a.u. ≈ 0.36 fs and a fictitious electron mass of 400 a.u. were used to integrate the equations of motion. We verified that the kinetic energy of the fictitious electronic degrees of freedom and the total energies were not drifting during the whole length of the simulation. The system was thermalised for about 5 ps at temperature T_{eq} in the NVT ensemble using the Nosé-Hoover thermostat [170, 171], then it was let evolved in the microcanonical ensemble for about $t_{run} \approx 52$ ps. No atomic diffusion or significant structural modifications were observed during the whole *ab initio* MD runs.

Four different equilibrium temperatures T_{eq} were simulated: 300, 500, 1000, and 1500 K. For each temperature we actually ran two independent simultaneous simulations with different initial conditions, thus obtaining a total of ≈ 105 ps worth of data at each temperature, in half the wall time. Each of the CPMD calculations costed about 140 k CPU hours.

6.3.1   Heat current calculation

For each AIMD trajectory generated, we proceeded to the computation of the *ab initio* heat current, following the procedure described in Sec. 4.2.2. The first important parameter to fix is the heat current sampling rate. For this system, we estimated that one single-step calculation of the current costs roughly 60 CPU hours, so one can easily estimate the potential cost of a 100 ps trajectory.

Heat current sampling rate

In fact, the time period ϵ_{HC} over which we compute the current determines the Nyqvist frequency of its power spectrum, f_{Ny}, *i.e.* the maximum frequency reproducible (see Sec. 5.2.5), therefore we have to make sure that the maximum frequency of the power spectrum is smaller than f_{Ny}. Of course, the longer ϵ_{HC}, the smaller the number of steps we will need to compute. An educated guess can be made from classical MD simulations. By examining the power spectrum of the classical heat current, we estimated that a sampling period $\epsilon_{HC} = 30\epsilon_{CP} \approx 10.88$ fs would give a reasonably low $f_{Ny} \approx 45$ THz. If we resample the classical time series at different sampling rates, without applying any preliminary filter, we observe the effects of aliasing on the power spectrum. After some trials, we verified that sampling rates leading to a decrease of spectral power ΔP (the integral of the power spectrum) of less than 1% do not appreciably introduce aliasing effects that may alter the low-frequencies of the spectrum, hence the value of thermal conductivity.
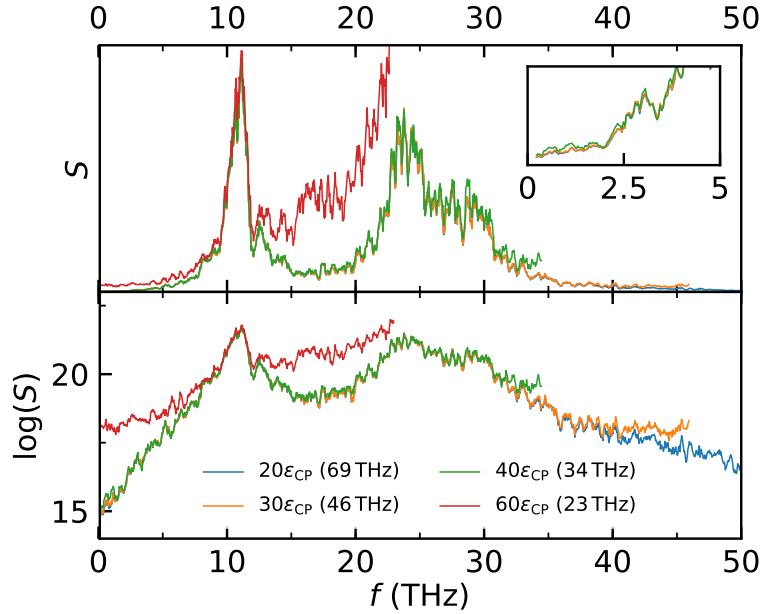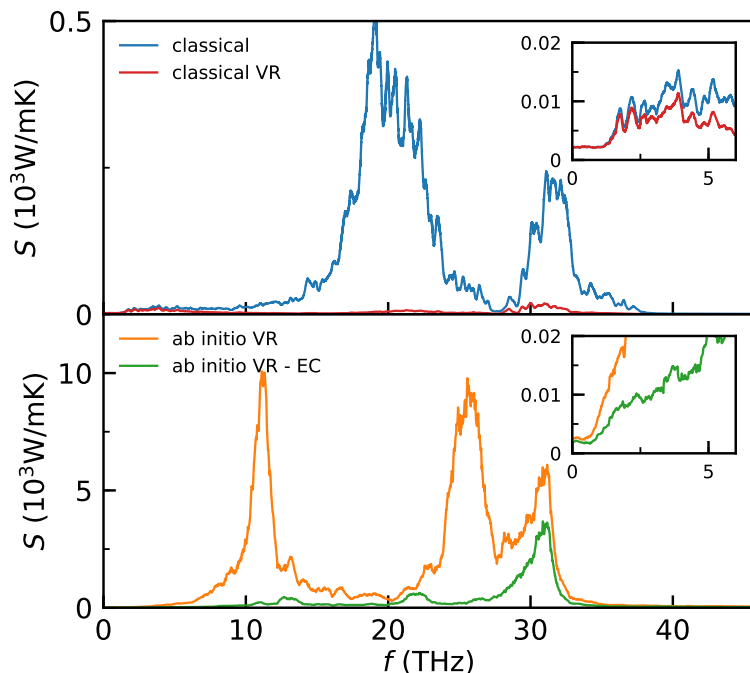
Figure 6.8: Power spectral density of the *ab initio* heat current of sample $\mathbb{S}_1$ (upper panel) and its logarithm (lower panel), computed from a short trajectory at 1500 K at different sampling periods (the resulting f_{Ny} are reported in parenthesis). Inset: zoom of the low-frequency region of the spectrum.

A value $f_{\mathrm{Ny}} \approx 40\,\mathrm{THz}$ ($\Delta\mathrm{P} \approx 0.9\%$) does not change the estimated κ; choosing $f_{\mathrm{Ny}} \approx 35\,\mathrm{THz}$, instead, cuts a tail of the spectrum ($\Delta\mathrm{P} \approx 4\%$) and introduces important aliasing effects that ultimately change its value at zero-frequency, so it should not be used.

Notwithstanding these considerations, past experience with other systems suggests us that the *ab initio* heat current often possess a larger variance than the classical one, (see Sec. 5.4) hence a larger spectral power, that may invalidate the empirical tests just performed. To verify that this was not the case, we decided to compute the *ab initio* heat current of a short trajectory at every 20 CP time steps ($\epsilon_{\mathrm{HC}} = 20\epsilon_{\mathrm{CP}} \approx 7.26\,\mathrm{fs}$), and compare the results obtainable from different sampling periods: $\epsilon_{\mathrm{HC}} = 20\epsilon_{\mathrm{CP}}$, $30\epsilon_{\mathrm{CP}}$, $40\epsilon_{\mathrm{CP}}$, and $60\epsilon_{\mathrm{CP}}$. The corresponding periodograms are plotted in Fig. 6.8. The two largest sampling periods, $40\epsilon_{\mathrm{CP}}$ and $60\epsilon_{\mathrm{CP}}$, clearly display remarkable aliasing effects, that affect the low- and middle-frequency region of the spectrum, an effect not present if we choose $30\epsilon_{\mathrm{CP}}$. Therefore, we decided to set $\epsilon_{\mathrm{HC}} = 30\epsilon_{\mathrm{CP}}$. For a trajectory of 100 ps, we need to perform about 9500 heat current calculations, with a total estimated cost of the order of 560 k CPU hours.

Heat current power spectrum

As we just mentioned, the *ab initio* heat current time series has a variance much larger than the classical one, thus making the peaks of its power spectrum much higher, and its analysis possibly more difficult. This effect is due to the different definition of the microscopic energy density in the classical and DFT approach, and

Figure 6.9: Power spectral density of the heat current of $\mathbb{S}_1$ at $300\,\mathrm{K}$. Upper panel: classical current (blue) and the same with renormalized velocities. Lower panel: *ab initio* current with renormalized velocities (orange) and the same decorrelated from the electronic current (green).

its different ripartition between atoms. Similarly to what happens in a molecular system like water (see Sec. 3.3), the average distance between atoms in a solid is a bounded vector if atomic diffusion does not occur, so we can expect a flux $\mathbf{J}^{\mathrm{SiO}} = \mathbf{J}^{\mathrm{Si}} - \mathbf{J}^{\mathrm{O}}$, where $\mathbf{J}^{\mathrm{Si}}$ and $\mathbf{J}^{\mathrm{O}}$ are the number fluxes defined in Eq. (3.18), to be a total time derivative of a bounded vector field. By the gauge invariance theorem, we conclude that this flux does not contribute to the thermal conductivity and can therefore be removed with one of the techniques presented in Sec. 5.4.

We decided to apply the velocity-renormalization (VR) decorrelation technique before computing the heat current: the value of each atom's velocity (extracted from the CPMD trajectory) was renormalized by subtracting the velocity of the center of mass of its species from it. For example, at each time t the velocity of a silicon atom $\mathbf{V}_n(t)$ was substituted with $\mathbf{V}_n(t) - \frac{1}{N_{\mathrm{Si}}} \sum_{m \in \mathrm{Si}} \mathbf{V}_m(t)$, where N_{Si} is the total number of silicon atoms. Furthermore, as discussed in Sec. 4.2.1, the electronic current (EC) $\mathbf{J}^{el}$ is also non-diffusive and can therefore be removed, for example by a simple decorrelation procedure applied after the heat current computation.

The power spectra of the classical and the *ab initio* heat currents are displayed in Fig. 6.9. One can immediately notice the large difference in power of the classical and *ab initio* spectra (see units), and the effects of the VR and EC-decorrelation, that make the spectrum flatter. This effect does not change much the low-frequency region, in the classical case, but it does in the quantum case, even though the
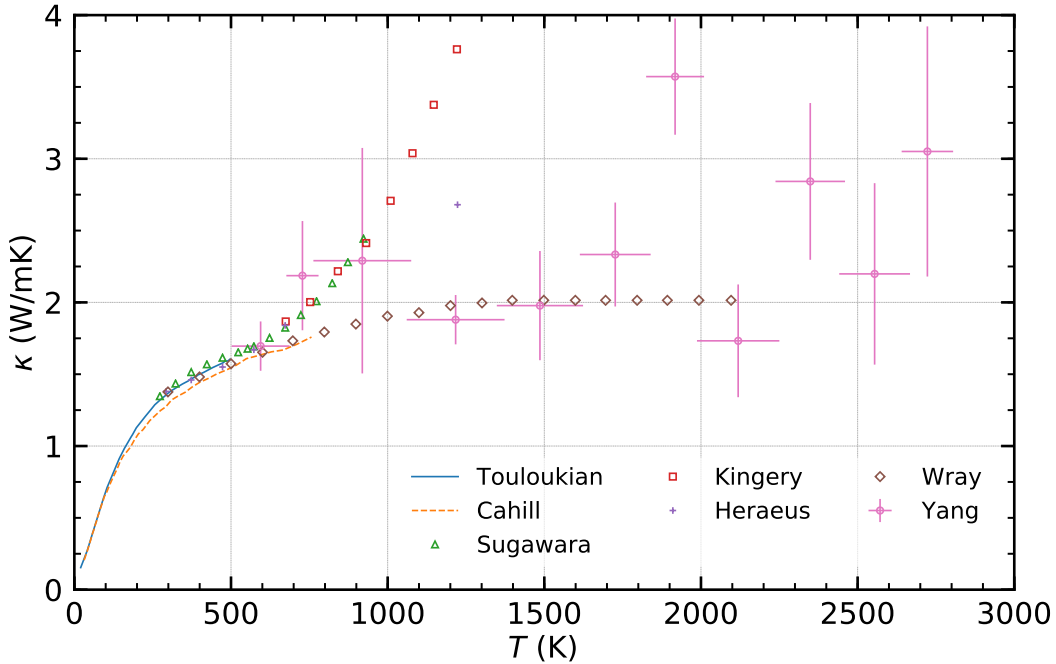
Figure 6.10: Experimental measurements of the thermal conductivity of a-SiO$_2$ as a function of the temperature. Data from Touloukian et al. [172], Cahill [173], Sugawara [174], Kingery [175], Wray and Connolly [176], Yang et al. [177], and data from a glass manufacturer [178].

convergence at zero-frequency is maintained. We also notice that the positions of the peaks of the *ab initio* power spectrum are shifted with respect to the classical case, a consequence of the different VDOS of these two systems.

6.3.2 Temperature dependence of κ

We now study the thermal conductivity of silica as a function of the temperature and compare it with experimental data.

Experimental data

The first experimental measurements of the thermal conductivity of a-SiO$_2$ as a function of temperature were carried out between the 50's and 70's by Kingery [175], Wray and Connolly [176], Sugawara [174], and Touloukian et al. [172]; a few more recent studies are the ones of Cahill [173] and Yang et al. [177]. We display all these experimental results in Fig. 6.10, which shows substantial agreement between all of them at low temperatures, but two different trends at temperatures larger than 600 K. Above 600 K radiative heat transport becomes very intense (scaling roughly as $\sim T^{3 \div 4}$) and can alter the measured value of κ, that can be overestimated. This problem is of special importance in vitreous silica because this substance is highly transparent [173, 179, 180]. Cahill [173] and Wray and Connolly [176] accounted
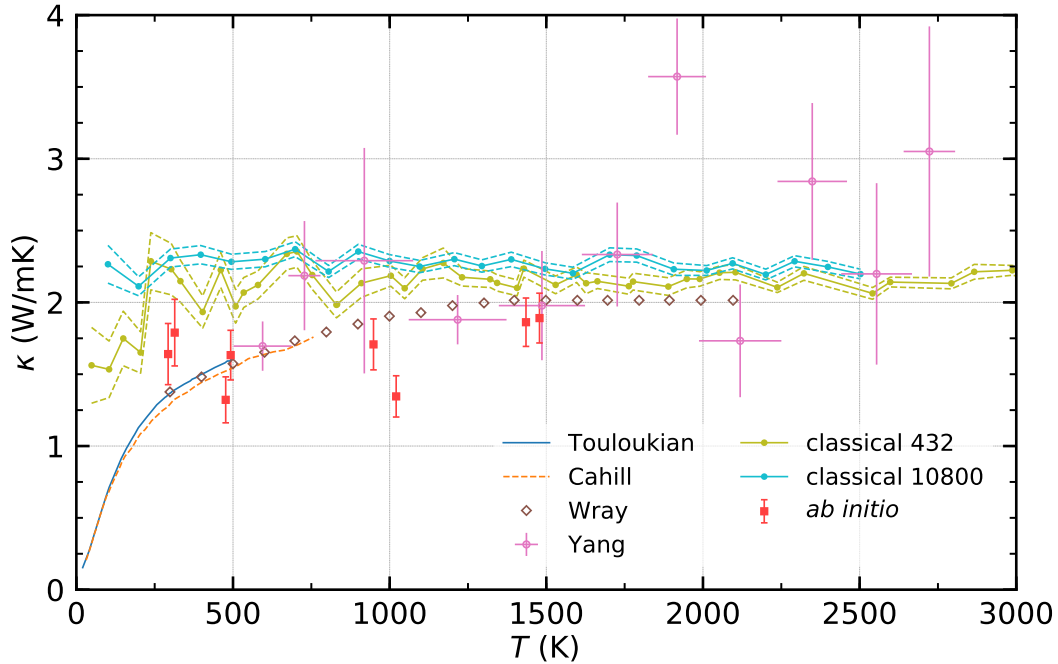
Figure 6.11: Thermal conductivity of a-SiO$_2$ as function of temperature: comparison between experiments and simulations. Only the experimental studies that accounted for radiative heat transport have been reported. Classical simulations were carried out using the BKS potential for the $\mathbb{S}_1$ sample (432 atoms), and a larger sample (10800 atoms). *Ab initio* results were computed using the $\mathbb{S}_1$ sample, as described in Sec. 6.3, by analysing the VR-EC decorrelated energy flux.

empirically for the radiative effects, thus resulting in a κ approaching the value $\kappa \approx 2\,\mathrm{K/mK}$ for temperatures up to $2000\,\mathrm{K}$. The recent measures of Yang et al. [177] performed with CO_2 laser heating, instead, did not appear to feature significant radiative contributions. Nevertheless, the matter is still under active debate [181], so at this time no clear experimental values of κ are available in this regime. This state of affairs motivates even more an accurate atomistic study to determine the thermal conductivity of a-SiO$_2$ at high temperatures.

Computational results

In Fig. 6.11 we display the results of our *ab initio* thermal conductivity simulations, compared with the results of classical simulations for the same 432-atoms sample $\mathbb{S}_1$ and a larger sample with 10800 atoms, and with experimental data.

The *ab initio* thermal conductivities for the eight independent simulations were obtained by analysing the VR-EC decorrelated energy fluxes defined in Sec. 6.3.1, with $f^* = f_{\mathrm{Ny}}$. No preliminary filtering and resampling were performed on the time series before cepstral analysis, because the estimated thermal conductivity displayed an unusual dependence on the details of the filtering procedure. We attribute this

$\mathbf{T}$ (K)	$\kappa \left(\frac{\mathrm{W}}{\mathrm{m\,K}}\right)$
303	1.71 ± 0.16
485	1.47 ± 0.12
985	1.49 ± 0.11
1460	1.88 ± 0.12

Table 6.3: Average thermal conductivities of a-SiO$_2$ computed from AIMD simulations of the $\mathbb{S}_1$ sample. Each value is a weighted average of the values obtained from two independent $\approx 52\,\mathrm{ps}$ MD simulations.

difficulty to the relatively large spectral power of the *ab initio* energy flux, compared to the classical one. Additional in-depth studies on this matter should be performed.

Nevertheless, the values obtained seem in fairly good agreement with the available experimental data, at all the temperatures analysed. The thermal conductivities at $\sim 300\,\mathrm{K}$ are larger than the experimental value $\kappa_{\mathrm{exp}} \approx 1.3 - 1.4\,\mathrm{W/mK}$ of about $0.3\,\mathrm{K/mK}$. The values between 500 and 1500 K roughly follow the experimental trent of Cahill [173], with slightly lower values at 1000 and 1500 K, even though the magnitude of the theoretical and experimental errors do not allow us to draw definitive conclusions. In Table 6.3 we report the weighted averages of the *ab initio* results performed at the same target temperature.

The classical results, obtained using the BKS potential, show a substantially constant value $\kappa \approx 2.1 - 2.2\,\mathrm{W/mK}$, that becomes compatible with experiments only at high temperatures. We can attribute the poor agreement at low temperatures to the altered vibrational properties described by the BKS potential, as we discussed in Sec. 6.1.1. Furthermore, we notice that a system of 432 atoms seems to underestimate the thermal conductivity of $\sim 5\%$ with respect to a sample with 10800 atoms, as we estimated in Sec. 6.2.2. It is possible that similar finite-size effects have affected the results of the *ab initio* simulations as well, even though we cannot verify this hypothesis without simulating larger cells.

In conclusion, our *ab initio* results, while requiring some further analysis and validation, are very promising and call for a systematic extension to other thermodynamic conditions.

7

Conclusions

In this thesis we applied for the first time the *ab initio* Green-Kubo theory to compute the lattice thermal conductivity of silica glass. To undertake this goal, we first needed to overcome two main hurdles that have hindered a first-principles application of the GK theory in the past.

The first was a conceptual problem due to the microscopic indeterminacy of the energy density, that makes the heat current ill-defined at the atomic level. We revealed the spurious nature of this problem by discovering a gauge invariance principle for heat transport coefficients, which ensures that the thermal conductivity, that is the actual measurable quantity, is well-defined and can be computed from classical and *ab initio* MD simulations. As a plus, this principle also offers us some freedom in the definition of the energy flux, enabling one to choose an expression that can optimize its statistical properties without affecting the computed value of thermal conductivity. We presented this idea and showed how it can be applied to molecular fluids and solids, where it is possible to identify fluxes that do not contribute to κ and can therefore be removed by a decorrelation technique.

The great potential of the gauge invariance principle is currently being further investigated, trying to understand in what measure the heat flux time series can be manipulated to obtain better statistical properties. If a minimum variance limit exists and can be determined, one may wonder if a physical interpretation can be inferred out of it. As we already mentioned, the GK method is able to estimate the thermal conductivity of any material in a straightforward way and without approximations, but it comes at the price of a more difficult physical interpretation. Methods based on a normal-modes decomposition [182] may reveal to be a better approach if one wishes to identify the most relevant vibrational modes contributing to κ and to understand their atomistic nature. Of course, to be effective such approaches should be able to describe non-periodic systems.

The second problem concerned the practical computation of the thermal conductivity from the GK equation, which was known to require impractically long MD simulations and lacked a solid technique for its estimation. We were able to devise a new data-analysis method based on the cepstral analysis of time-series and on sound statistical basis, that is able to provide an asymptotically consistent and unbiased estimator of κ from a single MD trajectory of limited length. We benchmarked this method on different classes of materials and found it especially suitable to study disordered systems, such as liquids and glasses, where any other traditional method fails.

Data analysis of *ab initio* heat currents revealed to be much tougher than one would expect from classical simulations. The larger statistical fluctuations, due to

the different energy density definitions, make the power spectra harder to analyse. We believe that further development should be pursued in understanding the effects of the basis set, filters and window functions used in the cepstral analysis technique, especially when a low sampling rate is used to keep the computational cost as low as possible. Multi-resolution methods, aimed to achieve a proportional accuracy from low to high frequencies, may also bring good improvements.

Equipped with these tools, we tackled the challenge of simulating silica glass (a-SiO$_2$). The simulation of amorphous materials requires additional care compared to crystalline solids. Their structure is a non-equilibrium state that sensibly depends on the preparation history. By means of classical MD simulations, we studied the effects that the sample preparation and its size have on the computed thermal conductivity. We found that quenching rates as slow as 10^{13} K/s and a few hundred atoms are needed to ensure a convergence of κ within 5%. The widely used two-body BKS force field is able to predict the structural properties of a-SiO$_2$ remarkably well, but lacks a proper accounting for its vibrational properties, thus rendering a κ that is too high at low and intermediate temperatures. Finally, we chose one classical sample of a-SiO$_2$ of 432 atoms and we simulated it with AIMD to compute its thermal conductivity by first-principles. The results are fairly in agreement with the available experimental data, that however are very imprecise at $T \gtrsim 600$ K, a regime where radiative effects become very strong and are difficult to be accounted for.

We believe that the final outcomes of this study will be particularly important to model the damage processes of laser pulses in optical glasses, and will also represent a starting point to simulating more complex glasses for a variety of applications. Although our results look encouraging, an *ab initio* study of heat transport of silica glass and amorphous materials in general will require some further refinement work. In addition, it would be particularly interesting to study more deeply the dependence of the thermal conductivity of a-SiO$_2$ and silicate glasses on suitably defined structural indicators, in order to identify its potential dependence on *e.g.* the fraction of defects, the statistics of rings, the chemical composition, etc.

In spite of the accuracy of AIMD methods, we believe that a significant boost in our future prediction capabilities will come from the design of advanced force fields, possibly based on fits of first-principles data or on modern neural networks. Recent developments in this field give us hope that it will soon be possible to design neural-networks force fields that render accurate structural and vibrational properties, and thus accurate thermal conductivities, hence reducing the cost of simulations and giving us the tools to tackle more complex systems, for a wide range of fundamental and technological applications.

A

Classical definitions of energy flux in solids

In this appendix we demonstrate the equivalence between two formulations of the classical energy current in solids, Eqs. (2.36) and (2.45), by using the gauge invariance principle presented in Sec. 3.2.

Let us consider the general formula of the energy flux for classical force fields, Eq. (2.36), and rewrite it in the following way:

$$\mathbf{J}_A^E(\Gamma) = \frac{1}{\Omega} \sum_n \left(\mathbf{J}_c^E + \mathbf{J}_v^E\right)$$
$$= \frac{1}{\Omega} \sum_n \left(\dot{\mathbf{R}}_n \epsilon_n + \mathbf{R}_n \dot{\epsilon}_n\right), \tag{A.1}$$

where $\mathbf{J}_c^E$ and $\mathbf{J}_v^E$ are the "convective" and "virial" components of the energy flux, as defined in Eqs. (2.38-2.39). In solids, the definition of Eq. (2.45) can be adopted, that can be rewritten as:

$$\mathbf{J}_B^E(\Gamma) = \frac{1}{\Omega} \sum_{n,m} \mathbf{R}_n^0 \dot{\epsilon}_n, \tag{A.2}$$

where $\mathbf{R}_n = \mathbf{R}_n^0 + \mathbf{u}_n$, $\mathbf{R}_n^0$ denotes the average atomic position of atom n, and $\mathbf{u}_n$ its instantaneous displacement. According to the gauge invariance theorem (p. 24), in order to ensure that $\mathbf{J}_B^E(\Gamma)$ is equivalent to $\mathbf{J}_A^E(\Gamma)$, that is it yields the same thermal conductivity, we just need to prove that their difference is *non-diffusive*, *i.e.* it is a total time derivative of a bounded vector. After a few manipulations we have:

$$\mathbf{J}_A^E(\Gamma) - \mathbf{J}_B^E(\Gamma) = \frac{1}{\Omega} \sum_n \left(\dot{\mathbf{R}}_n \epsilon_n + \mathbf{R}_n \dot{\epsilon}_n - \mathbf{R}_n^0 \dot{\epsilon}_n\right)$$
$$= \frac{1}{\Omega} \sum_n \left(\dot{\mathbf{u}}_n \epsilon_n + \mathbf{u}_n \dot{\epsilon}_n\right)$$
$$= \frac{1}{\Omega} \frac{d}{dt} \sum_n \dot{\mathbf{u}}_n \epsilon_n, \tag{A.3}$$

where we used the fact that $\dot{\mathbf{R}}_n = \dot{\mathbf{u}}_n$. The sum $\sum_n \dot{\mathbf{u}}_n \epsilon_n$ is a function of the phase-space that is well-defined in PBC, and it is a bounded quantity, in a solid where atomic diffusion does not occur. Therefore we can conclude that $\mathbf{J}_B^E(\Gamma)$ and $\mathbf{J}_A^E(\Gamma)$ result in the same thermal conductivity.

The same cannot be concluded for the sole "virial" term $\mathbf{J}_v^E$, for which we have

that:

$$\mathbf{J}_A^E(\Gamma) - \mathbf{J}_v^E(\Gamma) = \frac{1}{\Omega} \sum_n \dot{\mathbf{R}}_n \epsilon_n$$

$$= \frac{1}{\Omega} \sum_n \dot{\mathbf{u}}_n \epsilon_n$$

$$= \mathbf{J}_A^E(\Gamma) - \mathbf{J}_B^E(\Gamma) - \frac{1}{\Omega} \sum_n \mathbf{u}_n \dot{\epsilon}_n. \qquad (A.4)$$

The last two lines are not manifestly expressible as a total time derivative of a bounded vector, therefore the "convective" term $\mathbf{J}_c^E$ cannot be neglected *a priori* in a solid. The magnitude of its contribution (and that of the cross-correlations $\langle \mathbf{J}_c^E(t) \cdot \mathbf{J}_v^E(0) \rangle$) should be verified on a case-by-case basis, as commented in Sec. 2.3.1.
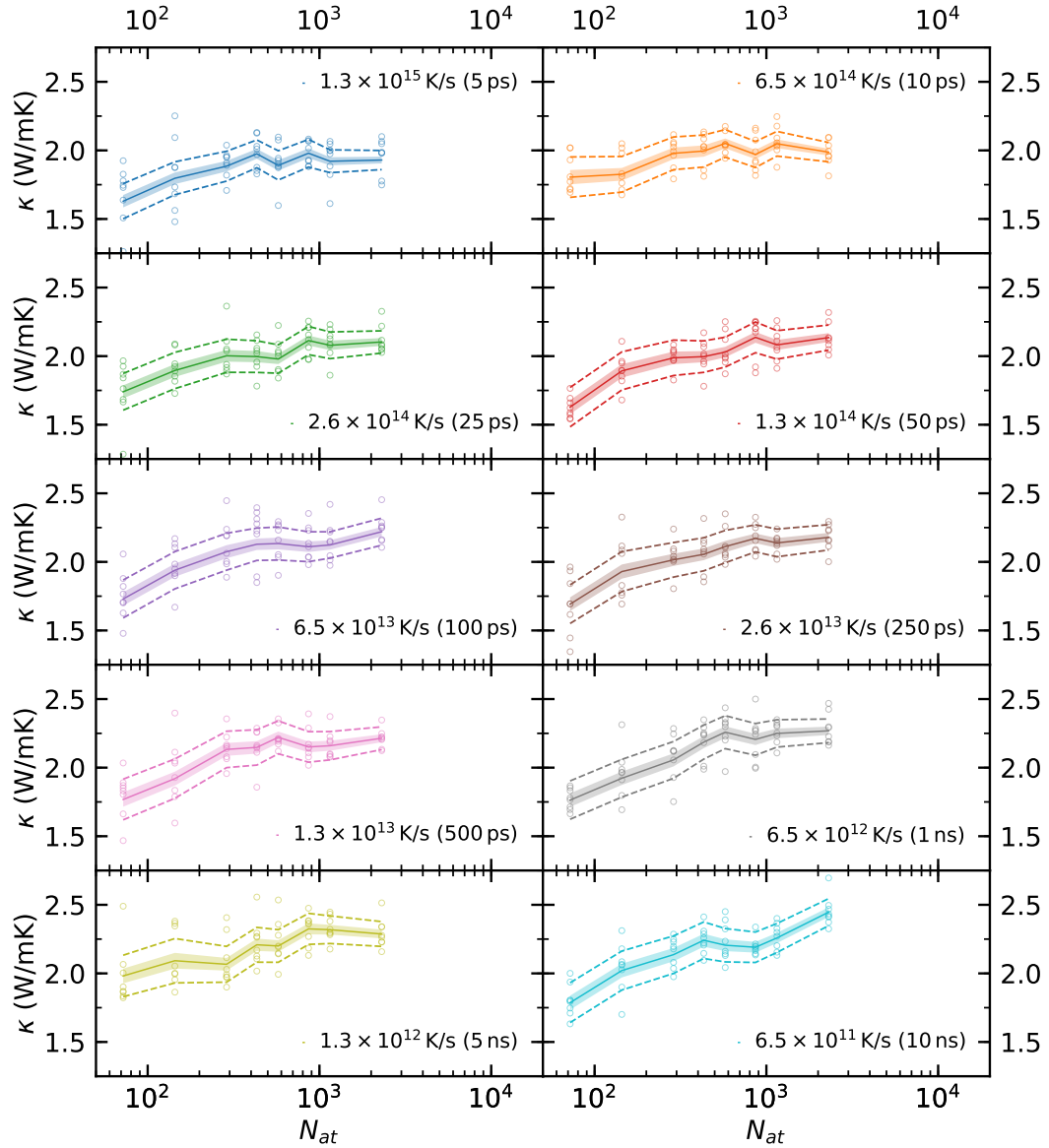
B

Silica – NPT quench results
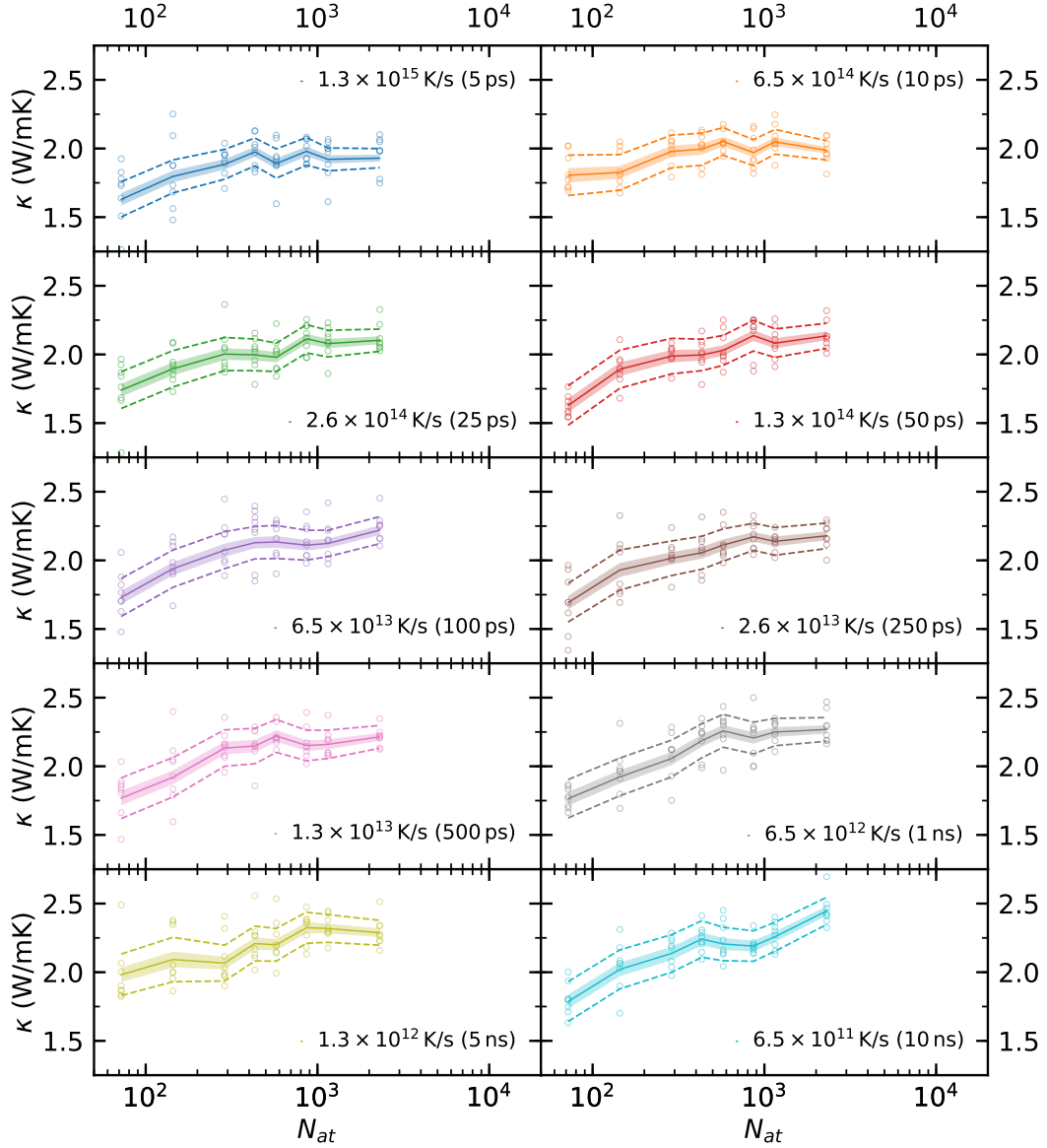
Figure B.1: Thermal conductivity of a-SiO$_2$ at 500 K obtained by a quench in the NPT ensemble at zero-pressure and with cooling rate γ. The abscissa indicate the number of atoms of the system, each panel corresponds to a different quenching rate γ (the relative quenching time t_{quench} is indicated in brackets). The same symbols as Fig. 6.4 are used.

Figure B.2: Thermal conductivity of a-SiO$_2$ at 500 K obtained by a quench in the NPT ensemble at zero-pressure and with cooling rate γ. Each panel corresponds to a different system size with N_{at} atoms. The same symbols as Fig. 6.5 are used.
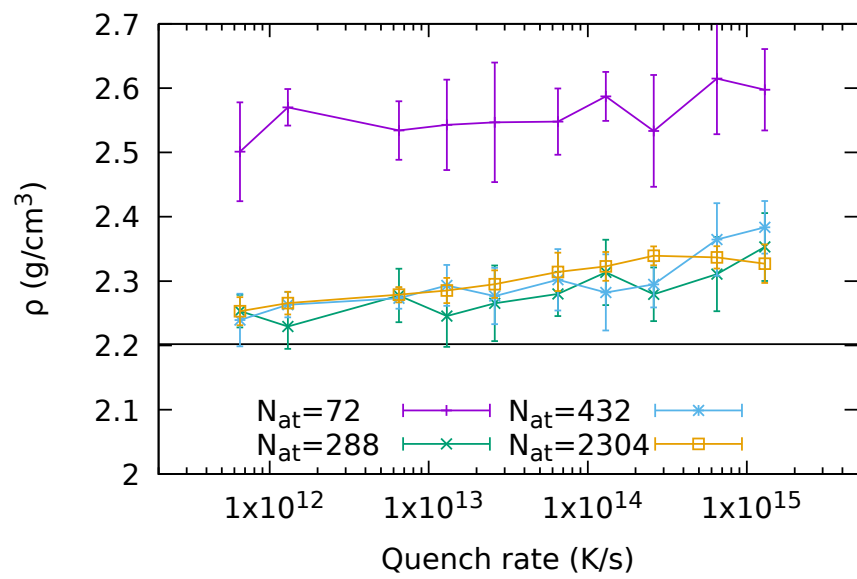
Figure B.3: Average density of a sample of N_{at} atoms at $500\,K$, obtained from a quench in the NPT ensemble at zero-pressure as a function of the quenching rate. The black line indicates the experimental value $\rho = 2.202\,g/cm^3$.

Bibliography

[A] L. Ercole, A. Marcolongo, P. Umari, and S. Baroni, "Gauge invariance of thermal transport coefficients", J. Low Temp. Phys. **185**, 79 (2016) `10.1007/s10909-016-1617-6`.

[B] L. Ercole, A. Marcolongo, and S. Baroni, "Accurate thermal conductivities from optimally short molecular dynamics simulations", Sci. Rep. **7**, 15835 (2017) `10.1038/s41598-017-15843-2`.

[C] S. Baroni, R. Bertossa, L. Ercole, F. Grasselli, and A. Marcolongo, "Heat transport in insulators from ab initio green-kubo theory", in *Handbook of materials modeling: applications: current and emerging materials*, edited by W. Andreoni, and S. Yip, (Springer International Publishing, Cham, 2018), pp. 1–36, `10.1007/978-3-319-50257-1_12-1`.

[D] R. Bertossa, L. Ercole, and S. Baroni, "Transport coefficients in multicomponent fluids from equilibrium molecular dynamics", arXiv:1808.03341, 2018.

[1] J. Lienhard IV, and J. Lienhard V, *A heat transfer textbook*, 4th (Phlogiston Press, Cambridge, MA, 2017).

[2] J. B. J. Fourier, *The analytical theory of heat* (Cambridge University Press, 1878).

[3] J. C. Mauro, C. S. Philip, D. J. Vaughn, and M. S. Pambianchi, "Glass science in the united states: current status and future directions", International Journal of Applied Glass Science **5**, 2 (2014) `10.1111/ijag.12058`.

[4] J. C. Mauro, "Grand challenges in glass science", Frontiers in Materials **1**, 20 (2014) `10.3389/fmats.2014.00020`.

[5] L. Huang, L. Duffrène, and J. Kieffer, "Structural transitions in silica glass: thermo-mechanical anomalies and polyamorphism", Journal of Non-Crystalline Solids **349**, Glass Science for High Technology. 16th University Conference on Glass Science, 1 (2004) `https://doi.org/10.1016/j.jnoncrysol.2004.08.252`.

[6] P. F. McMillan, "Polyamorphic transformations in liquids and glasses", J. Mater. Chem. **14**, 1506 (2004) `10.1039/B401308P`.

[7] C. R. W. George H. Miller, Edward I. Moses, "The national ignition facility", Optical Engineering **43**, 43 (2004) `10.1117/1.1814767`.

[8] B. Canaud, X. Fortin, F. Garaude, C. Meyer, and F. Philippe, "Progress in direct-drive fusion studies for the laser mégajoule", Laser and Particle Beams **22**, 109 (2004) `10.1017/S0263034604222042`.

[9]   P. E. Miller, J. D. Bude, T. I. Suratwala, N. Shen, T. A. Laurence, W. A. Steele, J. Menapace, M. D. Feit, and L. L. Wong, "Fracture-induced sub-bandgap absorption as a precursor to optical damage on fused silica surfaces", Opt. Lett. **35**, 2702 (2010) `10.1364/OL.35.002702`.

[10] M. Chambonneau, R. Diaz, P. Grua, J.-L. Rullier, G. Duchateau, J.-Y. Natoli, and L. Lamaignère, "Origin of the damage ring pattern in fused silica induced by multiple longitudinal modes laser pulses", Applied Physics Letters **104**, 021121 (2014) `10.1063/1.4861748`.

[11] N. Kuzuu, K. Yoshida, H. Yoshida, T. Kamimura, and N. Kamisugi, "Laser-induced bulk damage in various types of vitreous silica at 1064, 532, 355, and 266 nm: evidence of different damage mechanisms between 266-nm and longer wavelengths", Appl. Opt. **38**, 2510 (1999) `10.1364/AO.38.002510`.

[12] B. C. Stuart, M. D. Feit, A. M. Rubenchik, B. W. Shore, and M. D. Perry, "Laser-induced damage in dielectrics with nanosecond to subpicosecond pulses", Phys. Rev. Lett. **74**, 2248 (1995) `10.1103/PhysRevLett.74.2248`.

[13] J. Wong, J. Ferriera, E. Lindsey, D. Haupt, I. Hutcheon, and J. Kinney, "Morphology and microstructure in fused silica induced by high fluence ultraviolet 3ω (355nm) laser pulses", Journal of Non-Crystalline Solids **352**, 255 (2006) `https://doi.org/10.1016/j.jnoncrysol.2005.11.036`.

[14] C. W. Carr, J. D. Bude, and P. DeMange, "Laser-supported solid-state absorption fronts in silica", Phys. Rev. B **82**, 184304 (2010) `10.1103/PhysRevB.82.184304`.

[15] K. Saito, and A. J. Ikushima, "Absorption edge in silica glass", Phys. Rev. B **62**, 8584 (2000) `10.1103/PhysRevB.62.8584`.

[16] T. F. Soules, G. H. Gilmer, M. J. Matthews, J. S. Stolken, and M. D. Feit, "Silica molecular dynamic force fields-a practical assessment", Journal of Non-Crystalline Solids **357**, 1564 (2011) `https://doi.org/10.1016/j.jnoncrysol.2011.01.009`.

[17] M. I. Ojovan, and W. E. Lee, *An introduction to nuclear waste immobilisation* (Newnes, 2013).

[18] D. J. Evans, and G. P. Morriss, *Statistical mechanics of nonequilibrium liquids* (Academic Press, 1990).

[19] R. Peierls, "Zur kinetischen theorie der wärmeleitung in kristallen", Ann. Phys. (Berlin) **395**, 1055 (1929) `10.1002/andp.19293950803`.

[20] M. S. Green, "Markoff random processes and the statistical mechanics of time-dependent phenomena.", J. Chem. Phys. **20**, 1281 (1952) `10.1063/1.1700722`.

[21] M. Green, "Markoff random processes and the statistical mechanics of time-dependent phenomena. ii. irreversible processes in fluids", J. Chem. Phys. **22**, 398 (1954) `10.1063/1.1740082`.

[22] R. Kubo, "Statistical-mechanical theory of irreversible processes. i. General theory and simple applications to magnetic and conduction problems", J. Phys. Soc. Jpn. **12**, 570 (1957) `10.1143/JPSJ.12.570`.

[23] R. Kubo, M. Yokota, and S. Nakajima, "Statistical-mechanical theory of irreversible processes. ii. response to thermal disturbance", J. Phys. Soc. Jpn. **12**, 1203 (1957) `10.1143/JPSJ.12.1203`.

[24] R. Zwanzig, "Time-correlation functions and transport coefficients in statistical mechanics", Annual Review of Physical Chemistry **16**, 67 (1965) `10.1146/annurev.pc.16.100165.000435`.

[25] P. Hohenberg, and W. Kohn, "Inhomogeneous electron gas", Phys. Rev. **136**, B864 (1964) `10.1103/PhysRev.136.B864`.

[26] W. Kohn, and L. J. Sham, "Self-consistent equations including exchange and correlation effects", Phys. Rev. **140**, A1133 (1965) `10.1103/PhysRev.140.A1133`.

[27] R. M. Martin, *Electronic structure: basic theory and practical methods* (Cambridge University Press, 2008).

[28] D. A. Broido, M. Malorny, G. Birner, N. Mingo, and D. A. Stewart, "Intrinsic lattice thermal conductivity of semiconductors from first principles", Appl. Phys. Lett. **91**, 231922 (2007) `10.1063/1.2822891`.

[29] A. Ward, D. A. Broido, D. A. Stewart, and G. Deinzer, "Ab initio theory of the lattice thermal conductivity in diamond", Phys. Rev. B **80**, 125203 (2009) `10.1103/PhysRevB.80.125203`.

[30] G. Fugallo, A. Cepellotti, L. Paulatto, M. Lazzeri, N. Marzari, and F. Mauri, "Thermal conductivity of graphene and graphite: collective excitations and mean free paths", Nano Letters **14**, 6109 (2014) `10.1021/nl502059f`.

[31] A. Marcolongo, P. Umari, and S. Baroni, "Microscopic theory and ab initio simulation of atomic heat transport", Nature Phys. **12**, 80 (2016) `10.1038/nphys3509`.

[32] L. P. Kadanoff, and P. C. Martin, "Hydrodynamic equations and correlation functions", Ann. Phys. **24**, 419 (1963) `10.1016/0003-4916(63)90078-2`.

[33] D. Forster, *Hydrodynamic fluctuations, broken symmetry, and correlation functions* (Reading, Mass., W. A. Benjamin, Inc., 1975).

[34] L. Onsager, "Reciprocal relations in irreversible processes. i.", Phys. Rev. **37**, 405 (1931) `10.1103/PhysRev.37.405`.

[35] L. Onsager, "Reciprocal relations in irreversible processes. ii.", Phys. Rev. **38**, 2265 (1931) `10.1103/PhysRev.38.2265`.

[36] H. B. G. Casimir, "On onsager's principle of microscopic reversibility", Rev. Mod. Phys. **17**, 343 (1945) `10.1103/RevModPhys.17.343`.

[37] E. Helfand, "Transport coefficients from dissipation in a canonical ensemble", Phys. Rev. **119**, 1 (1960) `10.1103/PhysRev.119.1`.

[38] N. Wiener, "Generalized harmonic analysis", Acta Math. **55**, 117 (1930) `10.1007/BF02546511`.

[39] A. Khintchine, "Korrelationstheorie der stationären stochastischen prozesse", Math. Ann. **109**, 604 (1934) `10.1007/BF01449156`.

[40] A. McGaughey, and M. Kaviany, "Phonon transport in molecular dynamics simulations: formulation and thermal conductivity prediction", in *Advances in heat transfer*, Vol. 39 (Elsevier, 2006), pp. 169–255, `10.1016/S0065-2717(06)39002-8`.

[41] Z. Fan, L. F. C. Pereira, H.-Q. Wang, J.-C. Zheng, D. Donadio, and A. Harju, "Force and heat current formulas for many-body potentials in molecular dynamics simulations with applications to thermal conductivity calculations", Phys. Rev. B **92**, 094301 (2015) `10.1103/PhysRevB.92.094301`.

[42] C. Carbogno, R. Ramprasad, and M. Scheffler, "Ab initio Green-Kubo approach for the thermal conductivity of solids", Phys. Rev. Lett. **118**, 175901 (2017) `10.1103/PhysRevLett.118.175901`.

[43] R. Vogelsang, C. Hoheisel, and G. Ciccotti, "Thermal conductivity of the lennard-jones liquid by molecular dynamics calculations", The Journal of Chemical Physics **86**, 6371 (1987) `10.1063/1.452424`.

[44] D. A. McQuarrie, *Statistical mechanics* (University Science Books, Sausalito, 2000).

[45] A. Kinaci, J. B. Haskins, and T. Çağın, "On calculation of thermal conductivity from einstein relation in equilibrium molecular dynamics", The Journal of Chemical Physics **137**, 014106 (2012) `10.1063/1.4731450`.

[46] A. J. C. Ladd, B. Moran, and W. G. Hoover, "Lattice thermal conductivity: a comparison of molecular dynamics and anharmonic lattice dynamics", Phys. Rev. B **34**, 5058 (1986) `doi.org/10.1103/PhysRevB.34.5058`.

[47] R. J. Hardy, "Atomistic formulas for local properties in systems with many-body interactions", The Journal of Chemical Physics **145**, 204103 (2016) `10.1063/1.4967872`.

[48] J. Tersoff, "Modeling solid-state chemistry: interatomic potentials for multi-component systems", Phys. Rev. B **39**, 5566 (1989) `10.1103/PhysRevB.39.5566`.

[49] F. H. Stillinger, and T. A. Weber, "Computer simulation of local order in condensed phases of silicon", Phys. Rev. B **31**, 5262 (1985) `10.1103/PhysRevB.31.5262`.

[50] R. J. Hardy, "Energy-flux operator for a lattice", Phys. Rev. **132**, 168 (1963) `10.1103/PhysRev.132.168`.

[51] D. Foster, *Hydrodynamic fluctuations, broken symmetry, and correlation functions* (Benjamin, 1975).

[52] P. Sindzingre, and M. J. Gillan, "A computer simulation study of transport coefficients in alkali halides", Journal of Physics: Condensed Matter **2**, 7033 (1990) `10.1088/0953-8984/2/33/014`.

[53] J. H. Irving, and J. G. Kirkwood, "The statistical mechanical theory of transport processes. iv. the equations of hydrodynamics", J. Chem. Phys. **18**, 817 (1950) `10.1063/1.1747782`.

[54] S. Stackhouse, L. Stixrude, and B. B. Karki, "Thermal conductivity of periclase (MgO) from first principles", Phys. Rev. Lett. **104**, 208501 (2010) `10.1103/PhysRevLett.104.208501`.

[55] A. Marcolongo, "Theory and ab initio simulation of atomic heat transport", PhD thesis (Scuola Internazionale Superiore di Studi Avanzati, Trieste, 2014).

[56] S. Plimpton, "Fast parallel algorithms for short-range molecular dynamics", Journal of Computational Physics **117**, 1 (1995) `10.1006/jcph.1995.1039`.

[57] P. K. Schelling, S. R. Phillpot, and P. Keblinski, "Comparison of atomic-level simulation methods for computing thermal conductivity", Phys. Rev. B **65**, 144306 (2002) `10.1103/PhysRevB.65.144306`.

[58] P. C. Howell, "Comparison of molecular dynamics methods and interatomic potentials for calculating the thermal conductivity of silicon", The Journal of Chemical Physics **137**, 224111 (2012) `10.1063/1.4767516`.

[59] B. O. Koopman, "Hamiltonian systems and transformation in hilbert space", Proceedings of the National Academy of Sciences **17**, 315 (1931) `10.1073/pnas.17.5.315`.

[60] J. v. Neumann, "Zur operatorenmethode in der klassischen mechanik", The Annals of Mathematics **33**, 587 (1932) `10.2307/1968537`.

[61] N. Chetty, and R. Martin, "First-principles energy density and its applications to selected polar surfaces", Phys. Rev. B **45**, 6074 (1992) `10.1103/PhysRevB.45.6074`.

[62] R. Car, and M. Parrinello, "Unified approach for molecular dynamics and density-functional theory", Phys. Rev. Lett. **55**, 2471 (1985) `10.1103/PhysRevLett.55.2471`.

[63] D. Marx, and J. Hutter, *Ab initio molecular dynamics: basic theory and advanced methods* (Cambridge University Press, 2009).

[64] G. Fugallo, and L. Colombo, "Calculating lattice thermal conductivity: a synopsis", Physica Scripta **93**, 043002 (2018).

[65] J. Zhou, B. Liao, and G. Chen, "First-principles calculations of thermal, electrical, and thermoelectric transport properties of semiconductors", Semicond. Sci. Technol. **31**, 043001 (2016) `10.1088/0268-1242/31/4/043001`.

[66] S. Baroni, P. Giannozzi, and A. Testa, "Green's-function approach to linear response in solids", Phys. Rev. Lett. **58**, 1861 (1987) `10.1103/PhysRevLett.58.1861`.

[67] X. Gonze, and J. Vigneron, "Density-functional approach to nonlinear-response coefficients of solids", Phys. Rev. B **39**, 13120 (1989).

[68] S. Baroni, S. de Gironcoli, A. Dal Corso, and P. Giannozzi, "Phonons and related crystal properties from density-functional perturbation theory", Rev. Mod. Phys. **73**, 515 (2001) `10.1103/RevModPhys.73.515`.

[69] P. Giannozzi, S. De Gironcoli, P. Pavone, and S. Baroni, "Ab initio calculation of phonon dispersions in semiconductors", Phys. Rev. B **43**, 7231 (1991) `10.1103/PhysRevB.43.7231`.

[70] A. Debernardi, S. Baroni, and E. Molinari, "Anharmonic phonon lifetimes in semiconductors from density-functional perturbation theory", Phys. Rev. Lett. **75**, 1819 (1995) `10.1103/PhysRevLett.75.1819`.

[71] L. Paulatto, F. Mauri, and M. Lazzeri, "Anharmonic properties from a generalized third-order ab initio approach: theory and applications to graphite and graphene", Phys. Rev. B **87**, 214303 (2013) `10.1103/PhysRevB.87.214303`.

[72] L. Lindsay, D. A. Broido, and T. L. Reinecke, "First-principles determination of ultrahigh thermal conductivity of boron arsenide: a competitor for diamond?", Phys. Rev. Lett. **111**, 025901 (2013) `10.1103/PhysRevLett.111.025901`.

[73] L. Lindsay, D. A. Broido, and T. L. Reinecke, "Ab initio thermal transport in compound semiconductors", Phys. Rev. B **87**, 165201 (2013) `10.1103/PhysRevB.87.165201`.

[74] J. Carrete, W. Li, N. Mingo, S. Wang, and S. Curtarolo, "Finding unprecedentedly low-thermal-conductivity half-heusler semiconductors via high-throughput materials modeling", Phys. Rev. X **4**, 011019 (2014) `10.1103/PhysRevX.4.011019`.

[75] A. N. Gandi, and U. Schwingenschlogl, "Ws2 as an excellent high-temperature thermoelectric material", Chemistry of Materials **26**, 6628 (2014) `10.1021/cm503487n`.

[76] G. Fugallo, M. Lazzeri, L. Paulatto, and F. Mauri, "Ab initio variational approach for evaluating lattice thermal conductivity", Phys. Rev. B **88**, 045430 (2013) `10.1103/PhysRevB.88.045430`.

[77] S. Lee, D. Broido, K. Esfarjani, and G. Chen, "Hydrodynamic phonon transport in suspended graphene", Nature Commun. **6**, 6290 (2015) `10.1038/ncomms7290`.

[78] A. Cepellotti, G. Fugallo, L. Paulatto, M. Lazzeri, F. Mauri, and N. Marzari, "Phonon hydrodynamics in two-dimensional materials", Nature Commun. **6**, 6400 (2015) `10.1038/ncomms7400`.

[79] A. Cepellotti, and N. Marzari, "Thermal transport in crystals as a kinetic theory of relaxons", Phys. Rev. X **6**, 1 (2016) `10.1103/PhysRevX.6.041013`.

[80] J. E. Turney, E. S. Landry, A. J. H. McGaughey, and C. H. Amon, "Predicting phonon properties and thermal conductivity from anharmonic lattice dynamics calculations and molecular dynamics simulations", Phys. Rev. B **79**, 064301 (2009) `10.1103/PhysRevB.79.064301`.

[81] M. P. Allen, and D. J. Tildesley, *Computer simulation of liquids* (Clarendon Press, 1989).

[82] D. Frenkel, and B. Smit, *Understanding molecular simulation: from algorithms to applications* (Academic Press, 2001), `10.1016/B978-0-12-267351-1.X5000-7`.

[83] F. Müller-Plathe, "A simple nonequilibrium molecular dynamics method for calculating the thermal conductivity", J. Chem. Phys. **106**, 6082 (1997) `10.1063/1.473271`.

[84] E. Lampin, P. L. Palla, P.-A. Francioso, and F. Cleri, "Thermal conductivity from approach-to-equilibrium molecular dynamics", J. Appl. Phys. **114**, 033525 (2013) `10.1063/1.4815945`.

[85] A. Bouzid, H. Zaoui, P. L. Palla, G. Ori, M. Boero, C. Massobrio, F. Cleri, and E. Lampin, "Thermal conductivity of glassy GeTe4 by first-principles molecular dynamics", Physical Chemistry Chemical Physics **19**, 9729 (2017) `10.1039/C7CP01063J`.

[86] M. Puligheddu, F. Gygi, and G. Galli, "First-principles simulations of heat transport", Phys. Rev. Materials **1**, 060802 (2017) `10.1103/PhysRevMaterials.1.060802`.

[87] Y. He, I. Savić, D. Donadio, and G. Galli, "Lattice thermal conductivity of semiconducting bulk materials: atomistic simulations.", Phys. Chem. Chem. Phys. **14**, 16209 (2012) `10.1039/c2cp42394d`.

[88] D. P. Sellan, E. S. Landry, J. E. Turney, A. J. H. McGaughey, and C. H. Amon, "Size effects in molecular dynamics thermal conductivity predictions", Phys. Rev. B **81**, 214305 (2010) `10.1103/PhysRevB.81.214305`.

[89] Y. He, D. Donadio, and G. Galli, "Heat transport in amorphous silicon: interplay between morphology and disorder", Appl. Phys. Lett. **98**, 144101 (2011) `10.1063/1.3574366`.

[90] H. Zaoui, P. L. Palla, F. Cleri, and E. Lampin, "Length dependence of thermal conductivity by approach-to-equilibrium molecular dynamics", Phys. Rev. B **94**, 054304 (2016) `10.1103/PhysRevB.94.054304`.

[91] Z. Wang, and X. Ruan, "On the domain size effect of thermal conductivities from equilibrium and nonequilibrium molecular dynamics simulations", J. Appl. Phys. **121**, 044301 (2017) `10.1063/1.4974884`.

[92] J. Kang, and L.-W. Wang, "First-principles green-kubo method for thermal conductivity calculations", Phys. Rev. B **96**, 20302 (2017) `10.1103/PhysRevB.96.020302`.

[93] N. J. English, and J. S. Tse, "Equilibrium born-oppenheimer molecular-dynamics exploration of the lattice thermal conductivity of silicon clathrates", Computational Materials Science **126**, 1 (2017) `10.1016/j.commatsci.2016.09.008`.

[94] J. S. Tse, N. J. English, K. Yin, and T. Iitaka, "Thermal conductivity of solids from first-principles molecular dynamics calculations", The Journal of Physical Chemistry C **122**, 10682 (2018) `10.1021/acs.jpcc.8b00880`.

[95] P. Giannozzi, O. Andreussi, T. Brumme, O. Bunau, M. B. Nardelli, M. Calandra, R. Car, C. Cavazzoni, D. Ceresoli, M. Cococcioni, N. Colonna, I. Carnimeo, A. D. Corso, S. de Gironcoli, P. Delugas, R. A. D. Jr, A. Ferretti, A. Floris, G. Fratesi, G. Fugallo, R. Gebauer, U. Gerstmann, F. Giustino, T. Gorni, J. Jia, M. Kawamura, H.-Y. Ko, A. Kokalj, E. Küçükbenli, M. Lazzeri, M. Marsili, N. Marzari, F. Mauri, N. L. Nguyen, H.-V. Nguyen, A. Otero-de-la-Roza, L. Paulatto, S. Poncé, D. Rocca, R. Sabatini, B. Santra, M. Schlipf, A. P. Seitsonen, A. Smogunov, I. Timrov, T. Thonhauser, P. Umari, N. Vast, X. Wu, and S. Baroni, "Advanced capabilities for materials modelling with q uantum espresso", Journal of Physics: Condensed Matter **29**, 465901 (2017) `10.1088/1361-648X/aa8f79`.

[96] D. J. Thouless, "Quantization of particle transport", Phys. Rev. B **27**, 6083 (1983) `10.1103/PhysRevB.27.6083`.

[97] P. Giannozzi, S. Baroni, N. Bonini, M. Calandra, R. Car, C. Cavazzoni, D. Ceresoli, G. L. Chiarotti, M. Cococcioni, I. Dabo, A. D. Corso, S. Gironcoli, S. Fabris, G. Fratesi, R. Gebauer, U. Gerstmann, C. Gougoussis, A. Kokalj, M. Lazzeri, L. Martin-Samos, N. Marzari, F. Mauri, R. Mazzarello, S. Paolini, A. Pasquarello, L. Paulatto, C. Sbraccia, S. Scandolo, G. Sclauzero, A. P. Seitsonen, A. Smogunov, P. Umari, and R. M. Wentzcovitch, "QUANTUM ESPRESSO: a modular and open-source software project for quantum simulations of materials", J. Phys. Condens. Matter **21**, 395502 (19pp) (2009) `10.1088/0953-8984/21/39/395502`.

[98] N. Marzari, A. A. Mostofi, J. R. Yates, I. Souza, and D. Vanderbilt, "Maximally localized wannier functions: theory and applications", Rev. Mod. Phys. **84**, 1419 (2012) `10.1103/RevModPhys.84.1419`.

[99] A. Damle, L. Lin, and L. Ying, "Compressed representation of kohn-sham orbitals via selected columns of the density matrix", J. Chem. Theory Comput. **11**, 1463 (2015) `10.1021/ct500985f`.

[100] R. H. French, V. A. Parsegian, R. Podgornik, R. F. Rajter, A. Jagota, J. Luo, D. Asthagiri, M. K. Chaudhury, Y.-m. Chiang, S. Granick, S. Kalinin, M. Kardar, R. Kjellander, D. C. Langreth, J. Lewis, S. Lustig, D. Wesolowski, J. S. Wettlaufer, W.-Y. Ching, M. Finnis, F. Houlihan, O. A. von Lilienfeld, C. J. van Oss, and T. Zemb, "Long range interactions in nanoscale science", Rev. Mod. Phys. **82**, 1887 (2010) `10.1103/RevModPhys.82.1887`.

[101] K. Berland, V. Cooper, K. Lee, E. Schröder, T. Thonhauser, P. Hyldgaard, and B. Lundqvist, "Van der waals forces in density functional theory: a review of the vdw-df method", Rep. Progr. Phys. **78**, 66501 (2015) `10.1088/0034-4885/78/6/066501`.

[102] K. Gordiz, D. J. Singh, and A. Henry, "Ensemble averaging vs. time averaging in molecular dynamics simulations of thermal conductivity", Journal of Applied Physics **117**, 045104 (2015) `10.1063/1.4906957`.

[103] K. V. Tretiakov, and S. Scandolo, "Thermal conductivity of solid argon from molecular dynamics simulations", J. Chem. Phys. **120**, 3765 (2004) `10.1063/1.1642611`.

[104] J. Alejandre, G. A. Chapela, F. Bresme, and J. P. Hansen, "The short range anion-h interaction is the driving force for crystal formation of ions in water", J. Chem. Phys. **130** (2009) `10.1063/1.3124184`.

[105] P. Shukla, T. Watanabe, J. C. Nino, J. S. Tulenko, and S. R. Phillpot, "Thermal transport properties of mgo and nd2zr2o7 pyrochlore by molecular dynamics simulation", J. Nucl. Mat. **380**, 1 (2008) `10.1016/j.jnucmat.2008.06.043`.

[106] B. W. H. van Beest, G. J. Kramer, and R. A. van Santen, "Force fields for silicas and aluminophosphates based on ab initio calculations", Phys. Rev. Lett. **64**, 1955 (1990) `10.1103/PhysRevLett.64.1955`.

[107] B. Mantisi, A. Tanguy, G. Kermouche, and E. Barthel, "Atomistic response of a model silica glass under shear and pressure", The European Physical Journal B **85**, 304 (2012) `10.1140/epjb/e2012-30317-6`.

[108] A. V. Oppenheim, R. W. Schafer, and J. R. Buck, *Discrete-time signal processing (2nd edition) (prentice-hall signal processing series)* (Prentice Hall, 1999).

[109] A. McGaughey, and M. Kaviany, "Thermal conductivity decomposition and analysis using molecular dynamics simulations. part i. lennard-jones argon", International Journal of Heat and Mass Transfer **47**, 1783 (2004) `10.1016/j.ijheatmasstransfer.2003.11.002`.

[110] J. Li, L. Porter, and S. Yip, "Atomistic modeling of finite-temperature properties of crystalline β-sic: ii. thermal conductivity and effects of point defects", Journal of Nuclear Materials **255**, 139 (1998) `10.1016/S0022-3115(98)00034-8`.

[111] A. McGaughey, and M. Kaviany, "Thermal conductivity decomposition and analysis using molecular dynamics simulations: part ii. complex silica structures", International Journal of Heat and Mass Transfer **47**, 1799 (2004) `10.1016/j.ijheatmasstransfer.2003.11.009`.

[112] E. W. Weisstein, *Moving average*, From MathWorld – a Wolfram Web Resource, `http://mathworld.wolfram.com/MovingAverage.html`.

[113] J. Chen, G. Zhang, and B. Li, "How to improve the accuracy of equilibrium molecular dynamics for computation of thermal conductivity?", Phys. Lett. A **374**, 2392 (2010) `10.1016/j.physleta.2010.03.067`.

[114] R. E. Jones, and K. K. Mandadapu, "Adaptive green-kubo estimates of transport coefficients from molecular dynamics based on robust error analysis.", J. Chem. Phys. **136**, 154102 (2012) `10.1063/1.3700344`.

[115] Z. Wang, S. Safarkhani, G. Lin, and X. Ruan, "Uncertainty quantification of thermal conductivities from equilibrium molecular dynamics simulations", International Journal of Heat and Mass Transfer **112**, 267 (2017) `10.1016/j.ijheatmasstransfer.2017.04.077`.

[116] L. d. S. Oliveira, and P. A. Greaney, "Method to manage integration error in the green-kubo method", Phys. Rev. E **95**, 023308 (2017) `10.1103/PhysRevE.95.023308`.

[117] J. Che, T. Çağın, W. Deng, and W. A. Goddard, "Thermal conductivity of diamond and related materials from molecular dynamics simulations", The Journal of Chemical Physics **113**, 6888 (2000) `10.1063/1.1310223`.

[118] Y. Zhang, A. Otani, and E. J. Maginn, "Reliable viscosity calculation from equilibrium molecular dynamics simulations: a time decomposition method", J. Chem. Theory Comput. **11**, 3537 (2015) `10.1021/acs.jctc.5b00351`.

[119] D. G. Cahill, and R. Pohl, "Heat flow and lattice vibrations in glasses", Solid State Communications **70**, 927 (1989) `https://doi.org/10.1016/0038-1098(89)90630-3`.

[120] D. G. Cahill, S. K. Watson, and R. O. Pohl, "Lower limit to the thermal conductivity of disordered crystals", Phys. Rev. B **46**, 6131 (1992) `10.1103/PhysRevB.46.6131`.

[121] J. Che, T. Çagin, and W. A. G. III, "Thermal conductivity of carbon nanotubes", Nanotechnology **11**, 65 (2000).

[122] N. Hirosaki, S. Ogata, C. Kocer, H. Kitagawa, and Y. Nakamura, "Molecular dynamics calculation of the ideal thermal conductivity of single-crystal α- and β-si$_3$n$_4$", Phys. Rev. B **65**, 134110 (2002) `10.1103/PhysRevB.65.134110`.

[123] Y. H. Lee, R. Biswas, C. M. Soukoulis, C. Z. Wang, C. T. Chan, and K. M. Ho, "Molecular-dynamics simulation of thermal conductivity in amorphous silicon", Phys. Rev. B **43**, 6573 (1991) `10.1103/PhysRevB.43.6573`.

[124] S. G. Volz, and G. Chen, "Molecular-dynamics simulation of thermal conductivity of silicon crystals", Phys. Rev. B **61**, 2651 (2000) `10.1103/PhysRevB.61.2651`.

[125] K. Esfarjani, G. Chen, and H. T. Stokes, "Heat transport in silicon from first-principles calculations", Phys. Rev. B **84**, 085204 (2011) `10.1103/PhysRevB.84.085204`.

[126] P. S. Stoica, and R. Moses, *Spectral analysis of signals* (Prentice Hall, Upper Saddle River, 2005).

[127] E. W. Weisstein, *Polygamma functions*, From MathWorld –A Wolfram Web Resource, `http://mathworld.wolfram.com/PolygammaFunction.html`.

[128] D. G. Childers, D. P. Skinner, and R. C. Kemerait, "The cepstrum: a guide to processing", Proceedings of the IEEE **65**, 1428 (1977) `10.1109/PROC.1977.10747`.

[129] T. W. Anderson, *The statistical analysis of time series* (Wiley-Interscience, 1994).

[130] M. Peligrad, and W. B. Wu, "Central limit theorem for fourier transforms of stationary processes", Ann. Prob. **38**, 2009 (2010) `10.1214/10-AOP530`.

[131] G. Claeskens, and N. L. Hjort, *Model selection and model averaging* (Cambridge University Press, 2008).

[132] H. Akaike, "A new look at the statistical model identification", IEEE Trans. Autom. Control **19**, 716 (1974) `10.1109/TAC.1974.1100705`.

[133] L. Ercole, and R. Bertossa, ThermoCepstrum*: a code to compute thermal conductivity through the cepstral analysis of heat flux time series*, (2017) `https://github.com/lorisercole/thermocepstrum`.

[134] F. Römer, A. Lervik, and F. Bresme, "Nonequilibrium molecular dynamics simulations of the thermal conductivity of water: a systematic investigation of the spc/e and tip4p/2005 models", J. Chem. Phys. **137**, 074503 (2012) `10.1063/1.4739855`.

[135] J. M. Larkin, and A. J. H. McGaughey, "Thermal conductivity accumulation in amorphous silica and amorphous silicon", Phys. Rev. B **89**, 144303 (2014) `10.1103/PhysRevB.89.144303`.

[136] S. S. Shapiro, and M. B. Wilk, "An analysis of variance test for normality (complete samples)", Biometrika **52**, 591 (1965) `10.2307/2333709`.

[137] K. P. Burnham, and R. P. Anderson, "Multimodel inference: understanding aic and bic in model selection", Soc. Meth. Res. **33**, 261 (2004) `10.1177/0049124104268644`.

[138] N. R. Goodman, "Statistical analysis based on a certain multivariate complex gaussian distribution (an introduction)", Ann. Math. Stat. **34**, 152 (1963).

[139] N. Goodman, "The distribution of the determinant of a complex wishart distributed matrix", Ann. Math. Stat. **34**, 178 (1963) `10.1214/aoms/1177704251`.

[140] A. M. Kshirsagar, "Bartlett decomposition and wishart distribution", Ann. Math. Statist. **30**, 239 (1959) `10.1214/aoms/1177706379`.

[141] D. K. Nagar, and A. K. Gupta, "Expectations of functions of complex wishart matrix", Acta Applicandae Mathematicae **113**, 265 (2011) `10.1007/s10440-010-9599-x`.

[142] P. H.-L. Sit, and N. Marzari, "Static and dynamical properties of heavy water at ambient conditions from first-principles molecular dynamics", The Journal of Chemical Physics **122**, 204510 (2005) `10.1063/1.1908913`.

[143] J. P. Perdew, K. Burke, and M. Ernzerhof, "Generalized gradient approximation made simple", Phys. Rev. Lett. **77**, 3865 (1996) `10.1103/PhysRevLett.77.3865`.

[144] N. Matsunaga, and A. Nagashima, "Transport properties of liquid and gaseous D2O over a wide range of temperature and pressure", Journal of Physical and Chemical Reference Data **12**, 933 (1983) `10.1063/1.555694`.

[145] M. L. V. Ramires, C. A. N. de Castro, Y. Nagasaka, A. Nagashima, M. J. Assael, and W. A. Wakeham, "Standard reference data for the thermal conductivity of water", Journal of Physical and Chemical Reference Data **24**, 1377 (1995) `10.1063/1.555963`.

[146] I. Saika-Voivod, F. Sciortino, T. Grande, and P. H. Poole, "Phase diagram of silica from computer simulation", Phys. Rev. E **70**, 061507 (2004) `10.1103/PhysRevE.70.061507`.

[147] A. Carré, J. Horbach, S. Ispas, and W. Kob, "New fitting scheme to obtain effective potential from car-parrinello molecular-dynamics simulations: application to silica", EPL (Europhysics Letters) **82**, 17001 (2008).

[148] P. Tangney, and S. Scandolo, "An ab initio parametrized interatomic force field for silica", The Journal of Chemical Physics **117**, 8898 (2002) `10.1063/1.1513312`.

[149] X. Yuan, and A. Cormack, "Local structures of md-modeled vitreous silica and sodium silicate glasses", Journal of Non-Crystalline Solids **283**, 69 (2001) `https://doi.org/10.1016/S0022-3093(01)00363-5`.

[150] Y. Tian, J. Du, W. Han, X. Zu, X. Yuan, and W. Zheng, "Thermal conductivity of vitreous silica from molecular dynamics simulations: the effects of force field, heat flux and system size", The Journal of Chemical Physics **146**, 054504 (2017) `10.1063/1.4975162`.

[151] K. Vollmayr, W. Kob, and K. Binder, "Cooling-rate effects in amorphous silica: a computer-simulation study", Phys. Rev. B **54**, 15808 (1996) `10.1103/PhysRevB.54.15808`.

[152] B. Bhattarai, and D. Drabold, "Vibrations in amorphous silica", Journal of Non-Crystalline Solids **439**, 6 (2016) `https://doi.org/10.1016/j.jnoncrysol.2016.02.002`.

[153] J. Sarnthein, A. Pasquarello, and R. Car, "Origin of the high-frequency doublet in the vibrational spectrum of vitreous sio2", Science **275**, 1925 (1997) `10.1126/science.275.5308.1925`.

[154] F. L. Galeener, A. J. Leadbetter, and M. W. Stringfellow, "Comparison of the neutron, raman, and infrared vibrational spectra of vitreous sio_2, geo_2, and bef_2", Phys. Rev. B **27**, 1052 (1983) `10.1103/PhysRevB.27.1052`.

[155] M. Benoit, and W. Kob, "The vibrational dynamics of vitreous silica: classical force fields vs. first principles", EPL (Europhysics Letters) **60**, 269 (2002).

[156] T. Coquil, J. Fang, and L. Pilon, "Molecular dynamics study of the thermal conductivity of amorphous nanoporous silica", International Journal of Heat and Mass Transfer **54**, 4540 (2011) `https://doi.org/10.1016/j.ijheatmasstransfer.2011.06.024`.

[157] X. Yu, and D. M. Leitner, "Thermal conductivity computed for vitreous silica and methyl-doped silica above the plateau", Phys. Rev. B **74**, 184305 (2006) `10.1103/PhysRevB.74.184305`.

[158] J. Sarnthein, A. Pasquarello, and R. Car, "Structural and electronic properties of liquid and amorphous sio_2: an ab initio molecular dynamics study", Phys. Rev. Lett. **74**, 4682 (1995) `10.1103/PhysRevLett.74.4682`.

[159] J. Sarnthein, A. Pasquarello, and R. Car, "Model of vitreous sio_2 generated by an ab initio molecular-dynamics quench from the melt", Phys. Rev. B **52**, 12690 (1995) `10.1103/PhysRevB.52.12690`.

[160] M. Benoit, S. Ispas, P. Jund, and R. Jullien, "Model of silica glass from combined classical and ab initio molecular-dynamics simulations", Eur. Phys. J. B **13**, 631 (2000) `10.1007/s100510050079`.

[161] R. M. Van Ginhoven, H. Jónsson, and L. R. Corrales, "Silica glass structure generation for ab initio calculations using small samples of amorphous silica", Phys. Rev. B **71**, 024208 (2005) `10.1103/PhysRevB.71.024208`.

[162] J. M. D. Lane, "Cooling rate and stress relaxation in silica melts and glasses via microsecond molecular dynamics", Phys. Rev. E **92**, 012320 (2015) `10.1103/PhysRevE.92.012320`.

[163] D. Wolf, "Reconstruction of nacl surfaces from a dipolar solution to the madelung problem", Phys. Rev. Lett. **68**, 3315 (1992) `10.1103/PhysRevLett.68.3315`.

[164] D. Wolf, P. Keblinski, S. R. Phillpot, and J. Eggebrecht, "Exact method for the simulation of coulombic systems by spherically truncated, pairwise r-1 summation", The Journal of Chemical Physics **110**, 8254 (1999) `10.1063/1.478738`.

[165] C. J. Fennell, and J. D. Gezelter, "Is the ewald summation still necessary? pairwise alternatives to the accepted standard for long-range electrostatics", The Journal of Chemical Physics **124**, 234104 (2006) `10.1063/1.2206581`.

[166] G. Bussi, D. Donadio, and M. Parrinello, "Canonical sampling through velocity rescaling", J. Chem. Phys. **126**, 014101 (2007) `10.1063/1.2408420`.

[167] S. Andersson, and L. Dzhavadov, "Thermal conductivity and heat capacity of amorphous sio 2 : pressure and volume dependence", Journal of Physics: Condensed Matter **4**, 6209 (1992).

[168] M. Schlipf, and F. Gygi, "Optimization algorithm for the generation of oncv pseudopotentials", Computer Physics Communications **196**, 36 (2015) `https://doi.org/10.1016/j.cpc.2015.05.011`.

[169]   D. R. Hamann, "Optimized norm-conserving vanderbilt pseudopotentials", Phys. Rev. B **88**, 085117 (2013) `10.1103/PhysRevB.88.085117`.

[170]   S. Nosé, "A unified formulation of the constant temperature molecular dynamics methods", The Journal of Chemical Physics **81**, 511 (1984) `10.1063/1.447334`.

[171]   W. G. Hoover, "Canonical dynamics: equilibrium phase-space distributions", Phys. Rev. A **31**, 1695 (1985) `10.1103/PhysRevA.31.1695`.

[172]   Y. Touloukian, R. Powell, C. Ho, and P. Klemens, *Thermophysical properties of matter - the tprc data series. volume 2. thermal conductivity - nonmetallic solids. (reannouncement). data book* (IFI/Plenum, New York, Jan. 1970).

[173]   D. G. Cahill, "Thermal conductivity measurement from 30 to 750k: the 3ω method", Review of Scientific Instruments **61**, 802 (1990) `10.1063/1.1141498`.

[174]   A. Sugawara, "Precise determination of thermal conductivity of high purity fused quartz from $0°$ to $650°c$", Physica **41**, 515 (1969) `https://doi.org/10.1016/0031-8914(69)90053-6`.

[175]   W. D. Kingery, "Thermal conductivity: xii, temperature dependence of conductivity for single-phase ceramics", Journal of the American Ceramic Society **38**, 251 (1955) `10.1111/j.1151-2916.1955.tb14940.x`.

[176]   K. L. Wray, and T. J. Connolly, "Thermal conductivity of clear fused silica at high temperatures", Journal of Applied Physics **30**, 1702 (1959) `10.1063/1.1735040`.

[177]   S. T. Yang, M. J. Matthews, S. Elhadj, V. G. Draggoo, and S. E. Bisson, "Thermal transport in co2 laser irradiated fused silica: in situ measurements and analysis", Journal of Applied Physics **106**, 103106 (2009) `10.1063/1.3259419`.

[178]   *Quartz glass for optics data and properties*, Heraeus (2010).

[179]   L. C. Carwile, and H. J. Hoge, *Thermal conductivity of vitreous silica: selected values*, tech. rep. 67-7-PR (U.S. Army Natick Laboratories, July 1966).

[180]   R. Gardon, "A review of radiant heat transfer in glass", Journal of the American Ceramic Society **44**, 305 (1961) `10.1111/j.1151-2916.1961.tb15914.x`.

[181]   P. Bouchut, D. Decruppe, and L. Delrive, "Fused silica thermal conductivity dispersion at high temperature", Journal of Applied Physics **96**, 3221 (2004) `10.1063/1.1776629`.

[182]   P. B. Allen, and J. L. Feldman, "Thermal conductivity of glasses: theory and application to amorphous si", Phys. Rev. Lett. **62**, 645 (1989) `10.1103/PhysRevLett.62.645`.